Protected states and metastable dynamics in superconducting circuits

Paul Brookes

A dissertation submitted in partial fulfillment

of the requirements for the degree of

Doctor of Philosophy

of

University College London.

Department of Physics

University College London

June 17, 2021

I, Paul Brookes, confirm that the work presented in this thesis is my own. Where information has been derived from other sources, I confirm that this has been indicated in the work.

Abstract

The twin fields of superconducting circuits and circuit quantum electrodynamics now form the basis for a major part of the effort towards building a quantum computer. Yet many fundamental problems remain. These may range from very practical considerations, such as how to construct a qubit with a sufficiently long coherence time, to questions of how best to understand and model the complex nonlinear dynamics arising in superconducting circuits. In this thesis we take a broad look at these fields and explore many questions within them. We begin by studying critical slowing down in a dissipative phase transition of a coupled qubit-cavity system, before examining the underlying dynamics of switching between metastable states which causes this slowdown. We then examine an unexplained phenomenon of resonance narrowing in another qubit-cavity system and suggest it may also be related to metastable states. Finally, we examine a circuit which harnesses long range interactions, and present it as a promising candidate for building a qubit with a long coherence time.

Acknowledgements

First I would like to thank my doctoral advisors Marzena Szymańska and Eran Ginossar who have provided so much support and guidance throughout this work. I would also like to thank Eytan Grosfeld and Michael Stern for generously hosting me for many months of research visits and making invaluable contributions to chapter 5.

The experimental work detailed in chapter 2 was carried out by Giovanna Tancredi in the lab of Peter Leek at the University of Oxford while the experimental work in chapter 4 was carried out by Eyal Buks in the lab of Adrian Lupascu at the University of Waterloo. I am grateful to them all for the opportunity to work with some real world data and get some understand of the side of physics about which everything else revolves. Next I would like to thank Chang-Woo Lee whose work applying Keldysh field theory to nonlinear oscillators formed a key part of chapter 3.

Finally I would like to thank my friends in the community of UCL and my family.

Impact Statement

The work described in this thesis is directly relevant to the development of quantum computation, which we hope will become an extremely useful toolset in the near future for a wide variety of tasks including the simulation of quantum systems, drug discovery and machine learning. This field is rapidly in the process of expanding out of academia so it is hoped that successful application of the knowledge derived in this thesis will also lead to commercial opportunities.

In particular, the first half of the thesis focuses on nonlinear dynamics in coupled qubit-cavity systems. Understanding such dynamics has previously been crucial in the development of various readout and control techniques which are crucial to the operation of a future quantum computer. We hope our contributions will find application in a similar way in the future.

The second half of this thesis focuses on a design which we consider to be a good candidate for a long-lived qubit. One of the key obstacles to the development of a quantum computer is the preservation of quantum coherence and there is enormous demand for solutions to this problem.

Contents

List of Figures

Chapter 1

Introduction

1.1 Superconducting qubits

Superconducting qubits are currently one of the leading platforms for the design and construction of quantum computers. These qubits can take many different forms, but typically they share some common features: they consist of lithographically fabricated superconducting circuits patterned onto a substrate and contain at least one nonlinear circuit element. This last point is crucial. In the absence of nonlinearity the degrees of freedom of the circuit would form a set of noninteracting harmonic oscillators and it would be impossible to selectively address the transition between a specific pair of eigenmodes of the circuit. Hence we would be unable to perform operations on any information encoded in its state. Josephson junctions are chosen for this purpose and offer the distinct advantage of being dissipation free, which helps us to preserve the quantum state of the circuit for sufficient time that computations can be carried out.

The resulting circuits are multi level quantum devices whose parameters can be engineered during the design process and this gives the experimentalist a high degree of control over properties such as their transition frequencies and couplings to other components and to electromagnetic field modes. For this reason they are often termed artificial atoms and have come to replace natural atoms in many experiments in cavity quantum electrodynamics, thus fueling the rise of circuit quantum electrodynamics [1].

The ability to tailor superconducting circuits has been an enormous advantage during their development and they now form the core of many of the leading efforts to build a quantum processor including [2]. Currently the most popular superconducting qubit for these efforts is the transmon [3], whose properties we will detail below. However even the most advanced quantum processors are still limited by the short coherence times of the current generation of qubits. One proposal to tackle this problem is the implementation of quantum error correction algorithms [4, 5, 6] which combine many individual short-lived physical qubits into a single collective logical qubit whose lifetime can be extended by detecting and correcting errors in the underlying qubits.

Unfortunately this approach faces many obstacles. In particular it is very challenging to carry out the necessary error detection and correction operators on a large ensemble of qubits, and even if this problem is solved the number of physical qubits required per logical qubit will be prohibitively large given the state of coherence times. If many thousands of physical qubits are required then it will difficult to even fit them onto a chip. For this reason some research focus has shifted towards the study of what useful computations on noisy intermediate-scale quantum (NISQ) devices [7].

However, whether one is interested in using quantum error correction to build a fault-tolerant quantum computer or performing calculations on a imperfect computer it will continue to be of fundamental importance that improvements are made in the underlying hardware. Therefore it is interesting to consider what improvements can be made to develop a new generation of superconducting qubits. Many efforts are currently being explored in this direction throughout the world but before we can discuss such them we intend to first introduce the reader to the various currently available classes of qubit [8, 9]. We will not be able to provide exhaustive coverage, but we hope to provide some foundation in their operating principals, beginning with the Hamiltonian and Lagrangian mechanics of circuits and an introduction to the Josephson junction.

1.2 Hamiltonian and Lagrangian circuits

In Lagrangian mechanics [10] we first construct the kinetic T and potential V energies in terms of some generalised coordinates q_j before constructing the Lagrangian according to $L = T - V$. We can then obtain the equations of motion via the Euler-Lagrange equations:

$$\frac{d}{dt}\left(\frac{\partial L}{\partial \dot{x}_j}\right) = \frac{\partial L}{\partial x_j}. \tag{1.1}$$

Alternatively we can move to a Hamiltonian formulation by defining canonical conjugate momenta p_j and performing a Legendre transformation:

$$p_j = \frac{\partial L}{\partial \dot{x}_j}, \qquad H = \sum_j p_j \dot{x}_j - L \tag{1.2}$$

which produces equations of motion given by:

$$\dot{x}_j = \frac{\partial H}{\partial p_j}, \qquad \dot{p}_j = -\frac{\partial H}{\partial x_j}. \tag{1.3}$$

Time derivatives can also be calculated using the Poisson bracket $\{\cdot,\cdot\}$. This operation is defined by:

$$\{f,g\} = \sum_j \left(\frac{\partial f}{\partial x_j}\frac{\partial g}{\partial p_j} - \frac{\partial f}{\partial p_j}\frac{\partial g}{\partial x_j}\right) \tag{1.4}$$

for two functions $f(x,p)$ and $g(x,p)$ which are defined on the phase space coordinates. Using this tool the time derivative of function f can be calculated by taking its Poisson bracket with the Hamiltonian:

$$\frac{df}{dt} = \{f,H\}. \tag{1.5}$$

For the cases $f = x_j$ and $f = p_j$ this reduces directly to the equations of motion displayed in eq. 1.3. Throughout our work we will be interested in the quantum mechanics describing the low lying excitations of superconducting circuits. To move beyond the classical formalism described above we will use the technique of canon-

ical quantization [11, 12]. This requires us to replace the system coordinates with quantum mechanical operators and replace Poisson brackets with commutators:

$$x_j \to \hat{x}_j, \quad p_j \to \hat{p}_j, \quad \{f,g\} \to \frac{1}{i\hbar}[\hat{f},\hat{g}]. \tag{1.6}$$

for which we define $[\hat{A},\hat{B}] = \hat{A}\hat{B} - \hat{B}\hat{A}$. Now the time derivative of a function of the system coordinates will be given by a Heisenberg equation of motion:

$$\frac{d\hat{f}}{dt} = \frac{1}{i\hbar}[\hat{f},\hat{H}]. \tag{1.7}$$

Meanwhile the Poisson brackets of the system coordinates:

$$\{x_i, x_j\} = 0, \tag{1.8}$$

$$\{p_i, p_j\} = 0, \tag{1.9}$$

$$\{x_i, p_j\} = \delta_{i,j} \tag{1.10}$$

are replaced by the canonical commutation relations:

$$[\hat{x}_i, \hat{x}_j] = 0, \tag{1.11}$$

$$[\hat{p}_i, \hat{p}_j] = 0, \tag{1.12}$$

$$[\hat{x}_i, \hat{p}_j] = i\hbar\delta_{i,j}. \tag{1.13}$$

In order to transfer these formulation to circuits we must find some quantities which can fulfill the role of generalised coordinates. We outline this process as follows [13, 14, 8]. First consider a circuit element which connects nodes labelled j and k. The voltage across this element can be labelled by $V_{j,k} = V_j - V_k$ while the current flowing through it from node j to k is labelled $I_{j,k}$. We are now in a position to define fluxes $\Phi_{j,k}$ and charges $Q_{j,k}$ for the elements of our circuit according to:

$$\Phi_{j,k}(t) = \int_{-\infty}^{t} V_{j,k}(t')dt' \quad \text{and} \quad Q_{j,k}(t) = \int_{-\infty}^{t} I_{j,k}(t')dt'. \tag{1.14}$$

We can select our generalised coordinates from either of these sets but we must be careful to take into account the constraints imposed by the conservation of charge and the Maxwell-Faraday equation. We shall see that these variables do not form an independent set of coordinates. Specifically, the conservation of charge tells us that the currents entering a node should sum to zero and this can be used to relate the charges of all elements connected to a given node k according to:

$$\sum_j I_{j,k} = 0 \tag{1.15}$$

$$\implies \sum_j Q_{j,k} = \tilde{Q}_j \tag{1.16}$$

for some constant $\tilde{Q}_j$. Meanwhile the Maxwell-Faraday equation tells us that the potential difference acquired around a loop in the circuit should be proportional to the rate of change of the magnetic flux threading through that loop. These allows us to relate the fluxes in a loop according to:

$$\sum_{j,k\in\text{loop } l} V_{j,k} = -\frac{\partial\tilde{\Phi}_l}{\partial t} \tag{1.17}$$

$$\implies \sum_{j,k\in\text{loop } l} \Phi_{j,k} = -\tilde{\Phi}_l(t) \tag{1.18}$$

where $\tilde{\Phi}_l(t)$ is the loop flux. In order to account for these constraints we find a an acyclic connected graph which reaches all nodes of our circuit [14, 15]. Such a graph is known as a tree and its edges are called branches. By including only those charges or fluxes which refer to branches of our tree we ensure that our coordinates are independent. The charges and fluxes of any circuit elements outside this tree can be obtained via the constraints outlined above.

Next we consider how to write down the Lagrangian of the circuit. This requires us to choose which set of variables to use as generalised coordinates and then write down kinetic and potential energies of the circuit elements. Kinetic energies will depend on the rates of change of our coordinates, while potential energies will depend on the coordinates themselves. We shall see below that the roles of ki-

netic and potential energies can be played by either capacitive or inductive elements of the circuit depending on whether we choose branch fluxes or branch charges as our coordinates. To outline this, we first classify the elements of our circuit as either inductive or capacitive. Inductive and capacitive elements can be described by a constitutive relations of the form [14]:

$$I = g(\Phi) \quad \text{and} \quad V = f(Q) \tag{1.19}$$

respectively. For example, in the case of linear circuit elements these relations taken the familiar forms:

$$I = \Phi/L \quad \text{and} \quad V = Q/C \tag{1.20}$$

with capacitance C and inductance L. Given that the power flowing into a circuit element is $P = IV$, we can calculate the energy stored in a circuit element according to $E = \int_{-\infty}^{t} I(t')V(t')dt'$. The resulting energies for our two element types are:

$$E_I(\Phi) = \int_0^{\Phi} g(\Phi')d\Phi' \quad \text{and} \quad E_C(Q) = \int_0^{Q} f(Q')dQ'. \tag{1.21}$$

For linear circuit elements these energies are given by

$$E_I(\Phi) = \frac{\Phi^2}{2L} \quad \text{and} \quad E_C(Q) = \frac{Q^2}{2C}. \tag{1.22}$$

If we choose the branch fluxes as our coordinates then we can use $V_{k,l} = \dot{\Phi}_{k,l}$ along with the second relation in eq. 1.20 in order to write:

$$E_C(Q(\dot{\Phi})) = \frac{C\dot{\Phi}^2}{2} \tag{1.23}$$

We can write the kinetic and potential energies of our circuit as

$$T = \sum_{k,l \in \text{ capacitive elements}} E_C(Q_{k,l}(\dot{\Phi}_{k,l})) \quad \text{and} \quad V = \sum_{k,l \in \text{ inductive elements}} E_I(\Phi_{k,l}). \tag{1.24}$$

However if we had chosen to use branch charges as our coordinates then we would continue to represent the capacitive energy as in eq. 1.22 and we would use $I_{k,l} = \dot{Q}_{k,l}$ and the first relation in eq. 1.20 to write the inductive energy as:

$$E_I(\Phi(\dot{Q})) = \frac{L\dot{Q}^2}{2}. \tag{1.25}$$

We could therefore exchange the roles of capacitive and inductive elements in the representation of kinetic and potential energies. However we will now proceed using branch fluxes as our coordinates.

At this point we could calculate the Lagrangian $L = T - V$ and produce equations of motion according to the Euler-Lagrange equations in eq. 1.1. Or if we wish to move to the Hamiltonian formalism we could find the canonical momenta, which now take the form of charges, and perform a Legendre transformation:

$$q_{k,l} = \frac{\partial L}{\partial \dot{\Phi}_{k,l}}, \qquad H = \sum_{k,l \in \text{ branches}} \dot{\Phi}_{k,l} q_{k,l} - L. \tag{1.26}$$

This results in a Hamiltonian H which produces equations of motion in the form:

$$\dot{\Phi}_{k,l} = \frac{\partial H}{\partial q_{k,l}}, \qquad \dot{q}_{k,l} = -\frac{\partial H}{\partial \Phi_{k,l}}. \tag{1.27}$$

For a simple circuit consisting of an inductor L and a capacitor C connected in parallel there is only one branch in the spanning tree. We easily obtain Lagrangian:

$$L = \frac{C\dot{\Phi}^2}{2} - \frac{\Phi^2}{2L} \tag{1.28}$$

from which we obtain the conjugate charge:

$$q = \frac{\partial L}{\partial \dot{\Phi}} = C\dot{\Phi} \tag{1.29}$$

and the Hamiltonian:

$$H = \frac{q^2}{2C} + \frac{\Phi^2}{2L} \tag{1.30}$$

which describes a simple harmonic oscillator with a natural frequency of $\omega_0 = \frac{1}{\sqrt{LC}}$. If we apply the canonical quantization procedure described above then we replace our coordinates by quantum operators which obey the commutation relation:

$$[\Phi, q] = i\hbar. \tag{1.31}$$

For our convenience we will no longer denote quantum operators using hats $\hat{O} \to O$. For this quantized simple harmonic oscillator we can define ladder operators a and $a^\dagger$ according to:

$$a = \sqrt{\frac{C\omega_0}{2\hbar}}\left(\Phi + \frac{iq}{C\omega_0}\right) \tag{1.32}$$

which obey:

$$[a, a^\dagger] = 1, \tag{1.33}$$

$$[a, a^\dagger a] = a, \tag{1.34}$$

$$[a^\dagger, a^\dagger a] = -a^\dagger. \tag{1.35}$$

In terms of these ladder operators the Hamiltonian can be rewritten as:

$$H = \hbar\omega_0\left(a^\dagger a + \frac{1}{2}\right). \tag{1.36}$$

We write the eigenstates and eigenvalues of $a^\dagger a$ as:

$$a^\dagger a\,|n\rangle = n\,|n\rangle\,. \tag{1.37}$$

The commutation relations above indicate to us that applying the operators a and $a^\dagger$ to $|n\rangle$ will produce new eigenstates of $a^\dagger a$ with eigenvalues which are either lowered

or raised by 1:

$$\begin{aligned} a^\dagger a a \left|n\right\rangle &= (a a^\dagger a - a)\left|n\right\rangle \\ &= (n-1)a\left|n\right\rangle, \end{aligned} \tag{1.38}$$

$$\begin{aligned} a^\dagger a a^\dagger \left|n\right\rangle &= (a^\dagger a^\dagger a + a^\dagger)\left|n\right\rangle \\ &= (n+1)a^\dagger \left|n\right\rangle. \end{aligned} \tag{1.39}$$

So we see that these operators can be used to add or remove quanta of energy $\hbar\omega_0$ from the system. Furthermore the commutation relations can be used to show:

$$\left\langle n\right| a^\dagger a \left|n\right\rangle = n \tag{1.40}$$

$$\implies a\left|n\right\rangle = \sqrt{n}\left|n-1\right\rangle, \tag{1.41}$$

$$\left\langle n\right| a a^\dagger \left|n\right\rangle = n+1, \tag{1.42}$$

$$\implies a^\dagger \left|n\right\rangle = \sqrt{n+1}\left|n+1\right\rangle. \tag{1.43}$$

Since we expect our system to have a well defined ground state it must be the case that repeated application of the lowering operator will eventually cease to produce lower energy states. This can only be the case if the index n is restricted to integer values and the state $\left|0\right\rangle$ is the ground state. Rather than producing a lower energy state, application of a annihilates this state entirely $a\left|0\right\rangle = 0$.

We now see that the action of these appropriately named ladder operators is to move the system through a discrete ladder of states $\left|n\right\rangle$with energies $E_n = \hbar\omega_0(n + \frac{1}{2})$. Because of the linearity of this system, the states are all equally spaced. As mentioned above, this presents a challenge if we wish to encode information in a particular subspace of states since their transitions cannot be uniquely addressed. For this reason we introduce nonlinearity via the Josephson junction as described below.

1.3 The Cooper Pair Box and the Transmon

Josephson junctions are the primary tool for introducing nonlinearity into superconducting circuits. A Josephson junction consists of two superconductors intersected by a weak link, which could be either an insulator, a normal conductor or a region of weakened superconductivity. Despite the presence this barrier, it is still possible for a supercurrent to flow through the junction via the tunneling of Cooper pairs. In this case the current and voltage across the junction are described by the Josesphson equations [16, 17]:

$$I = I_c \sin\left(\frac{\Phi}{\varphi_0}\right), \qquad V = \frac{d\Phi}{dt} \tag{1.44}$$

in which I_c is known as the critical current of the junction, Φ is the flux as defined above in eq. 1.14 and $\varphi_0 = \frac{\hbar}{2e}$ is the reduced flux quantum. The first Josephson equation displayed above indicates that the junction is an element of inductive type. Using eq. 1.21 we can calculate the potential energy stored by the junction:

$$E_I(\Phi) = -I_c\varphi_0\left(\cos\left(\frac{\Phi}{\varphi_0}\right) - 1\right) \tag{1.45}$$

This energy has a term dependent on the flux Φ as well as a constant offset, which we will neglect in future.

We can now create an anharmonic oscillator by replacing the linear conductor in our harmonic oscillator circuit by a Josephson junction. Such as device is known as a Cooper Pair Box and (CPB) [18, 19, 20] it can be constructed simply by connecting a small superconducting charge island to ground via Josephson junction. The close proximity between the two interfaces of the junction provides the necessary capacitive coupling C. Furthermore we can capacitively couple C_g the charge island to a gate electrode at potential V_g in order to tune an offset charge $q_g = C_g V_g$. The Hamiltonian can be written as:

$$H = \frac{(q-q_g)^2}{2C} - I_c\varphi_0\cos\left(\frac{\Phi}{\varphi_0}\right). \tag{1.46}$$

When dealing with Josephson junctions it is often convenient to use angular coordinates and to measure charge in units of Cooper pair charge $2e$. Therefore we define the variables $\phi = \Phi/\varphi_0$ and $N = q/2e$ which obey the commutation relation $[\phi, N] = i$. We also define the Josephson energy $E_J = I_c\varphi_0$, the charging energy $E_C = e^2/2C$ and the reduced gate charge $N_g = q_g/2e$. The Hamiltonian can be written in a standard form in terms of these quantities:

$$H = 4E_C(N - N_g)^2 - E_J\cos(\phi). \tag{1.47}$$

In the $E_J/E_C \lesssim 1$ regime the eigenstates will not be well localised in the minimum of the junction potential and will therefore be significantly affected by its anharmonicity. The energy levels no longer form an evenly spaced ladder and we can address a specific transition such as between the ground and first excited states.

However, one of the drawbacks of this system is its sensitivity to charge noise. Close to $N_g = 1/2$ we can write an effective Hamiltonian in terms of the $N|0\rangle = 0$ and $N|1\rangle = |1\rangle$ charge states:

$$H \approx 2E_C\big(1 - 2N_g\big)\sigma^z - \frac{E_J}{2}\sigma^x \tag{1.48}$$

where $\sigma^z = |1\rangle\langle 1| - |0\rangle\langle 0|$ and $\sigma^x = |0\rangle\langle 1| + |1\rangle\langle 0|$. The energy gap between the two qubit states is given by $E = \sqrt{E_J^2 + 4E_C^2(2N_g - 1)^2}$.

If noise sources are weakly coupled to the qubit and have short correlation times relative to the qubit dynamics then we can apply the Born-Markov approximation and quantify decoherence in terms of two rates [21, 22]: the relaxation rate Γ_1 and the dephasing rate Γ_ϕ. These are combined to produce the decoherence time $\Gamma_2 = \Gamma_\phi + \Gamma_1/2$. In terms of these rates the evolution of the qubit density matrix is given by [8]:

$$\rho(t) = \begin{pmatrix} |\beta|^2 e^{-\Gamma_1 t} & \alpha^*\beta e^{iEt\hbar - \Gamma_2 t} \\ \alpha\beta^* e^{-iEt\hbar - \Gamma_2 t} & 1 + (|\alpha|^2 - 1)e^{-\Gamma_1 t} \end{pmatrix} \tag{1.49}$$

where the initial state is $|\psi\rangle = \alpha|0\rangle + \beta|1\rangle$.

We can see that the transition frequency is dependent on the gate charge so any random fluctuations in this parameter will cause us the phase between the two qubit states to evolve in an unpredictable way. Over time this causes us to lose track of the phase coherence of our qubit at rate Γ_ϕ. Combined with energy relaxation this leads to an overall decoherence rate Γ_2. This problem can be alleviated to some extent by tuning the gate charge to the optimum point $N_g = 1/2$ at which the transition frequency is only sensitive to charge noise at second order. However this remains a limiting source of noise and the requirement to maintain the gate charge at the optimum point adds extra complexity to the system.

In order to solve this problem a new design was formulated: the transmon [3]. The transmon is almost identical to the CPB except for the addition of a large shunting capacitor in parallel with the junction. This reduces both the anharmonicity of the charge qubit and its sensitivity to charge noise, however whereas the anharmonicity decays only as a power law with respect to E_J/E_C, the charge sensitivity decays exponentially. This allows the fabrication of a charge qubit which is essentially immune to charge noise while still retaining the anharmonicity necessary for operation as a qubit.

Using a tight binding model it has been shown that energy of the mth level of the transmon E_m is well approximated by [3]:

$$E_m(N_g) \approx E_m(N_g = 1/4) - \frac{\varepsilon_m}{2}\cos(2\pi N_g) \tag{1.50}$$

where:

$$\varepsilon_m = E_m(N_g = 1/2) - E_m(N_g = 0). \tag{1.51}$$

Furthermore, the value of ε_m has been studied by examining the $E_J/E_C \gg 1$ asymptotics of the exact solutions of the charge qubit Hamiltonian eq. 1.47, which are

given by the Mathieu functions. The resulting approximation for ε_m is given by:

$$\varepsilon_m \approx (-1)^m E_C \frac{2^{4m+5}}{m!}\sqrt{\frac{2}{\pi}}\left(\frac{E_J}{2E_C}\right)^{\frac{m}{2}+\frac{3}{4}} \exp\Big(-\sqrt{8E_J/E_C}\Big). \tag{1.52}$$

The exponential suppression of ε_m for large values of E_J/E_C is the key result underlying the protection of the transmon against charge noise. Meanwhile, after a fourth order expansion of the junction potential the eigenenergies can be approximated by:

$$E_m \approx -E_J + \sqrt{8E_C E_J}\left(m+\frac{1}{2}\right) - \frac{E_C}{12}(6m^2+6m+3). \tag{1.53}$$

We denote the energy gap between states i and j by $E_{i,j} = E_j - E_i$. From this expression we see that the energy gap between the ground and first excited states is $E_{0,1} = \sqrt{8E_C E_J} - E_C$ while the anharmonicity is $\alpha = E_{1,2} - E_{0,1} = -E_C$. The relative anharmonicity is therefore $\alpha_r = \alpha/E_{0,1} \approx -(8E_J/E_C)^{-1/2}$. Therefore we can see that protecting the transmon against charge noise only leads to a modest reduction in anharmonicity.

The development of this design has allowed the construction of qubits with a coherence time in the 10s or even 100s of microseconds [9]. Yet despite their favourable coherence times, ease of fabrication and ease of operation, the weak anharmonicity of the transmon qubit can pose an issue during gate operations. High power control pulses are liable to scramble the transmon by populating higher energy states. In order to prevent this, weaker drives must be used, but this lengthens the time of gate operations. In the next section we shall consider flux qubits, which have much larger anharmonicities.

1.4 Flux qubits

In basic terms a flux qubit is a superconducting loop whose eigenstates are quantized circulating currents which can be used to encode information [23, 24]. This loop is typically intersected by a multiple Josephson junctions which are necessary for two reasons. First, by providing weak links in the loop they allow the tunneling of flux quanta in and out of the loop, which allows transitions between the persistent

current states. Second, as mentioned previously, the nonlinearity of these junctions is needed to produce an anharmonic ladder of states.

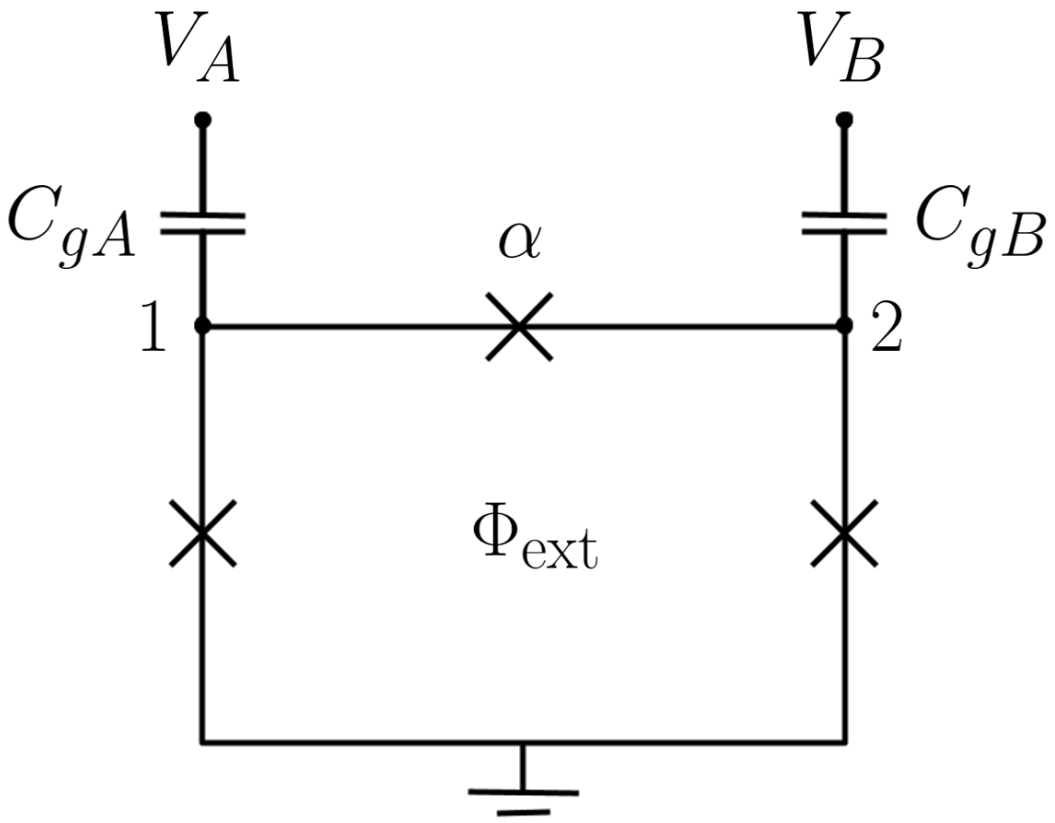

Figure 1.1: The most simple flux qubit design consists of a superconducting ring intersected by three junctions, two of which are identical with Josephson energy E_J while the third has energy αE_J. In the design above we have also included gates A and B which are capacitively coupled to nodes 1 and 2 of the circuit. An externally applied flux Φ_{ext} is linked through the loop.

The most simple flux qubit design [24, 23] (Fig. 1.1) contains three junctions: two of which have energy E_J while the third has energy αE_J. The potential energy of these junctions is given by:

$$V = -E_J\left(\cos\left(\frac{\Phi_1}{\varphi_0}\right)+\cos\left(\frac{\Phi_2}{\varphi_0}\right)+\alpha\cos\left(\frac{\Phi_{\text{ext}}+\Phi_1-\Phi_2}{\varphi_0}\right)\right) \tag{1.54}$$

where Φ_{ext} is the externally applied magnetic flux. For $\alpha > 1/2$ and Φ_{ext} close to $\pi\varphi_0$ this will produce a double well potential whose minima correspond to two states with oppositely circulating currents. Meanwhile the kinetic energy is given

by:

$$T = \frac{1}{2}C_j \sum_j \dot{\Phi}_j^2 - Q_{gA}\dot{\Phi}_A - Q_{gB}\dot{\Phi}_B \tag{1.55}$$

where the sum is taken over the five capacitive elements of the circuit and the voltage across the gate capacitors is given by $\dot{\Phi}_{gA} = V_A - \dot{\Phi}_1$ and $\dot{\Phi}_{gB} = V_B - \dot{\Phi}_2$. The induced gate charges are denoted by Q_{gA} and Q_{gB}. If we write these capacitances as $C_1 = C_2 = C$, $C_3 = \alpha C$ and $C_{gA} = C_{gB} = \gamma C$ and treat Φ_1 and Φ_2 as the coordinates of our system then the conjugate charges take the form:

$$\vec{q} = \frac{\partial L}{\partial \dot{\vec{\Phi}}} \tag{1.56}$$

$$= \boldsymbol{C}\dot{\vec{\Phi}} - \boldsymbol{C_g}\vec{V}_g \tag{1.57}$$

for which we define

$$\boldsymbol{C} = C\begin{pmatrix} 1+\alpha+\gamma & -\alpha \\ -\alpha & 1+\alpha+\gamma \end{pmatrix}, \quad \boldsymbol{C_g} = \gamma C \begin{pmatrix} 1 & 0 \\ 0 & 1 \end{pmatrix} \tag{1.58}$$

and

$$\vec{V}_g = \begin{pmatrix} V_{gA} \\ V_{gB} \end{pmatrix}, \quad \vec{q} = \begin{pmatrix} q_1 \\ q_2 \end{pmatrix}. \tag{1.59}$$

The resulting Hamiltonian is:

$$H = \frac{1}{2}(\vec{q} + \boldsymbol{C_g}\vec{V}_g)^T \boldsymbol{C}^{-1}(\vec{q} + \boldsymbol{C_g}\vec{V}_g)^T + V. \tag{1.60}$$

After quantization an effective model can be produced in terms of the two circulating current states localized in the minima of the double well potential, denoted by $|\circlearrowleft\rangle$ and $|\circlearrowright\rangle$, whose persistent current is labelled I_p The Hamiltonian can then be

written as:

$$H(\Phi_{\text{ext}}) = \frac{\Delta}{2}\sigma^x + I_p\left(\Phi_{\text{ext}} - \frac{\Phi_0}{2}\right)\sigma^z \tag{1.61}$$

where Δ is the tunnel coupling through the potential barrier and σ^x and σ^z are Pauli operators which acting according to:

$$\sigma^x = |\circlearrowleft\rangle\langle\circlearrowright| + |\circlearrowright\rangle\langle\circlearrowleft| \quad \text{and} \quad \sigma^z = |\circlearrowleft\rangle\langle\circlearrowleft| - |\circlearrowright\rangle\langle\circlearrowright|. \tag{1.62}$$

The gap between the eigenstates of this Hamiltonian is given by:

$$E_{0,1} = \sqrt{\Delta^2 + I_p^2(2\Phi_{\text{ext}} - \Phi_0)^2}. \tag{1.63}$$

Typically flux qubits are operated at the optimal point $\Phi_{\text{ext}} = \Phi_0/2$ at which this energy gap is sensitive to external flux variations only at second order.

Further improvements can be made by moving to the Fluxonium qubit [25]. The Fluxonium design is reached by dramatically increasing the number of junctions intersecting the loop. Suppose we include an array of n junctions then for sufficiently large n the Hamiltonian can be approximated by:

$$H \approx 4E_C N^2 - E_J \cos\left(\frac{\Phi_{\text{ext}} + \Phi}{\varphi_0}\right) + \frac{E_L \Phi^2}{2\varphi_0^2} \tag{1.64}$$

where E_L is the effective inductive energy of the junction array. Such qubits are well protected against dephasing due to flux noise and as well as energy relaxation due to charge defects and can achieve excellent coherence times [26, 27], extending even into the range of milliseconds [28].

1.5 Circuit quantum electrodynamics

So far we have introduced the basic types of superconducting qubit but we have not mentioned how to perform readout or control. These are essential operations for quantum information processing and they can be performed using the toolset of circuit quantum electrodynamics (cQED) [1]. In general quantum electrodynamics

is the study of the interactions of light and matter. Circuit quantum electrodynamics is the study of such interactions specifically in the context of superconducting circuits e.g. photons in transmission line or lumped element resonators interacting with systems such as atoms, quantum dots and superconducting qubits.

A simple example of a lumped element resonator is the harmonic oscillator circuit described above in eq. 1.30. It has a single resonance frequency at $\omega = 1/\sqrt{LC}$. On the other hand, a transmission line resonator [29], such as a coplanar waveguide, is more complicated since it can have many interacting modes. A coplanar waveguide consists of a strip of superconducting metal in close proximity to a ground plane. If we denote the inductance and capacitance per unit length by l and c respectively then the speed of light in the resonator is given by $v = 1/\sqrt{lc}$ while its characteristic impedance is given by $Z_0 = \sqrt{l/c}$.

An infinitely long transmission line will support a continuum of modes, but if boundary conditions are imposed then the modes will become quantized. A typical setup is a resonator of length Λ terminated either at one of both ends by weak capacitive couplings to other transmission lines which can be used to probe and measure the resonator. The resonator will then support modes with wavevectors $k = m\pi/\Lambda$ for $m \in \{1,2,3,...\}$. The Hamiltonian describing the resonator is given by:

$$H = \sum_{m=1}^{\infty} m\hbar\omega_1 a_m^\dagger a_m \tag{1.65}$$

where ω_1 is the frequency of the first harmonic and a_m is annihilation operator acting on mode m. Furthermore the current operator at position x is given by [29]:

$$I(x) = I_{\text{zpf},1} \sum_{m=1}^{\infty} i\sqrt{m}\sin(\pi m x/\Lambda)(a_m^\dagger - a_m) \tag{1.66}$$

where $I_{\text{zpf},1} = \omega_1\sqrt{\frac{\hbar}{\pi Z_0}}$ is the zero point fluctuation of the current in the first mode.

Similarly the voltage operator at position x is given by [29]:

$$V(x) = V_{\text{zpf},1} \sum_{m=1}^{\infty} \sqrt{m} \cos(\pi m x/\Lambda)(a_m + a_m^\dagger) \tag{1.67}$$

where $V_{\text{zpf},1} = \omega_1 \sqrt{\frac{\hbar Z_0}{\pi}}$ is the zero point fluctuation of the voltage in the first mode.

These currents and voltages can be used to couple the resonator to other components in a circuit such as various kinds of superconducting qubit. Typically a charge qubit can be capacitively coupled to the voltage on the resonator [30] while a flux qubit can be inductively coupled to its current. In either case it is possible to engineer a coupling described by the Jaynes-Cummings Hamiltonian [31, 32]:

$$H_{\text{JC}} = \hbar\omega_c \left(a^\dagger a + \frac{1}{2} \right) + \frac{1}{2}\omega_q \sigma^z + \hbar g(a^\dagger \sigma^- + a\sigma_+) \tag{1.68}$$

which models a two level system exchanging quanta of energy with a harmonic oscillator. This model can be exactly digaonalized in terms of the states [33]:

$$|+,n\rangle = \cos(\theta_n)\,|\downarrow,n\rangle + \sin(\theta_n)\,|\uparrow,n+1\rangle\,, \tag{1.69}$$

$$|-,n\rangle = -\sin(\theta_n)\,|\downarrow,n\rangle + \cos(\theta_n)\,|\uparrow,n+1\rangle \tag{1.70}$$

and the ground state $|\uparrow,0\rangle$ where $\sigma^z|\uparrow\rangle = -|\uparrow\rangle$, $\sigma^z|\downarrow\rangle = |\downarrow\rangle$, $\Delta = \omega_q - \omega_c$ and $\tan(2\theta_n) = 2g\sqrt{n+1}/\Delta$. The corresponding energies are:

$$E_{\pm,n} = (n+1)\hbar\omega_c \pm \frac{\hbar}{2}\sqrt{4g^2(n+1) + \Delta^2}, \tag{1.71}$$

$$E_{\uparrow,0} = -\frac{\hbar\Delta}{2}. \tag{1.72}$$

This model has proven to be extremely useful in many aspects of quantum information processing and particularly and readout. If we label the detuning $\Delta = \omega_q - \omega_c$ then we can define the dispersive regime of the Jaynes-Cummings model

by $g/|\Delta| \ll 1$. In this regime we can apply the transformation [1]:

$$U = \exp\left(\frac{g}{\Delta}(a\sigma^{+} - a^{\dagger}\sigma^{-})\right) \tag{1.73}$$

to obtain the approximate Hamiltonian:

$$UHU^{\dagger} \approx \hbar\left(\omega_c + \frac{g^2}{\Delta}\sigma^z\right)a^{\dagger}a + \frac{\hbar}{2}\left(\omega_q + \frac{g^2}{\Delta}\right)\sigma^z \tag{1.74}$$

which shows the resonance frequency of the cavity being shifted by $\pm g^2$ *Delta* depending on the state of the qubit. This is the basis for dispersive readout. If $g^2/\Delta > \kappa$ where κ is the linewidth of the cavity resonance then it will be possible to infer the qubit state from a signal transmitted through the cavity [30, 34].

Chapter 2

Critical slowing down and dissipative phase transitions in circuit quantum electrodynamics

2.1 Introduction

The study of dissipative phase transitions has a long and interesting history not only due to their technological applications, such as in the construction of the laser [35, 36, 37], quantum limited amplifiers [38, 39] and optical switches [40, 41, 42], but also due to their theoretical interest since these phase transitions cannot be described by standard techniques such as mean-field theory [43]. A key characteristic of first order dissipative phase transitions is bistability [44, 45, 46, 47]: close to the transition the two phases are metastable [48] and the dynamics of the system are highly sensitive to both its parameters and its initial state [49, 50, 51, 52].

This sensitivity has previously been harnessed in the construction of the Josephson Bifurcation Amplifier (JBA) which has been used in a variety of contexts including qubit readout and magnetometry [39]. In the context of readout, the qubit circuit is coupled to a separate readout circuit consisting of a nonlinear resonator which is driven close to a bifurcation. A small change in the state of the qubit is capable of producing a large change in the field on the nonlinear resonator by altering which metastable state the nonlinear prefers to occupy. This technique

has been applied to readout of transmon [53], flux [54] and quantronium [55] qubits, even reaching single shot readout in the case of the transmon.

Furthermore, subsequent work has shown that it is possible to harness the nonlinearity inherent to a coupled qubit-resonator system to perform single shot qubit readout [49, 56]. In the bistable regime we expect the system to make a sharp transition from a dim state to a bright state as the drive power is increased and the threshold at which this transition occurs was observed to depend sensitively on the initial state of the qubit. In the strongly driven regime the constrast between these bistable states allowed the experimentalists to perform single shot readout.

In the current work we will be examining a coupled-transmon resonator system close to the onset of the bistable regime. Instead of studying qubit readout we will examine the rate at which the system approaches steady state in this regime in order to learn about the dynamics which govern the metastable states. The steady state is reached via rare switching events during which the system transitions from one phase to the other [57, 58]. This can be modelled using the theory of quantum activation in the case of dispersive optical bistability [59]. Since the metastable states may be very long lived, this leads to critical slowing down in the equilibration time of the system. Critical slowing down has already been observed in a circuit-QED lattice [60] and in an ensemble of NV centers coupled to a superconducting cavity [61], and has been modelled in the context of the Bose-Hubbard lattice [62].

Here, we observe critical slowing down in a circuit-QED system with only two degrees of freedom: a transmon qubit [3] coupled to a 3D microwave cavity [63]. The nonlinearity introduced by the qubit causes the cavity to display bistability when a sufficiently strong microwave drive is applied. Within the bistable regime the system divides its time between two metastable states which are known as the bright and dim states according to number of photons occupying the cavity. While the inherent nonlinearity of such a system has been exploited in [49] to achieve high fidelity readout of the qubit state using high drive powers, here we are interested in exploring and understanding the rich quantum dynamics happening at intermediate powers, close to the onset of bistability. We show that, at such powers, the cavity

exhibits critical slowing down, reaching its steady state in a time much longer than the lifetimes of both the qubit and the cavity. We characterize the timescale of this slowdown as a function of driving frequency and power. We discover a new regime of quantum activation in which the slowdown displays a saturation, which can only be explained by taking into account the full quantum description of the transmon. We demonstrate that even a simple superconducting circuit, consisting of only a qubit and a cavity, can be used to explore the rich physics of quantum phase transitions.

The device consists of a transmon qubit embedded in a superconducting aluminium 3D microwave cavity. Measurements of the transmitted signal through the cavity are performed using a standard cQED microwave setup described in Materials and Methods. This system can be described by the generalized Jaynes-Cummings model (GJC) and its Hamiltonian can be written as

$$\begin{aligned} H =& \hbar \sum_n \omega_n |n\rangle\langle n| + \hbar\omega_c a^\dagger a + \hbar \sum_{m,n} g_{m,n} |m\rangle\langle n| (a + a^\dagger) \\ &+ \hbar\varepsilon(a^\dagger e^{-i\omega_d t} + a e^{i\omega_d t}) : \end{aligned} \tag{2.1}$$

a cavity mode of frequency ω_c is coupled with strength $g_{m,n}$ to a transmon qubit whose unperturbed eigenstates can be written in terms of Mathieu functions [3]. Here, we simply denote them by $|n\rangle$ and their eigenenergies by $\hbar\omega_n$. The cavity is represented using the annihilation(creation) operator $a(a^\dagger)$ and is driven by a monochromatic field of strength ε and frequency ω_d. To model environmental noise we use the Lindblad master equation [64]

$$\begin{aligned} \partial_t \rho =& -(i/\hbar)[H,\rho] + (n_c+1)\kappa D(a)\rho + n_c \kappa D(a^\dagger)\rho \\ &+ \gamma_\phi D(b^\dagger b)\rho + (n_t+1)\gamma D(b)\rho + n_t \gamma D(b^\dagger)\rho, \end{aligned} \tag{2.2}$$

where b is the ladder operator acting on the transmon and is defined by $b = \sum_{n=0}^{\infty} \sqrt{n+1}\,|n\rangle\langle n+1|$. The thermal occupations of the transmon and cavity baths

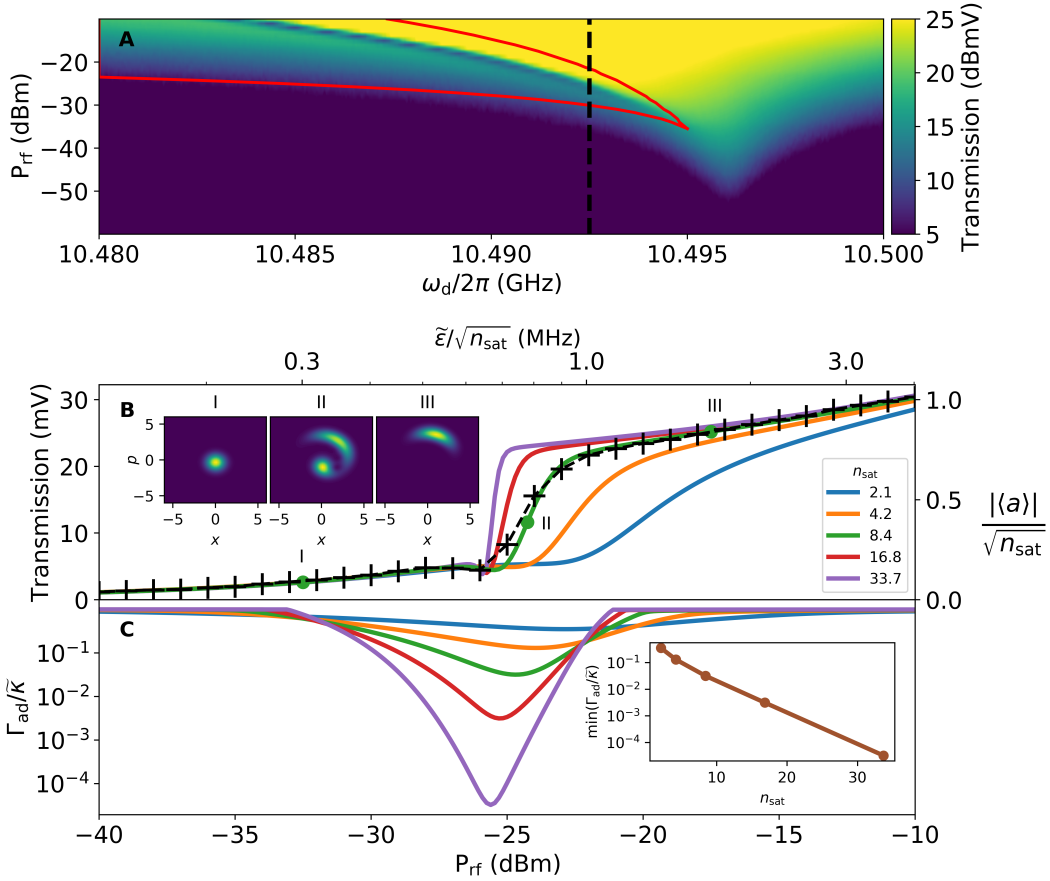

Figure 2.1: Introducing a phase transition in a system with 2 degrees of freedom. **A**: Transmission spectroscopy of the cavity for a range of drive powers and frequencies. At low drive powers we observe a resonance at $\omega_d/2\pi = 10.4960$ GHz. The nonlinearity of the system causes the resonance to shift to lower frequencies as the drive power is increased. The boundaries of the bistable regime are modelled using the mean-field equations of motion of the Duffing oscillator and are displayed in red. Within the bistable regime the cavity displays a sharp transition from a low transmission (dim) to a high transmission (bright) state as the drive power is increased. **B**: Transmitted signal as a function of drive power at $\omega_d/2\pi =$ GHz, indicated by the vertical dashed line in panel **A**. The experimentally measured transmission is indicated by dashed black line and is compared with the results of a Duffing model in green, for which we plot the cavity amplitude divided by the root of the photon saturation number ($|\langle a\rangle|/\sqrt{n_{sat}}$). This model accurately models the transition. The three insets, labelled I, II and III, show the Wigner function of the steady state of the cavity according to the Duffing model at the marked powers. This confirms that the transition from low to high transmission is associated with a transfer of probability between two distinct regions in phase space: the bright and dim states of the cavity. The cavity transmission is also modelled for a range of saturation photon numbers and show that the transition becomes sharper as the n_{sat} increases towards the thermodynamic limit. **C**: Asymptotic decay rate as a function of driving power for different saturation photon numbers. The rate at which system approaches the steady state drops orders of magnitude below its natural relaxation time $\widetilde{\kappa}$, showing that the bistable regime is associated with critical slowing down. The inset shows that this slowdown increases exponentially as we approach the thermodynamic limit.

are denoted by n_t and n_c respectively, while γ and κ are the intrinsic transmon and cavity relaxation rates, and γ_ϕ is the intrinsic transmon dephasing rate.

At sufficiently low drive powers the transmon is confined to its ground state. The system can be treated as a single Duffing oscillator with a Kerr nonlinearity [65] whose Hamiltonian and master equation can be written as (Appendix 2.A):

$$\widetilde{H} = \hbar\widetilde{\omega}_c a^\dagger a + \frac{1}{2}\hbar K a^\dagger a^\dagger a a + \hbar\widetilde{\varepsilon}(a^\dagger e^{-i\omega_d t} + a e^{i\omega_d t}), \tag{2.3}$$

$$\partial_t \rho = -(i/\hbar)[\widetilde{H}, \rho] + (\widetilde{n}_c + 1)\widetilde{\kappa} D(a)\rho + \widetilde{n}_c \widetilde{\kappa} D(a^\dagger)\rho + \widetilde{\kappa}_\phi D(a^\dagger a)\rho. \tag{2.4}$$

In this simplified model, the dispersive coupling with the transmon shifts the cavity frequency to $\widetilde{\omega}_c$, and introduces a Kerr nonlinearity K. The thermal occupation of the cavity bath is denoted by $\widetilde{n}_c$ and the cavity relaxation and dephasing rates are represented by $\widetilde{\kappa}$ and $\widetilde{\kappa}_\phi$ respectively.

A further simplification can be made with the mean-field approximation i.e. we assume the cavity to be in a coherent state $\rho = |\alpha\rangle\langle\alpha|$ and substitute this into $\partial_t \alpha = \mathrm{Tr}(a\partial_t \rho)$. We obtain the classical equation of motion in a frame rotating with the drive:

$$\partial_t \alpha = -(\widetilde{\kappa} + i(\widetilde{\omega}_c - \omega_d) + iK|\alpha|^2)\alpha - i\widetilde{\varepsilon}, \tag{2.5}$$

and find the steady state cavity amplitude

$$\alpha = -\frac{i\widetilde{\varepsilon}}{\widetilde{\kappa} + i(K|\alpha|^2 + \widetilde{\omega_c} - \omega_d)}. \tag{2.6}$$

At weak drive powers the occupation of the cavity is low, so the nonlinear term $K|\alpha|^2$ in Eq. 2.6 vanishes and the standard Lorentzian response is obtained. However, when the number of photons in the cavity approaches the saturation number $n_{\mathrm{sat}} = |\omega_c - \omega_d|/K \sim |\alpha|^2$, the nonlinearity becomes significant and the equation of motion may admit two stable steady state solutions. The system enters the bistable regime.

In the mean-field approximation the lifetimes of these states are infinitely long,

but if fluctuations are taken into account these states become metastable and the system may undergo rare escape events, switching from one state to the other. Both metastable states may coexist with each other over a range of drive amplitudes and the time taken for the system to reach a steady state will be determined by their lifetimes. These lifetimes can be much greater than the lifetime of the cavity and this gives rise to the phenomenon of critical slowing down. If an appropriate thermodynamic limit is taken, this time diverges and the model produces a first order dissipative phase transition in which the two phases may coexist only at a single drive amplitude [47, 48, 66].

2.2 Results

2.2.1 Cavity response in the bistable regime

We now show evidence of such a first order phase transition in our system, containing only two degrees of freedom. We measure the signal transmitted through the cavity as a function of driving frequency (ω_d) and power (P_{rf}) as shown in Fig. 2.1A. We find that at low power the cavity line is dispersively shifted to $\omega_{\mathrm{r}}/2\pi = 10.4960$ GHz and has the Lorentzian shape which is typical of linear response. As the driving power increases, the lineshape shifts to lower frequencies and nonlinear features appear. The effective Kerr nonlinearity of the cavity is found to be $K = -0.4221$ MHz and its relaxation rate is $\widetilde{\kappa}/2\pi = 1.040$ MHz. Above $P_{\mathrm{rf}} = -29$ dBm a dip in the transmitted signal is observed. This indicates the presence of the bistable regime and is due to destructive interference between the two metastable states of the cavity [45, 46]. The boundaries of this regime are modelled using the mean-field equations of motion derived from the Duffing approximation and are shown by the red lines. The bistable regime emerges just below the resonance frequency at a drive power of $P_{\mathrm{rf}} = -35$ dBm and opens up over a wider range of frequencies as the drive power increases.

Fig. 2.1B shows the signal transmitted through the cavity (black crosses) as a function of the drive power at $\omega_d/2\pi = 10.4925$ GHz. At this drive frequency we calculate a saturation photon number of $n_{\mathrm{sat}} = 8.4$. We observe a sudden change in

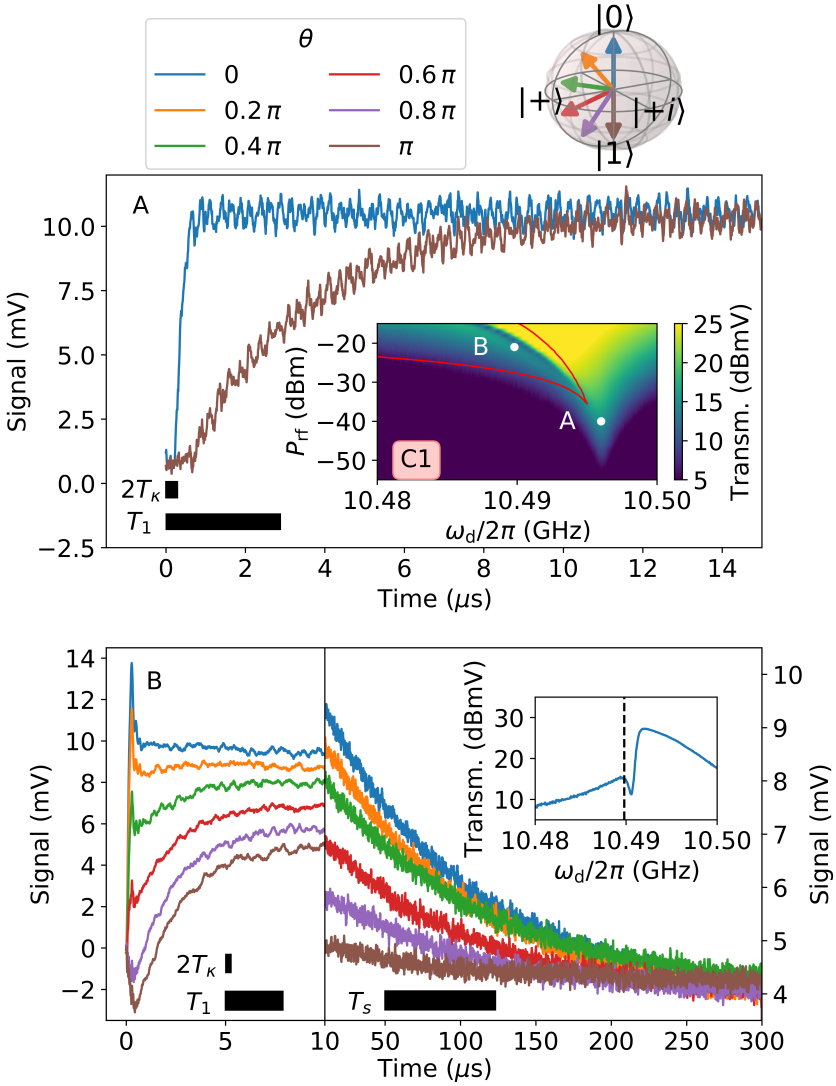

Figure 2.2: Averaged transient response of the cavity outside and inside the bistable regime during the 1st cooldown. The inset in panel A shows transmission spectroscopy of the cavity for a range of drive powers and frequencies. The mean-field Duffing limits of the bistable regime are displayed in red and the locations at which the data in panels A and B were taken are indicated by the white dots. (A): The cavity is driven at the low power resonance $\omega_d/2\pi = 10.4960$ GHz and $P_{\rm rf} = -40$ dBm. The signal in blue (brown) is the transient response measured with the qubit initialized in its ground (first excited) state. The transient response is governed by the timescale $2T_\kappa = 0.29$ μs if the transmon is in the ground state, whereas it is governed by $T_1 = 2.89$ μs if the transmon is in the first excited state. (B): Transient responses for different initial qubit states in the bistable regime at $P_{\rm rf} = -21$ dBm. The inset shows spectroscopy of the cavity at this drive power with the drive frequency $\omega_d/2\pi = 10.4898$ GHz indicated by the dashed line. The transient response is divided into two parts. There is an initial fast response with a time scale ranging from T_κ to T_1 depending on the initial transmon state, followed by a slow decay towards steady state over a timescale $T_s = 73.2$ μs, obtained from an exponential fit, which is much longer than both the transmon and cavity lifetimes. This critical slowing down allows us to distinguish the transients for different transmon states for over 100 μs.

transmission at $P_{rf} = -25$ dBm in which the cavity switches from a low amplitude (dim) state to a high amplitude (bright) state. This transition is accurately modelled by the Duffing master equation (Eq. 3.2), the results of which are displayed by the green line.

We can make a connection between this behaviour and the theory of phase transitions by defining the thermodynamic limit in which the saturation photon number n_{sat} goes to infinity. This is achieved by rescaling the drive and nonlinearity according to $\varepsilon \to \sqrt{\lambda}\varepsilon$ and $K \to K/\lambda$, which in turn gives $n_{sat} \to \lambda n_{sat}$ [43, 67, 47]. The simulated cavity amplitude is displayed for a range of values of n_{sat} and, as expected, we observe that the transition becomes sharper as the system moves towards the thermodynamic limit, which is typical of first order phase transitions.

We are interested in exploring the system dynamics within this bistable regime, where the steady state consists of a mixture of bright and dim states. We can form an effective master equation by writing the state of the system as

$$\rho(t) = p_b(t)\rho_b + p_d(t)\rho_d \tag{2.7}$$

where ρ_b and ρ_d are the bright and dim states, and p_b and p_d are their occupation probabilities. We can then write a simple rate equation for evolution of the state

$$\begin{pmatrix} \partial_t p_b \\ \partial_t p_d \end{pmatrix} = \begin{pmatrix} -\Gamma_{b\to d} & \Gamma_{d\to b} \\ \Gamma_{b\to d} & -\Gamma_{d\to b} \end{pmatrix} \begin{pmatrix} p_b \\ p_d \end{pmatrix}, \tag{2.8}$$

in which occasional fluctuations allow the system to switch between states at the rates $\Gamma_{b\to d}$ and $\Gamma_{d\to b}$ [46, 58]. The system reaches a steady state when the occupation probabilities have reached equilibrium. The approach to this steady state is governed by

$$\begin{pmatrix} p_b \\ p_d \end{pmatrix} = \frac{1}{\Gamma_{ad}} \begin{pmatrix} \Gamma_{d\to b} \\ \Gamma_{b\to d} \end{pmatrix} + Ae^{-\Gamma_{ad}t} \begin{pmatrix} 1 \\ -1 \end{pmatrix}, \tag{2.9}$$

where the coefficient A is determined by the initial system conditions. Γ_{ad} is referred

to as the asymptotic decay rate and it is given by

$$\Gamma_{\mathrm{ad}} = \Gamma_{\mathrm{d}\to\mathrm{b}} + \Gamma_{\mathrm{b}\to\mathrm{d}}. \tag{2.10}$$

Γ_{ad} is calculated by extracting the gap in the Liouvillian superoperator [48, 60], derived from the Duffing master equation (Eq. 3.2). Fig. 2.1C shows the asymptotic decay rate as a function of drive powers for different photon saturation numbers. We find that, within the bistable regime, the asymptotic decay rate drops far below the cavity decay rate [68]. This effect is known as critical slowing down and is characteristic of the phase transition. Furthermore, the asymptotic decay rate is exponentially suppressed as n_{sat} increases, indicating that ever larger fluctuations are required to cause switching between the states.

2.2.2 Critical slowing down

Measurements of critical slowing down are performed by recording the transient response of the cavity when a step function drive pulse is applied. Fig. 2.2 shows the average cavity response outside (A) and inside (B) the bistable regime. Fig. 2.2A shows the response at the cavity resonance at $P_{\mathrm{rf}} = -40$ dBm with the transmon initialized in either the ground state (blue line) or the first excited state (brown line). The timescale over which the cavity responds shows a clear dependence on the transmon state. When the transmon starts in the ground state the cavity reaches equilibrium over a timescale $2\ T_\kappa = 2/\kappa = 0.29\ \mu$s, set by the cavity relaxation rate κ, whereas when the transmon is initialized in the first excited state, the drive is initially off resonant with the cavity and the transmon must relax over a time T_1 before the system can reach equilibrium.

Fig. 2.2B shows that the dynamics changes significantly if the system is driven at higher powers. The cavity is now driven at $\omega_d/2\pi = 10.4898$ GHz and $P_{\mathrm{rf}} = -21$ dBm. The inset displays the spectrum at this drive power and the dashed line indicates the drive frequency, which is chosen such that the system is in the bistable regime as signalled by the dip in transmission. The cavity response is now governed by multiple timescales. Initially, there is a fast rise in the cavity

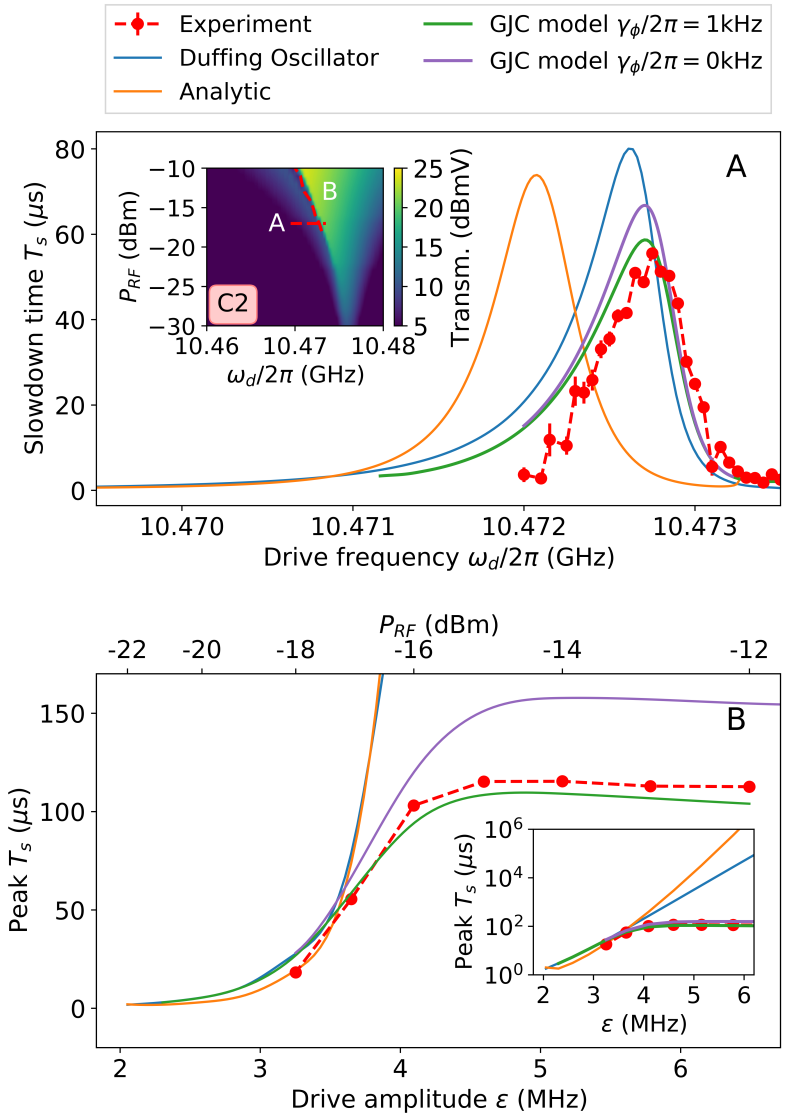

Figure 2.3: Measuring and modelling the critical slowing down time. (A): Critical slowing down time T_s in the bistable regime as a function of driving frequency at $P_{rf} = -17$ dBm during the 2nd cooldown, during which the qubit frequency had shifted to 8.7965 GHz and the low power resonance of the cavity had shifted to 10.4761 GHz. The red points represent the experimental data, which we compare with the results of master equation calculations applied to the Duffing oscillator (blue line) and the GJC model with transmon dephasing (green line) and without (purple line). We also display the results of previous analytical theory of switching rates for the Duffing oscillator (orange line) [59]. At this power both the master equation and the analytical calculations qualitatively reproduce the experimental values of T_s. The horizontal dashed line in the inset shows the location of our measurements within the overall cavity spectrum. (B): Maximum value of T_s for different drive amplitudes (red points). These data were collected along the diagonal dashed line in the inset of panel A. As the drive power increases beyond -17 dBm, T_s reaches a saturation at a value of $115\,\mu$s, that is consistent with the simulations based on the GJC model with transmon dephasing (green line). Removing the dephasing by setting $\gamma_\phi = 0$ (purple line) does not change the power at which saturation occurs but it does raise the upper limit on T_s. Meanwhile analytical (orange line) and master equation (blue line) calculations with the Duffing approximation predict that T_s rises exponentially with drive amplitude, as can be seen using the logarithmic scale of the inset.

transmission over a time ranging from T_κ to T_1 depending on the initial state of the qubit. However, after this fast response we observe critical slowing down: a gradual decay towards equilibrium over a time much longer than both the cavity and qubit lifetimes. We denote the time constant over which the system reaches equilibrium by $T_s = 1/\Gamma_{ad}$. By initializing the transmon in a range of initial states, we show that the cavity retains a memory of the initial transmon state for over 100 μs, indicating our proximity to a phase transition.

Next, we characterize the dependence of the critical slowing down T_s on both driving frequency and power within the bistable regime and we model our findings using a range of approaches. We can either exploit the analytical theory of quantum activation for a Duffing oscillator, as provided in [59] or we can use the master equations for the Duffing and GJC models. In this latter approach we rewrite the GJC master equation as $\partial_t \rho = \mathscr{L}\rho$ where $\mathscr{L}$ is the Liouvillian superoperator. The eigenbasis of $\mathscr{L}$ can be used to express the state of the system as

$$\rho(t) = \sum_n c_n e^{-(\Gamma_n + i\omega_n)t} \rho_n \tag{2.11}$$

where $\mathscr{L}\rho_n = -(\Gamma_n + i\omega_n)\rho_n$. At long times the state will be dominated by the steady state ρ_{ss} and the asymptotically decaying state ρ_{ad}. In this limit we write the state as:

$$\rho(t) = \rho_{ss} + c_{ad} e^{-\Gamma_{ad} t} \rho_{ad}. \tag{2.12}$$

While for the Duffing model it is possible to extract Γ_{ad} by diagonalizing the Liouvillian, due to the larger Hilbert space size of the GJC model, Γ_{ad} is extracted by integrating the master equation (Eq. 2.2) for a sufficiently long time. We are hence able to compare the experimentally attained values of critical slowing down time with simulated values. Fig. 2.3A shows the measured valued of T_s (red circles) as a function of the drive frequency ω_d along the dashed line in the spectroscopy inset, which is located at a drive power of $P_{rf} = -17$ dBm. We find that T_s reaches a maximum close to the dip in the cavity spectrum. This is expected, since the dip is a key signature of the coexistence of the two phases in our transition.

We compare our measurements with master equation simulations applied to a Duffing oscillator model (blue line) and to the GJC model with (green line) and without (purple line) transmon dephasing. We also compare our data to results attained from the analytical theory of quantum activation for a Duffing oscillator (orange line) [59]. At this drive power we find that all of our models give at least qualitative agreement with the measured dependence of critical slowing down on frequency, but only the GJC model is able to model this effect quantitatively.

However, if we plot how the maximum value of T_s varies with the amplitude of the drive, as shown in Fig. 2.3B, we observe a significant divergence between our data and the values attained using the Duffing model. Whereas the theory of the Duffing oscillator predicts that T_s should increase exponentially with the drive, we instead observe that, at sufficiently strong drive amplitudes, T_s saturates. To account for this difference we require the full GJC model. We find that the master equation predicts the same saturation in T_s as found in experiment when we explicitly include the transmon in the simulation.

Furthermore, we see that the level at which this saturation occurs is highly sensitive to the pure dephasing rate of of the transmon. A peak of $T_s = 158$ μs is obtained from the master equation when we don't include pure dephasing of the transmon, however this falls to $T_s = 109$ μs when we take a pure dephasing rate of $\gamma_\phi = 1$ kHz. We might naively consider such a small rate to be insignificant compared to the coherence time of the transmon, which was measured to be $T_2 = 2.37$ μs, however the large change in T_s suggests that the switching rates of the metastable states are strongly influenced by the decoherence channels to which the transmon is coupled.

2.3 Discussion

Clearly, the coupled transmon-resonator system is governed by essentially different activation dynamics from the Duffing oscillator. In order to shed light on the dissimilarity between the Duffing model and the GJC model we examine the switching rates $\Gamma_{b\to d}$ and $\Gamma_{d\to b}$ more closely. In order to obtain these rates it is necessary to

first find the steady state and extract the occupation probabilities $p_{\mathrm{b}}(t \to \infty)$ and $p_{\mathrm{d}}(t \to \infty)$. We can then calculate the switching rates $\Gamma_{\mathrm{d}\to\mathrm{b}}$ and $\Gamma_{\mathrm{b}\to\mathrm{d}}$ according to:

$$\Gamma_{\mathrm{d(b)}\to\mathrm{b(d)}} = p_{\mathrm{d(b)}}(t \to \infty)\Gamma_{\mathrm{ad}}. \tag{2.13}$$

The occupation probabilities can be extracted using the asymptotically decaying and steady states (Appendix 2.B). The resulting rates are displayed in Fig. 2.4B, which shows $\Gamma_{\mathrm{d}\to\mathrm{b}}$ and $\Gamma_{\mathrm{b}\to\mathrm{d}}$ as a function of frequency at a driving power of $P_{\mathrm{rf}} = -14$ dBm for both the Duffing and the GJC model. Whereas $\Gamma_{\mathrm{d}\to\mathrm{b}}$ is in close agreement between the two models, $\Gamma_{\mathrm{b}\to\mathrm{d}}$ is significantly greater in the GJC model. This limits the critical slowing down time according to Eq. (2.10) and leads to the saturation seen in Fig. 2.3B. It also indicates that the bright state has a shorter lifetime in the GJC model.

The Wigner function for three cavity steady states using the GJC model is shown in Fig. 2.4A. We observe that, at low drive frequencies, the dim state is the main contributor to the overall state of the system; this is consistent with $\Gamma_{\mathrm{b}\to\mathrm{d}}$ dominating over $\Gamma_{\mathrm{d}\to\mathrm{b}}$. At higher drive frequencies the reverse is true, while at some intermediate drive frequency the two bistable states are equally occupied and the switching rates are balanced.

Prior work suggests that the instability of the bright state increases with the nonlinearity of the ladder of states in the vicinity of the wave-packet [51]. The instability of the bright state in the GJC model may be due to extra nonlinearity which is present when the transmon becomes excited. It may also be due to backaction of the resonator on the transmon which occurs when the occupation of the resonator increases. This can take the form of measurement dephasing [69, 70], whereby fluctuations in the resonator occupation can cause loss of phase coherence of the transmon via the AC Stark effect; or via dressed-dephasing [71], in which pure dephasing of the transmon exposes it to additional relaxation and heating from the resonator. These phenomena have previously been explored in the nonlinear regime [72] and future work could use this framework to explore how these additional dephasing mechanisms relate to the observed saturation.

In summary, we have explored the rich quantum activation dynamics happening at an intermediate driving regime in cQED. We have observed a phase transition in our system, which contains only two degrees of freedom: a transmon qubit coupled to a microwave cavity. A key signature of this transition is critical slowing down, in which the time taken for the system to reach a steady state can extend far beyond the natural lifetime of the qubit or cavity. We have measured the slowdown time for a wide range of powers and frequencies, and we have compared our results with simulations. We found that the transition and its associated critical slowing down is well modelled by the Duffing approximation at low drive powers. However, at higher drive powers, we observed a saturation in the critical slowing down time, which can only be captured by the full GJC model.

It is known that in this regime the transmon becomes highly excited and starts to participate in the dynamics [73] so it is no longer valid to apply the Duffing approximation. An accurate model must include the quantum fluctuations of the qubit and the resulting destabilisation of the bright state which this causes. Currently, there exists no analytical theory for the switching rates in the bistable regime of a cavity coupled to spins or multilevel systems and this suggests that one avenue of future work could focus on extending the existing theory for the Duffing oscillator to these models. Moreover, we link the critical slowing down to the switching rates between the two metastable states and show how these differ for the GJC and Duffing models. This experiment is a powerful demonstration of the versatility of superconducting circuits, showing that even with few degrees of freedom it is possible to explore rich nonlinear physics and phenomena such as dissipative phase transitions.

2.4 Materials and Methods

A two-port Al microwave cavity holds a lithographically patterned Al transmon qubit, that is fabricated on a sapphire substrate. The transmon qubit consists of two Al pads of dimensions $350\,\mu$m by $450\,\mu$m connected by an Al/AlOx/Al Josephson junction, that is patterned using standard e-beam lithography and double-shadow

evaporation techniques. The cavity is thermally anchored to the 10 mK plate of a dilution refrigerator. Input signals are heavily cryogenically attenuated to reduce thermal noise, and measurements of the signal transmitted through the cavity are made via cryogenic circulators and a low noise HEMT amplifier, with the signal finally being recorded as a voltage with an analog-to-digital converter (ADC).

Measurements were collected during two successive cooldowns. During the 1st cooldown (C1), spectroscopy of the transmon reveals its lowest transition to be $\omega_{01}/2\pi = 9.1932$ GHz with anharmonicity $\alpha/2\pi = -203.6$ MHz. The bare resonance frequency of the cavity is $\omega_c/2\pi = 10.4263$ GHz and its quality factor is found to be $Q = 7900$. The relaxation and dephasing times of the transmon are $T_1 = 2.89$ μs and $T_2 = 2.37$ μs respectively. During the 2nd cooldown (C2) the system is described by a GJC model with the following parameters: $\omega_c/2\pi = 10.423$ GHz, $g_0/2\pi = 295$ MHz, $\kappa = 1.432$ MHz, $\gamma = 33$ kHz, $\gamma_\phi = 1$ kHz, $n_c = 0.01$ and $n_t = 0.02$. The eigenstates of the transmon were produced using a Josephson energy of $E_J/2\pi = 46.7$ GHz and a charging energy of $E_C/2\pi = 221$ MHz [3]. Applying the Duffing approximation to this system we find $\widetilde{\omega}_c/2\pi = 10.4761$ GHz, $K/2\pi = -0.152$ MHz, $\widetilde{\kappa}/2\pi = 1.387$ MHz, $\widetilde{\kappa}_\phi/2\pi = 1.02$ Hz and $\widetilde{n}_c = 0.0100$.

Contributions

Giovanna Tancredi performed the experiments in the group of Peter Leek at the Clarendon Laboratory, University of Oxford. Paul Brookes carried out the numerical and theoretical studies and assisted during data collection. Joseph Rahamim fabricated the sample. Andrew Patterson optimized the FPGA measurement setup. Martina Esposito provided support for analyzing the results. Themistoklis Mavrogordatos contributed to understanding the theory. Eran Ginossar, Peter Leek and Marzena Szymanska supervised the project.

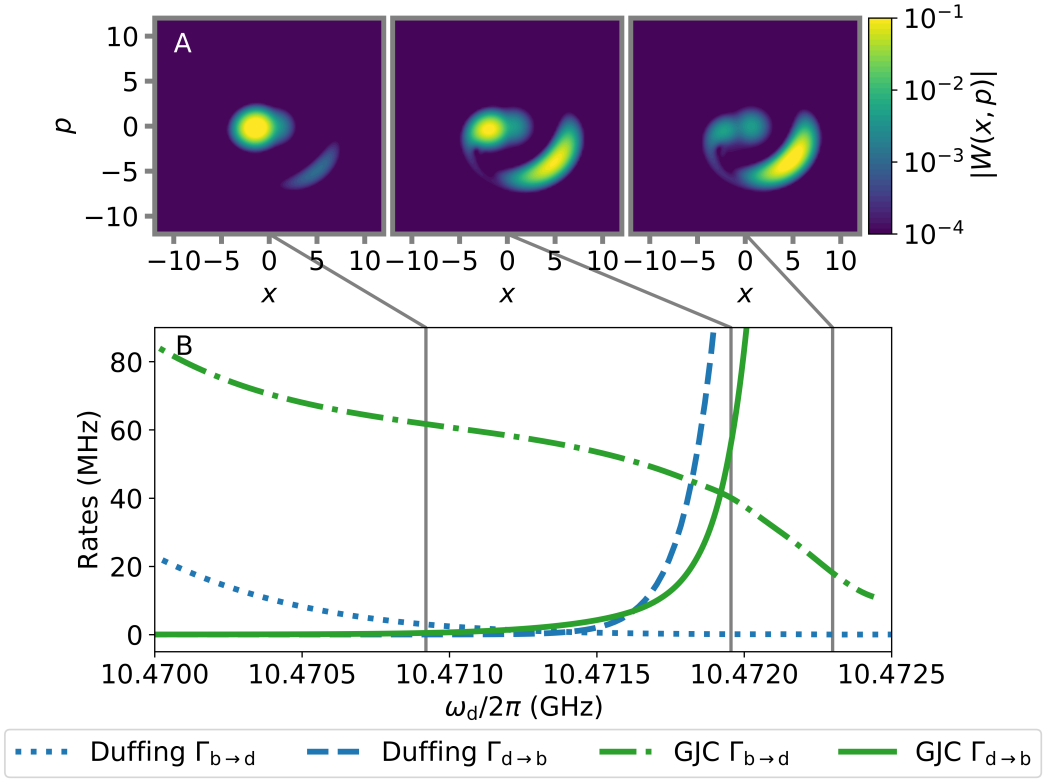

Figure 2.4: Relating the steady state Wigner to the switching rates. (A): Steady state cavity Wigner functions produced using the GJC model at $P_{\mathrm{rf}} = -14$ dBm. At $\omega_d/2\pi = 10.4709$ GHz the steady state consists mainly of the dim state, which corresponds to the peak near the origin. However, as we increase the drive frequency the occupation of the bright state increases as well. At $\omega_d/2\pi = 10.4720$ GHz the occupations of the bistable states are approximately equal and at $\omega_d/2\pi = 10.4723$ GHz the bright state is dominant. (B): Switching rates between metastable state as a function of driving frequency. Whereas $\Gamma_{\mathrm{d}\to\mathrm{b}}$ is similar in both the Duffing and the GJC models, $\Gamma_{\mathrm{b}\to\mathrm{d}}$ is significantly different. In the GJC model $\Gamma_{\mathrm{b}\to\mathrm{d}}$ is much greater compared to the Duffing model. This explains the saturation we observe in T_{s}.

Appendix

2.A Performing the Duffing approximation

In the main text we approximate our system as a Duffing oscillator in order to obtain a benchmark showing the dynamics of a single non-linear oscillator in the bistable regime. This model is used to calculate how the critical slowing down time varies with drive amplitude, as displayed in Fig. 2, and how the switching rates between the bistable states vary drive frequency, shown in Fig. 3. To map our system to a Duffing oscillator we project the GJC Hamiltonian onto a low-energy subspace and identify a Kerr nonlinearity in the resulting spectrum. This subspace consists of the eigenstates of the GJC Hamiltonian for which the transmon is close to the ground state. The first step is to identify these states. We start by writing the the Hamiltonian in the form:

$$H = H_0 + H_{\text{int}} \tag{2.14}$$

where H_0 describes the bare cavity and transmon, and H_{int} describes the interaction between them. These components are given by [3]:

$$H_0 = \hbar\omega_c a^\dagger a + \hbar \sum_{n=0}^{\infty} \omega_n |n\rangle\langle n| \tag{2.15}$$

$$H_{\text{int}} = \hbar \sum_{n=0}^{\infty} g_n \left(a |n+1\rangle\langle n| + a^\dagger |n\rangle\langle n+1| \right). \tag{2.16}$$

If the interaction is turned off by setting $g_n = 0$ then the eigenstates of H are simply products of the eigenstates of the bare cavity and transmon with eigenstates and

eigenenergies given by:

$$H_0 |m\rangle |n\rangle = E_{mn} |m\rangle |n\rangle \tag{2.17}$$

$$E_{mn} = \hbar(m\omega_c + \omega_n) \tag{2.18}$$

where m denotes the number of photons in the cavity and n denotes the number of excitations in the transmon. For finite strength interactions we enter the dispersive regime, which is defined by $|g_n/\Delta_n| \ll 1$ where the detuning is given by

$$\Delta_n = \omega_{n+1} - \omega_n - \omega_c. \tag{2.19}$$

Provided that the interaction strength is sufficiently weak we can continue to label the eigenstates by the number of cavity and transmon excitations they carry and if the system is weakly driven close to the cavity resonance then the only state which will take part in the dynamics are those for which the transmon is in the dressed ground state. These states form a ladder of dressed cavity states which define the low-energy subspace upon which we can project our model. We define the projector by:

$$\Pi = \left(|\psi_{0,0}\rangle\langle\psi_{0,0}| , |\psi_{1,0}\rangle\langle\psi_{1,0}| , |\psi_{2,0}\rangle\langle\psi_{2,0}| , ... \right) \tag{2.20}$$

where $|\psi_{mn}\rangle$ represents the eigenstate of H which can be smoothly transformed to $|m\rangle |n\rangle$ by turning off H_{int}. Using this projector we obtain the low-energy model:

$$\widetilde{H} = \Pi^\dagger H \Pi \tag{2.21}$$

$$= \hbar\widetilde{\omega}_c a_0^\dagger a_0 + \frac{1}{2}\hbar K a_0^\dagger a_0^\dagger a_0 a_0 + \mathscr{O}\left((g_m/\Delta_m)^6\right). \tag{2.22}$$

where the ladder operator in the projected subspace is defined by

$$a_0 = \sum_{n=1}^{\infty} \sqrt{n} |\psi_{n-1,0}\rangle\langle\psi_{n,0}| . \tag{2.23}$$

This Hamiltonian describes a Duffing oscillator with a frequency $\widetilde{\omega}_c$ and a Kerr nonlinearity K [52]. If we use the GJC model parameters given in Table 1 of the

main text then the Duffing model parameters we obtain are shown in Table S1 below. This table also includes the rescaled drive amplitude $\widetilde{\varepsilon}$ which arises when we add a driving term to H_0 of the form:

$$H_d(t) = \hbar\varepsilon(a^\dagger e^{-i\omega_d t} + a e^{i\omega_d t}). \tag{2.24}$$

We find that this transforms to a similar driving term in the Duffing Hamiltonian given by

$$\widetilde{H}_d(t) = \hbar\widetilde{\varepsilon}(a_0^\dagger e^{-i\omega_d t} + a_0 e^{i\omega_d t}). \tag{2.25}$$

The drive amplitude in the projected space $\widetilde{\varepsilon}$ is given by $r_a\varepsilon$ where r_a is calculated according to:

$$\Pi^\dagger a \Pi = r_a a_0 + \mathscr{O}\big((g_m/\Delta_m)^4\big) \tag{2.26}$$

Next we must consider the Lindblad operators which describe the effects of environmental interactions. We have already considered a, but the remaining operators can be projected into the low-energy subspace as follows:

$$\Pi^\dagger b \Pi = r_b a_0 + \mathscr{O}\big((g_m/\Delta_m)^2\big) \tag{2.27}$$

$$\Pi^\dagger b^\dagger b \Pi = r_{nb} a_0^\dagger a_0 + \mathscr{O}\big((g_m/\Delta_m)^2\big). \tag{2.28}$$

From Eqs. (2.26) and (2.27) we see that both a and b contribute to the annihilation operator in the low-energy subspace a_0. The implication is that in the basis of dressed cavity states both κ and γ contribute to relaxation, as expected from prior work on the dressed state formalism in the Jaynes-Cummings model [33]. The coefficients of the Lindblad operators in the low-energy subspace are then given by

$$a_0 : \ \sqrt{(1+\widetilde{n}_c)\widetilde{\kappa}} = \sqrt{r_a^2(1+n_c)\kappa + r_b^2(1+n_t)\gamma} \tag{2.29}$$

$$a_0^\dagger : \ \sqrt{\widetilde{n}_c\widetilde{\kappa}} = \sqrt{r_a^2 n_c\kappa + r_b^2 n_t\gamma} \tag{2.30}$$

$$a_0^\dagger a_0 : \ \sqrt{\widetilde{\kappa}_\phi} = \sqrt{r_{nb}^2\gamma_\phi} \tag{2.31}$$

We use these equations to calculate two sets of Duffing model parameters to describe our system during the two cooldowns of the experiment. For the first cooldown we found $\widetilde{\omega}_c/2\pi = 10.4961$ GHz, $K/2\pi = -0.422$ MHz, $\widetilde{\varepsilon} = 0.971\varepsilon$, $\widetilde{\kappa}/2\pi = 1.040$ MHz, $\widetilde{\kappa}_\phi/2\pi = 56.4$ Hz and $\widetilde{n}_c = 0.0293$. For the second cooldown we found $\widetilde{\omega}_c/2\pi = 10.4761$ GHz, $K/2\pi = -0.152$ MHz, $\widetilde{\varepsilon} = 0.984\varepsilon$, $\widetilde{\kappa}/2\pi = 1.387$ MHz, $\widetilde{\kappa}_\phi/2\pi = 31.9$ Hz and $\widetilde{n}_c = 0.0100$.

2.B Obtaining the occupation probabilities of the bright and dim states

By integrating the Duffing or GJC master equation for a time t we obtain the state $\rho(t)$. If t is much longer than both the caivty and transmon lifetimes then this state can be written as

$$\rho(t) = \rho_{\rm ss} + c_{\rm ad} e^{-\Gamma_{\rm ad} t} \rho_{\rm ad} \tag{2.32}$$

where the steady state is an unknown mixture of bright and dim states which we write as

$$\rho_{\rm ss} = p\rho_{\rm b} + (1-p)\rho_{\rm d} \tag{2.33}$$

and the asymptotically decaying state is given by

$$\rho_{\rm ad} = \rho_{\rm b} - \rho_{\rm d}. \tag{2.34}$$

This allows us to write $\rho(t)$ as another unknown mixture of bright and dim states

$$\rho(t) = q\rho_{\rm b} + (1-q)\rho_{\rm b}. \tag{2.35}$$

Using the steady state and master equation solvers in the QuTiP package [74] we can obtain both $\rho(t)$ and ρ_{ss}. A mixture of these states is written as

$$\tau(A) = \rho_{\mathrm{ss}} - A\rho(t) \tag{2.36}$$

$$= (p - Aq)\rho_{\mathrm{b}} + (1 + Aq - p - A)\rho_{\mathrm{d}}. \tag{2.37}$$

Both ρ_{d} and ρ_{b} are positive semidefinite and we assume that they are orthogonal, which is a good approximation provided that the cavity is sufficiently strongly driven so that they are well separated. Hence the mixture is positive semidefinite if and only if both $p - Aq \geq 0$ and $1 + Aq - p - A \geq 0$. The limits on this range are $A_{\mathrm{d}} = p/q$ and $A_{\mathrm{b}} = (1-p)/(1-q)$, at which points τ consists of solely of the dim state or the bright state respectively. Outside this range the coefficient of at least one of the bistable states will be negative. Hence we can obtain A_{d} and A_{b} by checking the spectrum of τ for negative eigenvalues at different values of A. Finally we obtain

$$p = \frac{A_{\mathrm{d}}(A_{\mathrm{b}} - 1)}{A_{\mathrm{b}} - A_{\mathrm{d}}}. \tag{2.38}$$

This method provides a fast and accurate means of extracting the occupation probabilities of the bright and dim states in the steady state. When the occupation of the cavity is sufficiently small it can also be benchmarked against quantum trajectory methods in which the pure state $|\psi(t)\rangle$ is integrated over a time much longer than Γ_{ad} and K-means clustering is applied to the cavity amplitude $\langle\psi(t)|\,a\,|\psi(t)\rangle$. We shall expand on these methods in chapter 3.

Chapter 3

Switching rates and occupation probabilities in the bistable regime

In this chapter we will describe how to calculate the rate of switching between metastable states in the bistable regime of the Duffing oscillator using Keldysh field theory. We then compare these rates with numerical results produced by studying the spectrum of the Liouvillian.

3.1 Keldysh approach

In a frame rotating with the drive the Duffing oscillator Hamiltonian is given by

$$H = \delta a^\dagger a + \chi a^\dagger a^\dagger a a + i\varepsilon(a^\dagger - a) \tag{3.1}$$

where δ is the detuning between the oscillator and the drive frequency, χ is the nonlinearity of the oscillator, ε is the drive amplitude and we have taken $\hbar = 1$. The rotating wave approximation has been applied in order to neglect counter rotating terms. If the oscillator is weakly coupled to a Markovian bath, then its density matrix will evolve according to the Lindblad master equation

$$\partial_t \rho = -i[H,\rho] + 2\kappa D[a]\rho \tag{3.2}$$

where $D[L]\rho = L\rho L^\dagger - \frac{1}{2}(L^\dagger L\rho + \rho L^\dagger L)$ and κ is the relaxation rate. If we map the dynamics of the master equation to that of Keldysh nonequilibrium functional

integral [75, 76, 77], we get the corresponding action in the forward/backward-time-field basis $S = \int L\, dt$ where

$$\begin{aligned} L = a_+^* i\partial_t a_+ - a_-^* i\partial_t a_- - \delta(a_+^* a_+ - a_-^* a_-) - \chi(a_+^{*2} a_+^2 - a_-^{*2} a_-^2) \\ - i\kappa\left(2a_+ a_-^* - a_+^* a_+ - a_-^* a_-\right) + i\varepsilon(a_+ + a_-^* - a_+^* - a_-). \end{aligned} \tag{3.3}$$

Here $\pm$ denotes the fields in the forward and backward time branches. It is convenient to introduce the classical and quantum field variables which are given by $a_c = (a_+ + a_-)/\sqrt{2},\ a_q = (a_+ - a_-)/\sqrt{2}$. In this basis the Lagrangian is given by

$$L = L_{\text{lin}} + L_{\text{nl}}, \tag{3.4}$$

$$L_{\text{lin}} = a_c^*(i\partial_t - \delta - i\kappa)a_q + a_q^*(i\partial_t - \delta + i\kappa)a_c + 2i\kappa a_q^* a_q + i\sqrt{2}\varepsilon(a_q - a_q^*) \tag{3.5}$$

$$L_{\text{nl}} = -\chi\left(a_c^* a_c + a_q^* a_q\right)\left(a_c^* a_q + a_c a_q^*\right) \tag{3.6}$$

where L_{lin} and L_{nl} denote the linear and nonlinear components of the Lagrangian respectively. From this Lagrangian we can obtain the saddle point equations of motion according to:

$$\frac{\partial L}{\partial a_q^*} = 0, \qquad \frac{\partial L}{\partial a_c^*} = 0. \tag{3.7}$$

The resulting equations of motion are given by

$$\partial_t a_c = \sqrt{2}\varepsilon - i\delta a_c - \kappa(a_c + 2a_q) - i\chi\left(a_c|a_c|^2 + 2a_c|a_q|^2 + a_c^* a_q^2\right), \tag{3.8}$$

$$\partial_t a_q = \kappa a_q - i\delta a_q - i\chi\left(a_q|a_q|^2 + 2|a_c|^2 a_q + a_c^2 a_q^*\right). \tag{3.9}$$

These equations describe the evolution of the system in a 4-dimensional space spanned by two complex fields. To obtain the classical equations of motion we can by setting $a_q = 0$ and simplifying the equation for $\partial_t a_c$ to give

$$\partial_t a_c = \sqrt{2}\varepsilon - i\delta a_c - \kappa a_c - i\chi a_c|a_c|^2. \tag{3.10}$$

This is equivalent to the mean-field equation of motion we have discussed previously in eq. 2.5. We have now constrained our system to the classical plane and in the bistable regime there will be three fixed points within this plane. Two of these points are stable and they correspond to the bright and dim states whereas a third unstable point lies on the separatrix which divides the plane into the two basins of attraction of the stables states.

Although the bright and dim states are stable within the classical plane, quantum fluctuations out of the plane can allow rare escape escape events. The trajectories of these escape events are described by the full equations of motion (3.8). In the following we find it convenient to decompose the variables into real and imaginary components according to:

$$a_c = \frac{x_c + ip_c}{\sqrt{2}}, \quad a_q = -\frac{x_q + ip_q}{\sqrt{2}}.$$

The dynamics can then be mapped to the following Hamiltonian[1]:

$$\begin{aligned} H = &\left(\delta + \frac{\chi}{2}\left(x_c^2 + p_c^2 - x_q^2 - p_q^2\right)\right)(p_c x_q - x_c p_q) - \kappa(x_c x_q + p_c p_q) \\ &+ \kappa(x_q^2 + p_q^2) + 2\varepsilon x_q. \end{aligned} \tag{3.11}$$

with the equations of motion given by:

$$\dot{\boldsymbol{z}}_c = \partial_{\boldsymbol{z}_q} H, \qquad \dot{\boldsymbol{z}}_q = -\partial_{\boldsymbol{z}_c} H \tag{3.12}$$

where $\boldsymbol{z}_c = (x_c, p_c)$ and $\boldsymbol{z}_q = (x_q, p_q)$. This process is explained in more detail in Appendix 3.A. These two quantities can be grouped together into $\boldsymbol{Z} = (\boldsymbol{z}_c, \boldsymbol{z}_q)$.

At first we are interested in the steady-state solution of the classical equations of motion, because this will indicate whether or not we are in the bistable regime. Let us denote a steady-state solution by the co-ordinates $(x_{c,\mathrm{ss}}, p_{c,\mathrm{ss}})$, in terms of which the cavity amplitude is given by $a_0 \equiv (x_{c,\mathrm{ss}} + ip_{c,\mathrm{ss}})/\sqrt{2}$. By rewriting our parameters in the form $\tilde{\delta} = \delta/\kappa$, $\tilde{\chi} = \chi/\kappa$ and $\tilde{\varepsilon}^2 = 2\tilde{\chi}\varepsilon^2/\kappa^2$ and absorbing the

[1] Derived by Changwoo Lee.

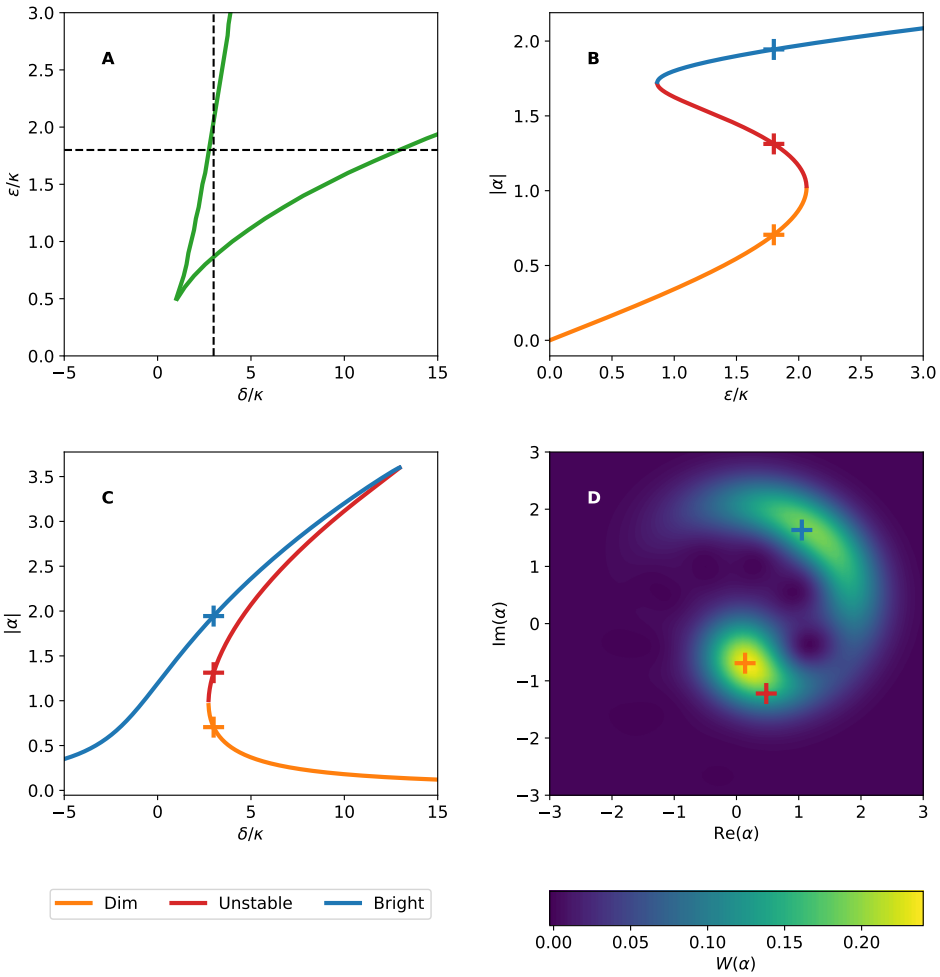

Figure 3.1.1: Fixed points of the classical equations of motion. Within the bistable regime the classical equations of motion have three fixed points, of which two are stable and one is unstable. In panel **A** we plot the boundaries of this regime as a function of the drive ε and detuning δ for $\chi/\kappa = -0.5$. We find that the bistable regime emerges above $\varepsilon/\kappa = 0.5$ and expands over a wider range of detunings as the drive is increased. In panels **B** and **C** we plot the amplitude of the fixed points as a function first of ε at $\delta/\kappa = 3$ and then as a function of δ at $\varepsilon/\kappa = 1.8$ i.e. along the dashed black lines indicated in panel **A**. We can now see the three fixed points which emerge in the bistable regime. The dim, bright and unstable states are indicated by the lower (orange), upper (blue) and middle (red) lines respectively. In panel **B** we see that the resonator responds linearly to low drives before making a sudden transition to a high amplitude state at higher drives. We see further evidence of nonlinear behaviour when we plot the response as a function of δ in panel **C**. Instead of displaying a Lorentzian response function typical of linear oscillators, we see a highly asymmetric peak which has shifted from the natural resonance frequency of the oscillator ($\delta = 0$). Finally, in panel **D** we plot the Wigner function obtained from the steady-state of the Lindblad master equation at $\delta/\kappa = 3$ and $\varepsilon/\kappa = 1.8$. There are two clear peaks, which correspond to the bright and dim states, and we compare them with the classical fixed points, marked by crosses. We see good agreement, indicating that the mean-field approximation is valid in this regime.

amplitude into $y = \tilde{\delta} + \tilde{\chi}|a_0|^2$, an algebraic equation for y with $\dot{x}_c = \dot{p}_c = 0$ can be obtained from eq. 3.10 in the form

$$y = (y - \tilde{\delta})(y^2 + 1) - \tilde{\varepsilon}^2. \tag{3.13}$$

This equation has only one solution if $|\tilde{\varepsilon}^2 + \tilde{\delta}(\tilde{\delta}^2 + 9)| > (\tilde{\delta}^2 - 3)^{3/2}$, two solutions if $|\tilde{\varepsilon}^2 + \tilde{\delta}(\tilde{\delta}^2 + 9)| = (\tilde{\delta}^2 - 3)^{3/2}$ and three otherwise. This last case is indicative of bistability and it consists of two stable fixed points and one unstable fixed point.

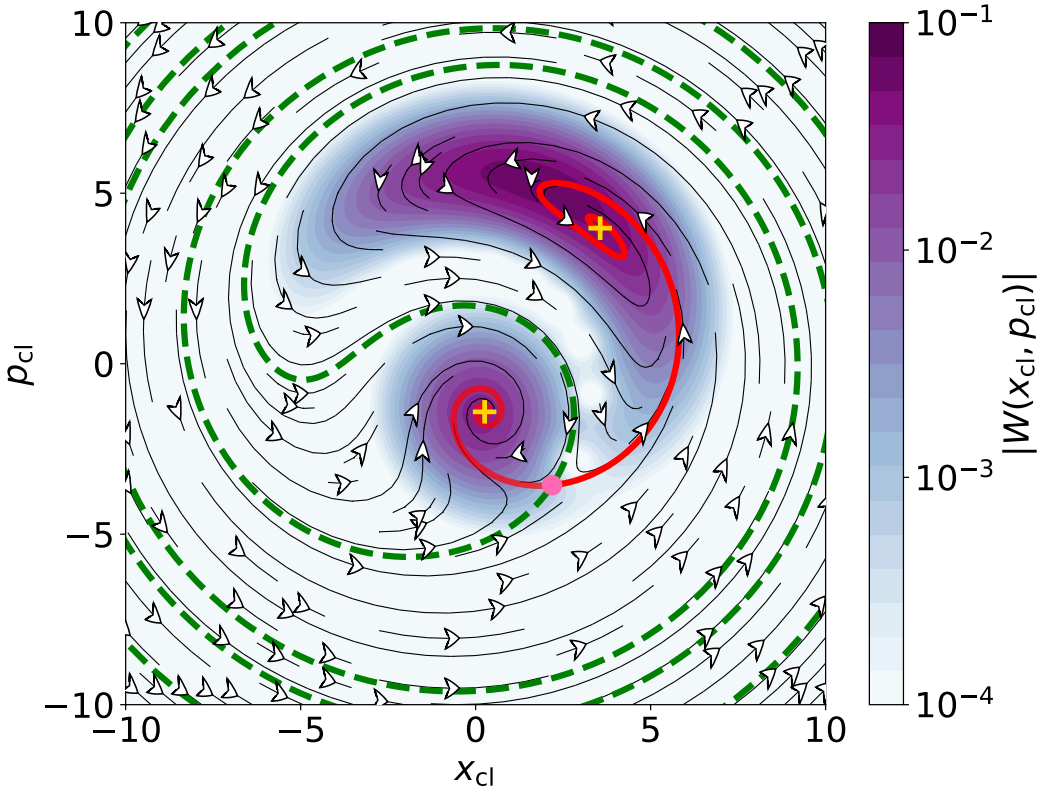

Figure 3.1.2: Wigner function and classical paths. Here we plot an example of the Wigner function in the bistable regime at $\delta/\kappa = 6.0$, $\varepsilon/\kappa = 4.0$ and $\chi/\kappa = -0.5$. The bright state can be seen in the upper right hand quadrant, whereas the dim state is located close to the origin. The classical fixed points corresponding to these states are represented by the yellow crosses and the solutions of the classical equations of motion are marked by black lines and white arrows. Depending on the initial conditions these flow lines converge on either the dim state or the bright state. The separatrix, marked by the green dashed line, forms the boundary between the basins of attraction of these states. Finally the unstable classical fixed point is marked by the pink dot. We have plotted the flow lines originating from the unstable point in red.

To illustrate this we have plotted these fixed points as a function of detuning

and drive amplitude for the case $\chi/\kappa = -0.5$ in Fig. 3.1.1. The green lines in panel A show the boundaries on the bistable regime. We see that at $\varepsilon/\kappa = 0.5$ the bistable appears and as the drive is increased it opens up over an ever wider range of detunings. In panel B we display the dependence of the amplitude of the fixed points on the drive at $\delta/\kappa = 3$ i.e. along the vertical dashed line in panel A. At low detunings there is a single fixed point displayed in orange, which corresponds to the dim state. Meanwhile at high detunings the single fixed point is displayed in blue and corresponds to the bright state. However over the range $0.86 < \varepsilon/\kappa < 2.06$ three fixed points coexist with each other. In this range the red line highlights the unstable fixed points. This is the bistable regime. Panel C shows these same three fixed points, but now as a function of the detuning at $\varepsilon/\kappa = 1.8$ i.e. along the horizontal dashed line in panel A.

Note that the response of the cavity displayed in panels B and C is highly nonlinear. Whereas we would expect the amplitude response of a linear oscillator to increase in direct proportion to the drive, here we see the S-curve which is typical of the bistable regime. Meanwhile the response as a function of detuning differs significantly from the a Lorentzian and is both asymmetric and shifted to higher detunings due to the nonlinearity χ. Finally, in panel B we compare the mean-field fixed points at $\varepsilon/\kappa = 1.8$ and $\delta/\kappa = 3$ with a Wigner function of the steady-state of the master equation (Eq. 3.2). The Wigner function clearly shows two peaks which correspond to the bright and dim states and whose amplitudes agree closely with the mean-field results.

A closer look at the classical dynamics of the bistable regime is on display in Fig. 3.1.2. The Wigner function of the steady-state at $(\delta/\kappa, \varepsilon/\kappa, \chi/\kappa) = (6.0, 4.0, -0.5)$ is plotted and the stable fixed points of the classical equations of motions are marked by yellow crosses. Black streamlines with white arrows are overlain on the Wigner function to show the classical evolution of the system. It can be seen that all of these streamlines eventually converge on one of the fixed points. The plane is divided into two basins of attraction by the separatrix marked by the green dashed line. Each basin corresponds to one of the fixed points. Fi-

nally the unstable fixed point is marked by the pink dot and the classical trajectories originating from the vicinty of this fixed point are marked in red.

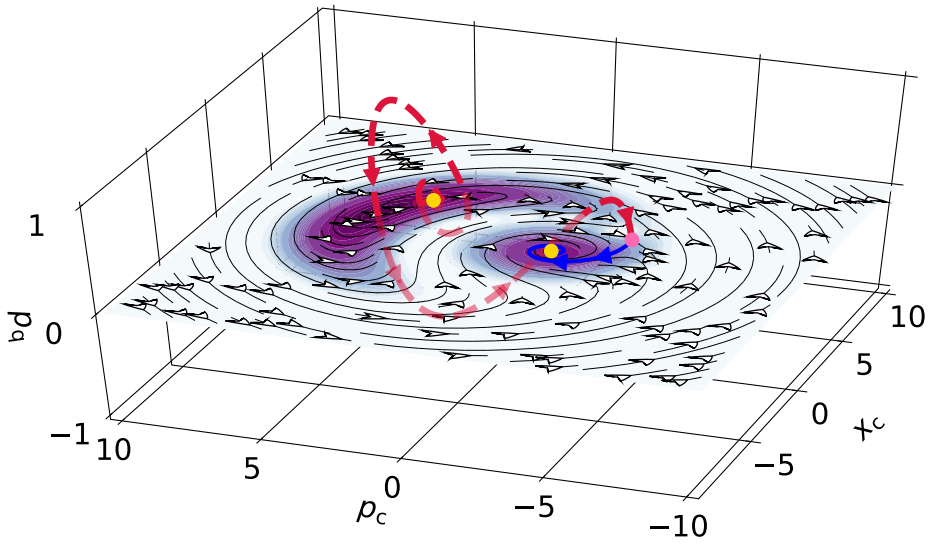

Figure 3.1.3: Switching trajectory going from the bright state to the dim state. The optimal switching trajectory going from the bright to the dim state is a solution to the 4-dimensional equations of motion in which the quantum co-ordinates x_c and p_c are non-zero, but here we only display the coordinates x_c, p_c and p_q. The Wigner function is plotted in the $p_q = 0$ plane and the stable classical fixed points are marked by yellow dots. The switching trajectory originates from the bright state and takes a complicated path outside the classical plane before reaching the unstable fixed point, marked by the pink dot. The system may then follow the classical path to the dim state. This example was produced at $(\delta/\kappa, \chi/\kappa, \varepsilon/\kappa) = (6, -0.5, 4)$.

Next we consider the full EOM, including non-zero values of x_q and p_q. These equations of motion have three fixed points within the classical plane, two of which are stable while the other is unstable. The dim and bright fixed points are denoted by $\boldsymbol{Z}_d$ and $\boldsymbol{Z}_b$ respectively and the unstable point is denoted by $\boldsymbol{Z}_u$. The two stable points each have their own basin of attraction and the unstable point lies on the boundary which separates these two basins. In order to switch from one stable point to another the system must leave the classical plane by utilizing the quantum dimensions x_q and p_q. The path of least action takes the system to the unstable point, from which it may move into the basin of attraction of the other stable point. An example of a switching path leading from the bright state to the dim state is displayed in Fig. 3.1.3.

In order to classify the fixed points it is necessary to linearise the equations of motion around them. At the stable points we find two eigenvalues given by $e_{j,-,\pm} = -\kappa \pm i\omega$ with eigenvectors $\boldsymbol{v}_{j,-,\pm}$ residing in the classical plane, where $j \in \{b,d\}$. This indicates that these points are stable within the plane. On the other hand, these points also have two eigenvectors $\boldsymbol{v}_{j,+,\pm}$ with nonzero quantum components and eigenvalues $e_{j,+,\pm} = \kappa \pm i\omega$, so they are not stable when we consider the full four-dimensional space.

As for $\boldsymbol{Z}_u$, the eigenvectors $\boldsymbol{v}_{u,-,1}$ and $\boldsymbol{v}_{u,+,2}$ corresponding to eigenvalues $e_{u,c,-} = -\kappa_1$ and $e_{u,+,2} = \kappa_2$ ($\kappa_1 > \kappa_2 > 0$) reside in the classical plane, which indicates that it is saddle point within the classical plane. Meanwhile, the eigenvectors $\boldsymbol{v}_{u,+,1}$ and $\boldsymbol{v}_{u,-,2}$ corresponding to eigenvalues $e_{u,+,1} = \kappa_1$ and $e_{u,-,2} = -\kappa_2$ have nonzero quantum components. The fact that the eigenvalues of fluctuation eigenvectors are nothing but negative of deterministic ones is characteristic of fluctuation-induced escape mechanism [78].

The probability of a successful escape event is proportional to $e^{S_{j\to u}}$ where $S_{j\to u}$ is the action calculated along the path from stable fixed point j to the unstable point. This quantity is given by:

$$S_{j\to u} = -\int_{\boldsymbol{Z}_j \to \boldsymbol{Z}_u} d\boldsymbol{z}_c \cdot \boldsymbol{z}_q, \tag{3.14}$$

This action can be computed from the numerical solution of the equations of motion. There are two methods of obtaining a solution depending on whether we treat path as an final value problem (FVP) or a boundary value problem (BVP), which we now compare.

Due to the stiffness of the equations of motion it, is numerically intractable to solve them in the vicinity of the stable fixed points. In the FVP method we instead initialize the system close to $\boldsymbol{Z}_u$ integrate backwards in time [79]. By the previous linearisation analysis around $\boldsymbol{Z}_u$, we know there is a negative eigenvalue $e_{u,-,2} = -\kappa_2$ and the corresponding eigenvector having nonzero quantum values. We use this eigenvector $\boldsymbol{v}_{u,-,2}$ to produce the initial conditions $\boldsymbol{Z}_u \pm \Delta\boldsymbol{v}_{u,-,2}$, in which we set Δ as small as our computing system allows, and integrate backwards

in time until we approach the stable points. The switching action is then calculated according to the formula above.

To check the validity of this method we can also use a BVP method. In this case the initial and final conditions are chosen to be $\boldsymbol{Z}_j + \Delta_{j,+,+}\boldsymbol{v}_{j,+,+} + \Delta_{j,+,-}\boldsymbol{v}_{j,+,-}$ and $\boldsymbol{Z}_u + \Delta_{u,-,1}\boldsymbol{v}_{u,-,1} + \Delta_{u,-,2}\boldsymbol{v}_{u,-,2}$. These conditions are set to ensure the system starts along a path leaving a stable state and ends along a path arriving at the unstable state. The Δ coefficients are used as fitting parameters when solving for the switching path using the scipy.integrate.solve_bvp function in SciPy [80].

We have numerically confirmed that two solutions evolve to the two stable points respectively and calculated the escape actions according to the integral above. The two methods are compared in Fig. 3.1.4 for a range of values of δ. The two methods align with each other well, indicating that despite the difficulty of dealing with these stiff equations of motion we have converged on the correct solution. A further example of the FVP method is shown in Fig. 3.1.5.

Both methods require of the order 1 minute to compute the action at a given set of parameters when the calculations are performed using an Intel Core i7-9700 Processor. However there is a marked difference between the numerical precision required by the methods. In the FVP formulation we found it necessary to specify the initial conditions with a precision greater than 1 part in 10^{20} in order to successfully converge to the stable point. This goes beyond the realm of double length floating point numbers and significantly complicates the procedure. FVP calculations were performed using Wolfram Mathematica[2]. This high sensitivity to initial state conditions may be an example of chaotic dynamics which is common in non-linear systems.

In the BVP approach the solver has information about both the initial state and the final state and the task is to find the path in between. This appears to be a more efficient approach in our system and only double length floating point precision is required. Therefore the approach is compatible with standard tools in Python such as SciPy.

[2]Mathematica notebooks for this task were prepared by Changwoo Lee.

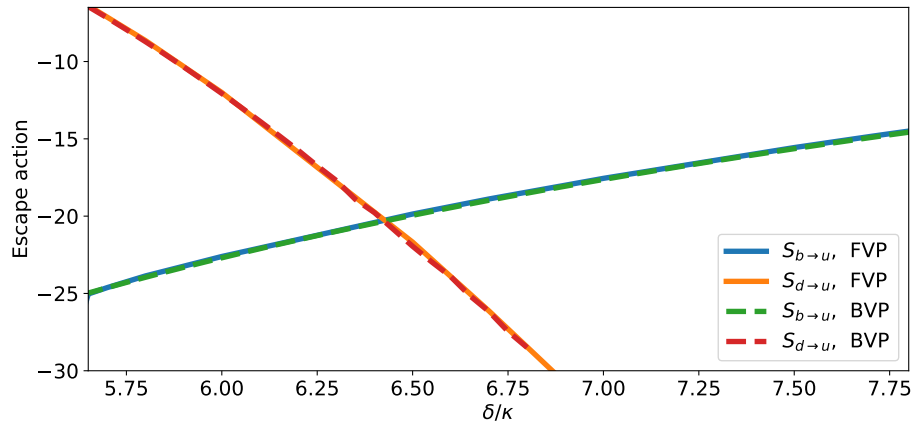

Figure 3.1.4: We calculate the actions of the switching trajectories from the stable points to the unstable point via both the boundary value method (BVP) and the end value method (FVP). Close agreement is found. The standard deviation of the difference between the methods is $\sigma = 0.1$.

The switching rate from $\boldsymbol{x}_j$ to the other stable point $\boldsymbol{x}_k$ reads $\gamma_{j\to k} = \omega_j e^{iS_j}$ where the prefactor ω_j is the attempt frequency [81, 82]. Assuming the dilute gas limit of instantons [81] and an effective two-state model [82, 83], the dynamics of probabilities of the system being at $\boldsymbol{x}_j$ is governed by the following master equation

$$\frac{d}{dt}\begin{bmatrix} p_{\mathrm{b}} \\ p_{\mathrm{d}} \end{bmatrix} = \begin{bmatrix} -\gamma_{\mathrm{b}\to\mathrm{d}} & \gamma_{\mathrm{d}\to\mathrm{b}} \\ \gamma_{\mathrm{b}\to\mathrm{d}} & -\gamma_{\mathrm{d}\to\mathrm{b}} \end{bmatrix}\begin{bmatrix} p_{\mathrm{b}} \\ p_{\mathrm{d}} \end{bmatrix}. \tag{3.15}$$

This master equation yields the stationary probabilities

$$p^s_{\mathrm{b(d)}} = \gamma_{\mathrm{d(b)}\to\mathrm{b(d)}}/\gamma_{\mathrm{total}}, \quad \gamma_{\mathrm{total}} \equiv \gamma_{\mathrm{b}\to\mathrm{d}} + \gamma_{\mathrm{d}\to\mathrm{b}}. \tag{3.16}$$

3.2 Liouvillian approach

In order to provide a crosscheck of the Keldysh approach we have developed an alternative method for calculating switching rates which relies on a the Lindblad master equation (Eq. 3.2). Since the master equation is linear, we can rewrite the evolution in terms of the Liouvillian superoperator $\mathscr{L}$ [48]:

$$\partial_t \rho = \mathscr{L}\rho. \tag{3.17}$$

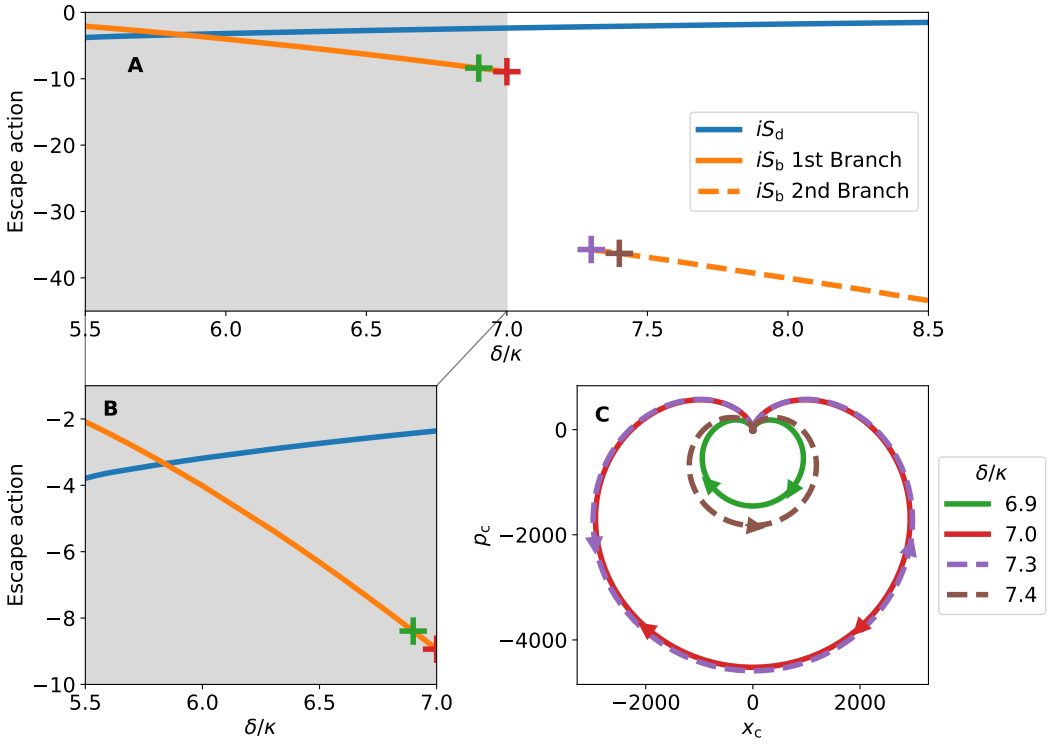

Figure 3.1.5: Action of the escape trajectories at $\varepsilon/\kappa = 4$ as a function of δ. At each value of δ we finding the switching trajectories and calculate their actions. These are plotted in panel **A**, which a zoom in panel **B**. The action of the trajectory escaping from the dim state iS_d is plotted in blue whereas the action of the trajectory escaping from the bright state iS_b is plotted in orange. As we increase δ the values of iS_b and iS_d cross each other, indicating a transition from a regime where the bright state is favoured to one where the dim state replaces it. Whereas the variation in iS_b is smooth and continuous, the variation in iS_d displays a gap at $7.0 < \delta/\kappa < 7.3$ before a sudden drastic fall. This is because in this range the switching path leaving the dim state becomes intractable. We plot four example switching paths in panel **C** at $\delta/\kappa = 6.9, 7.0, 7.3$ and 7.4. The direction of motion is indicated by the arrows marked on the paths. As we approach the missing region the switching path rapidly becomes larger before making sudden transition between clockwise and anticlockwise motion. No limit to the size of the switching path has been found, leading us to conjecture that the path diverges to infinity at some point in the missing range. This divides the value of iS_d into two disconnected branches, which are marked separately by solid and dashed lines.

We denote the matrix form of the Liouvillian by $\overline{\overline{\mathscr{L}}}$, which acts on a vectorized form for the densisty matrix $\overline{\rho}$. The Liouvillian matrix is given by

$$\overline{\overline{\mathscr{L}}} = -i\big((H\otimes\mathbb{1}) - (\mathbb{1}\otimes H^T)\big) + \sum_m \big(L_m\otimes L_m^* - L_m^\dagger L_m\otimes\mathbb{1} - \mathbb{1}\otimes L_m^T L_m^*\big). \quad (3.18)$$

Soon we shall see that a detailed investigation of the eigenvectors and eigenvalues of this Liouvillian matrix will allow us to extract both the occupation probabilities of the metastable states and their switching rates.

The eigenvalue equation takes the form $\overline{\overline{\mathscr{L}}}\overline{\rho}_m = -(\gamma_m + i\omega_m)\overline{\rho}_m$, where the real and imginary components of the complex eigenvalues are denoted by γ_m and ω_m respectively. The meaning of these components becomes clear when we write down the evolution of a state in terms of the eigenvectors as

$$\overline{\rho}(t) = \sum_n c_n e^{-(\gamma_m + i\omega_m)t}\overline{\rho}_m. \tag{3.19}$$

Now we see that γ_m represents the decay rate of the state $\overline{\rho}_m$ and ω_m represents its oscillation frequency. It is known that $\gamma_m \geq 0$ for all eigenvectors [48] and this ensures that $\overline{\rho}$ is well-behaved at long times. States for which $\gamma_m > 0$ will decay over time until the only remaning components of $\overline{\rho}(t)$ consists of those eigenvectors for which $\gamma_m = 0$. For our system we expect a single such eigenvector which forms the steady-state, denoted by $\overline{\rho}_{\text{ss}}$. In the bistable regime this state will consist of a mixture of the two metastable states, as we saw in Fig. 3.1.1. But we are also interested in the asymptotically decaying state, i.e. the eigenvector with the smallest finite value of γ_m, which will be denoted by ρ_{ad}. At long times the state of the system will consists of a mixture of the steady-state and this asymptotically decaying state, all other states having already decayed to negligible levels.

We now have two alternative descriptions of the transients response of the system: one from the Keldysh approach and one from the Liovuillian approach. The Keldysh approach shows us that the system approaches steady-state via switching events between the two metastable states which eventually cause the system to reach a dynamic equilibrium whereby the rates in each direction are balanced. This equilibration occurs at a rate $\gamma_{\text{total}} = \gamma_{\text{b}\to\text{d}} + \gamma_{\text{d}\to\text{b}}$. But now we see that this process is also described by the decay of an unknown asymptotically decaying state at rate γ_{ad}. These rates are in fact identical $\gamma_{\text{ad}} = \gamma_{\text{total}}$ and the asymptotically decaying state represents imbalance of the occupation probabilities of these states from the

eventual steady-state. It can be written as

$$\rho_{\mathrm{ad}} = N(\rho_{\mathrm{d}} - \rho_{\mathrm{b}}) \tag{3.20}$$

where we set the normalization N by $\mathrm{Tr}(\rho_{\mathrm{ad}}^{\dagger}\rho_{\mathrm{ad}}) = 1$. Given that the steady and asymptotically decaying states consist of independent mixtures of bright and dim states, we might consider combining them in such as way as to isolate their components. Having isolated the metastable states we may then calculate their occupation probabilities and hence the switching rates. The procedure for achieving this is illustrated in Fig. 3.2.1 and explained as follows. In panels A and B we have plotted the Wigner functions of the steady and asymptotically decaying states at $(\varepsilon/\kappa, \delta/\kappa, \chi/\kappa) = (1.8, 3.0, -0.5)$, within which the bright and dim states are clearly visible. We can write down a mixture of these states as

$$\tau(f) = \rho_{\mathrm{ss}} + f\rho_{\mathrm{ad}} \tag{3.21a}$$

$$= (p_{\mathrm{b}} - fN)\rho_{\mathrm{b}} + (p_{\mathrm{d}} + fN)\rho_{\mathrm{d}}. \tag{3.21b}$$

In order that ρ_{b} and ρ_{d} are both physically realistic states they should be positive semidefinite, i.e. they should have no negative eigenvalues. Let us define the function $\min(\tau)$ which returns the smallest eigenvalue of τ. Our condition can now be stated as $\min(\rho_{\mathrm{b}}), \min(\rho_{\mathrm{d}}) > 0$.

Next we assume that they are orthogonal, i.e. $\mathrm{Tr}(\rho_{\mathrm{b}}\rho_{\mathrm{d}}) = 0$, which is a good approximation provided the drive amplitude is sufficiently strong for the bistable states to be well separated. Given this assumption, the state $\tau(f)$ will be positive semidefinite if and only if the coefficients of the bistable states are both greater than or equal to zero. Therefore we can identify the values $f_{\mathrm{d}} = p_{\mathrm{b}}/N$ and $f_{\mathrm{b}} = -p_{\mathrm{d}}/N$ by plotting $\min[\tau(f)]$ as a function of f and locating where this function falls below zero. This function is plotted in panel C. Within the range $f_{\mathrm{b}} < f < f_{\mathrm{d}}$ we find $\min[\tau(f)] = 0$, which is to be expected since within a sufficiently large Hilbert space some states will have vanishingly small probabilities. These calculations were performed using a Hilbert space size of 20 states. The values f_{d} and f_{b} obtained

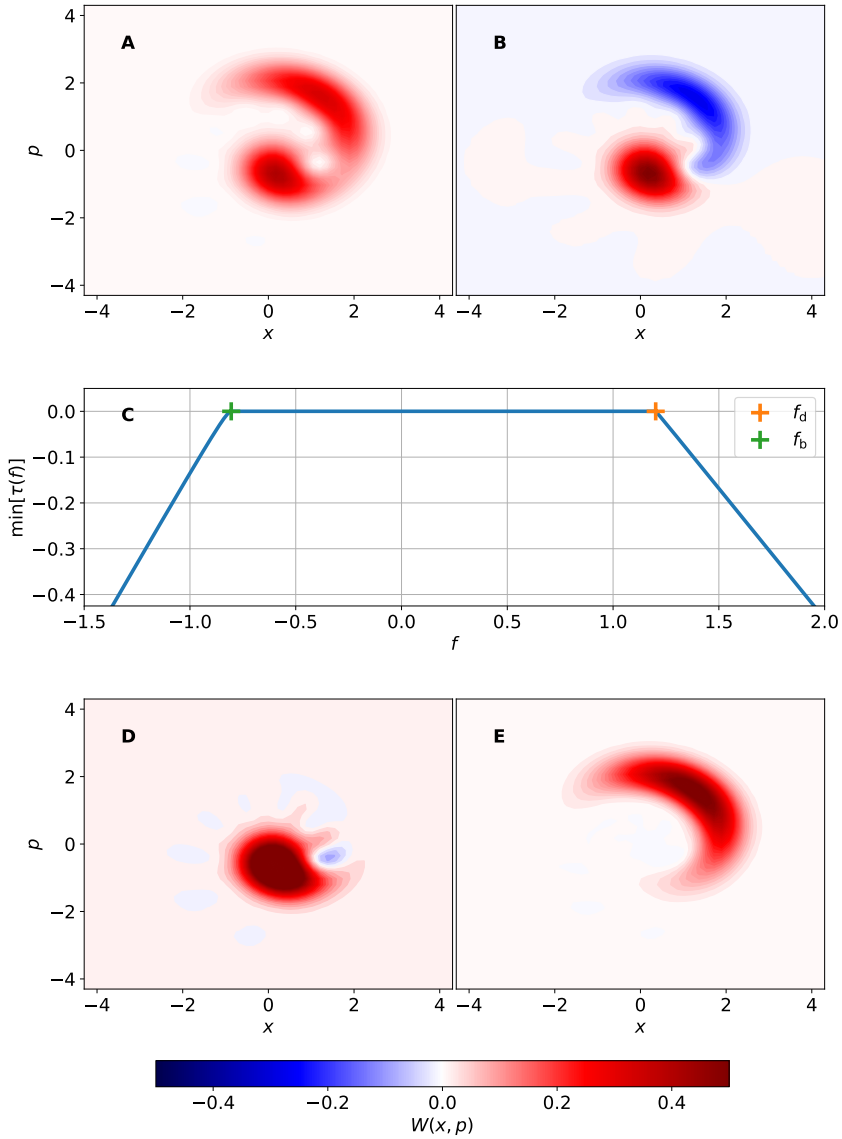

Figure 3.2.1: Extracting the metastable states from the steady and asymptotically decaying states. In panels **A** and **B** we plot the Wigner functions of the steady and asymptotically decaying states at $(\varepsilon/\kappa, \delta/\kappa) = (1.8, 3.0)$. We can see that the dim state makes a negative contribution to the asymptotically decaying state. This will allow us to form mixtures of steady and asymptotically decaying states which eliminate either the bright state or the dim state. In panel **C** we plot the minimum eigenvalue of $\tau(f) = \rho_{ss} + f\rho_{ad}$ as a function of f. This eigenvalue falls below zero when either the coefficient of either the bright state of the dim state in τ falls below zero. By identifying the values of f where this occurs we extract the dim and bright states. In panels **D** and **E** we plot $\tau(f_d)$ and $\tau(f_b)$ respectively, which are proportional to the dim and bright states.

from panel C are then used to produce the dim and bright states displayed in panels

D and E. Finally the occupation probabilities are given by

$$p_{\mathrm{b}} = \frac{f_{\mathrm{d}}}{f_{\mathrm{d}} - f_{\mathrm{b}}} \tag{3.22}$$

$$p_{\mathrm{d}} = \frac{f_{\mathrm{b}}}{f_{\mathrm{b}} - f_{\mathrm{d}}}. \tag{3.23}$$

3.3 Quantum jump approach

As a final crosscheck, it is also possible to obtain the occupation probabilities from quantum trajectory simulations. For example, we could consider a scenario in which the environment of our oscillator is continuously monitored for any leakage of photons. In this scenario it is known [84] that the wavefunction of the oscillator conditioned on these measurements can be broken up into two parts: periods of deterministic evolution according to a non-Hermitian effective Hamiltonian separated by occasional quantum jumps occurring when a photon escapes into the environment and is detected. The effective Hamiltonian is given by:

$$H_{\mathrm{eff}} = H - i\kappa a^{\dagger} a. \tag{3.24}$$

During a timestep Δt the non-Hermitian component causes the norm of the wavefunction to decline by:

$$\Delta p = 2\Delta t\, \kappa \langle \psi(t) | a^{\dagger} a | \psi(t) \rangle \tag{3.25}$$

which corresponds to the probability of a photon escape. If such an event occurs the wavefunction immediately jumps to a new normalized state given by:

$$|\psi(t+\Delta t)\rangle = \frac{a|\psi(t)\rangle}{\sqrt{\langle \psi(t)| a^{\dagger} a |\psi(t)\rangle}}. \tag{3.26}$$

In this manner we can evolve the wavefunction in time and build an ensemble of trajectories which describe the typical behaviour of the oscillator during an experiment. This task is performed using the solvers provided in the QuTiP packages [74].

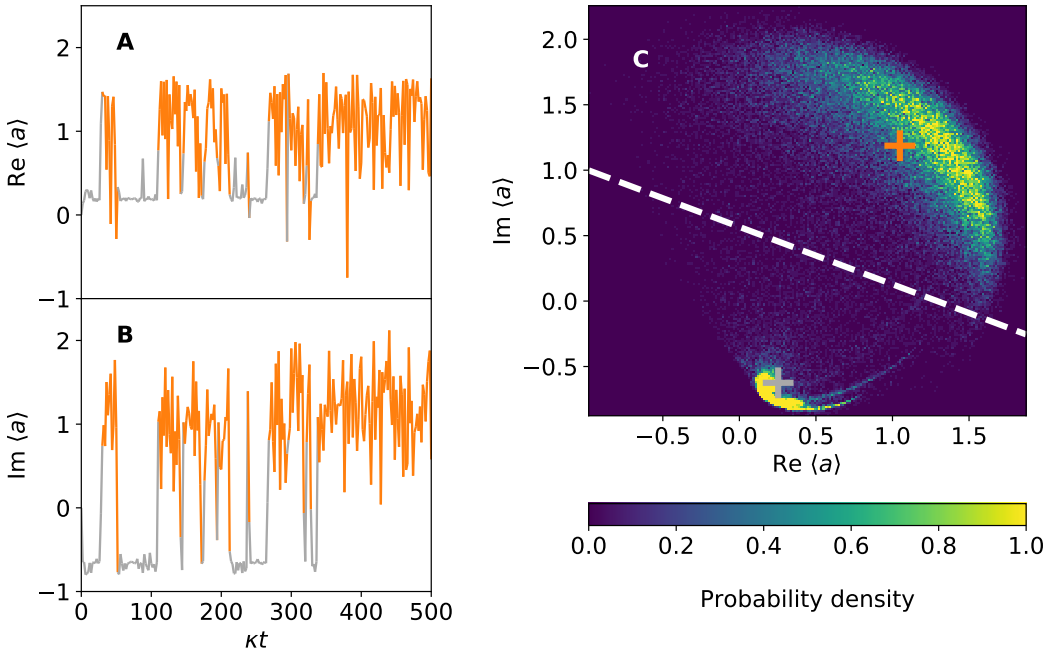

Figure 3.3.1: Using quantum trajectories to extract probabilities. As a crosscheck we can produce a quantum trajectory using an appropriate stochastic Schrödinger equation and identify the fraction of time the system spends in each state. Here we display an example trajectory produced at $(\varepsilon/\kappa, \delta/\kappa, \chi/\kappa) = (1.8, 3.0, -0.5)$. The real component of the cavity amplitude is plotted in panel **A** while the imaginary component is plotted in panel **B**. Within the trajectory we can see two metastable states, whose lifetimes are much longer than the natural lifetime of the oscillator. The dim state is marked in grey and the bright state is marked in orange. In panel **C** we use this trajectory to produce a histogram of the oscillator amplitude, within which the clusters corresponding to the bright and dim states are clearly visible. In order to identify the occupation probability of these two states we apply k-means clustering. This technique produces the linear classification boundary marked by the white dashed line, which forms the locus of points equidistant from the cluster centers marked in grey and orange. For this particular case we find $p_{\mathrm{b}} = 0.610$ and $p_{\mathrm{b}} = 0.390$.

An example is displayed in panels A and B of Fig. 3.3.1, which display the real and imaginary components of $\langle\psi(t)|\,a\,|\psi(t)\rangle\,/\,\langle\psi(t)|\,\psi(t)\rangle$ during a single quantum trajectory produced at $(\varepsilon/\kappa, \delta/\kappa, \chi/\kappa) = (1.8, 3.0, -0.5)$. We see clear evidence of occasional sudden switching between metastable states whose lifetimes are much greater than the typical lifetime of photons in the oscillator. Using k-means clustering [85], a standard technique for linear classification, we have classified the state of the oscillator at every sampled point in time. In panel C we display a histogram of the oscillator amplitude throughout evolution and we highlight the two cluster centers along with the boundary which separates them. By sampling the state of

the oscillator over a sufficiently long period of time we can find an estimate of the occupation probabilities of the two metastable states and compare them with the results of our previously described Liouvillian based method.

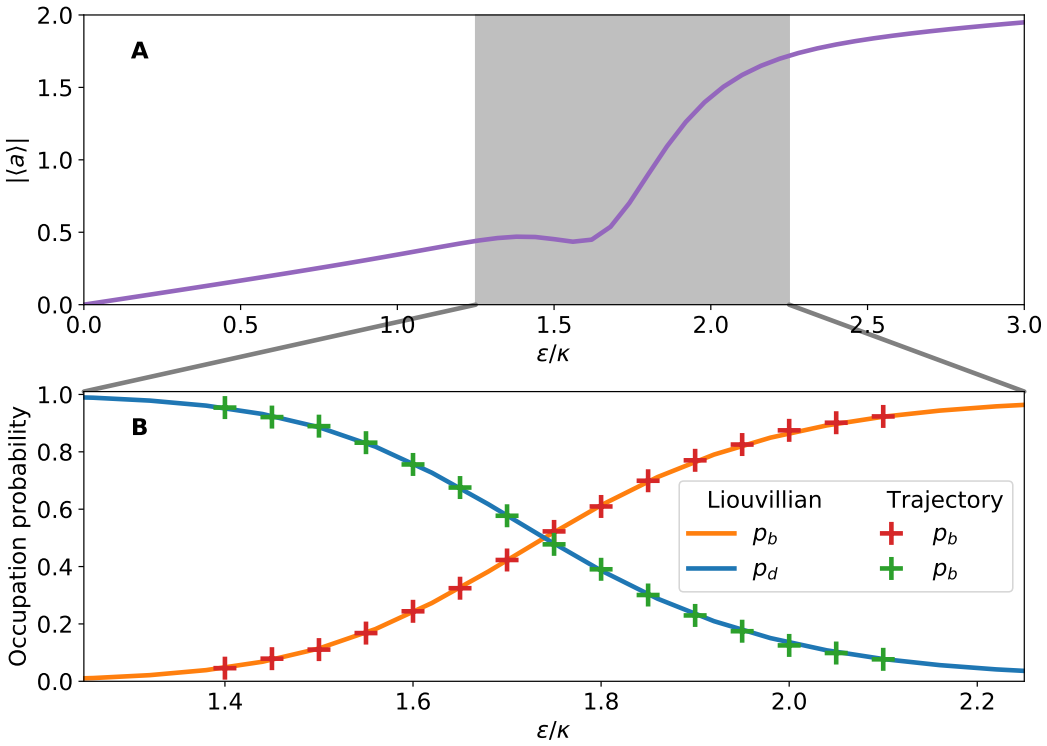

Figure 3.3.2: Occupation probabilities of the bright and dim states. In panel **A** we display the oscillator amplitude at $(\delta/\kappa, \chi/\kappa) = (3, -0.5)$ as a function of the drive ε. Over the range $1.25 < \varepsilon/\kappa < 2.25$ there is a sharp sudden increase in the oscillator amplitude. We zoom in on this range in panel **B**, where we examine the occupation probabilities of the bright and dim states according to our methods based on the Liouvillian and quantum trajectories. We see that the transition to a high amplitude state corresponds to a shift in occupation probability from the dim state to the bright state. We also see close agreement between our two methods, which gives us confidence that they are working effectively.

A comparison of occupation probabilities calculated using the trajectory and Liouvillian methods is presented in in Fig. 3.3.2. In panel A we first set the context by plotting the oscillator amplitude as a function of the drive ε at $(\delta/\kappa, \chi/\kappa) = (3.0, -0.5)$. This displays the expected linear response before a sudden transition to a high amplitude state. We focus on the intermediate region $1.15 < \varepsilon/\kappa < 2.25$ where the transition occurs. In panel B the occupation probabilities calculated using the Liouvillian method are marked by solid lines. These show a clear crossover from the dim state to the bright state as the transition occurs. The markers display the

occupation probabilities obtained from k-means clustering on quantum trajectories evolved over a time period of $200,000/\kappa$.

Close agreement between our methods observed. The root mean square difference between the two methods is only 0.004, which gives us confidence in their accuracy. However the Liouvillian method is much faster and can produce results over a wider range of drive parameters. Each trajectory took approximately 40 minutes to produce on the Intel Core i7-9700 Processor mentioned previously whereas the Liouvillian method produced matching results over 10 seconds. One reason for this disparity is that the trajectory method requires us to evolve the system for a long period of time in order to produce enough switching events between bistable states that the occupation probabilities converge. Since switching events are inherently rare, the required evolution time is much greater than the cavity lifetime $1/\kappa$. Switching events are most common when the two metastable states have equal occupation probabilities. Away from this point switching events can become extremely rare, which increases the length of the required evolution time.

3.4 Switching rates

Now that we have are confident in our calculations of the occupation probabilities we can use them to calculate the switching rates. After that we will compare these results with the switching rates calculated using the Keldysh method. First we rearrange Eq. 3.16 to give:

$$\gamma_{\mathrm{d(b)}\to\mathrm{b(d)}} = p_{\mathrm{b(d)}}\gamma_{\mathrm{ad}}. \tag{3.27}$$

Using this method we calculate the switching rates corresponding to the probabilities plotted in Fig. 3.3.2B. These are displayed in Fig. 3.4.1B. At the edges of the bistable regime γ_{ad} is dominated by the larger switching rate. In the middle of the bistable regime, where they are balanced, both rates contribute and γ_{ad} is minimized.

Finally we compare the Liouvillian and Keldysh methods in Fig. 3.4.2. In panel A we plot the steady-state oscillator amplitude as a function of δ and ε at $\chi/\kappa = -0.5$. This helps to give some context to the parameter ranges over which

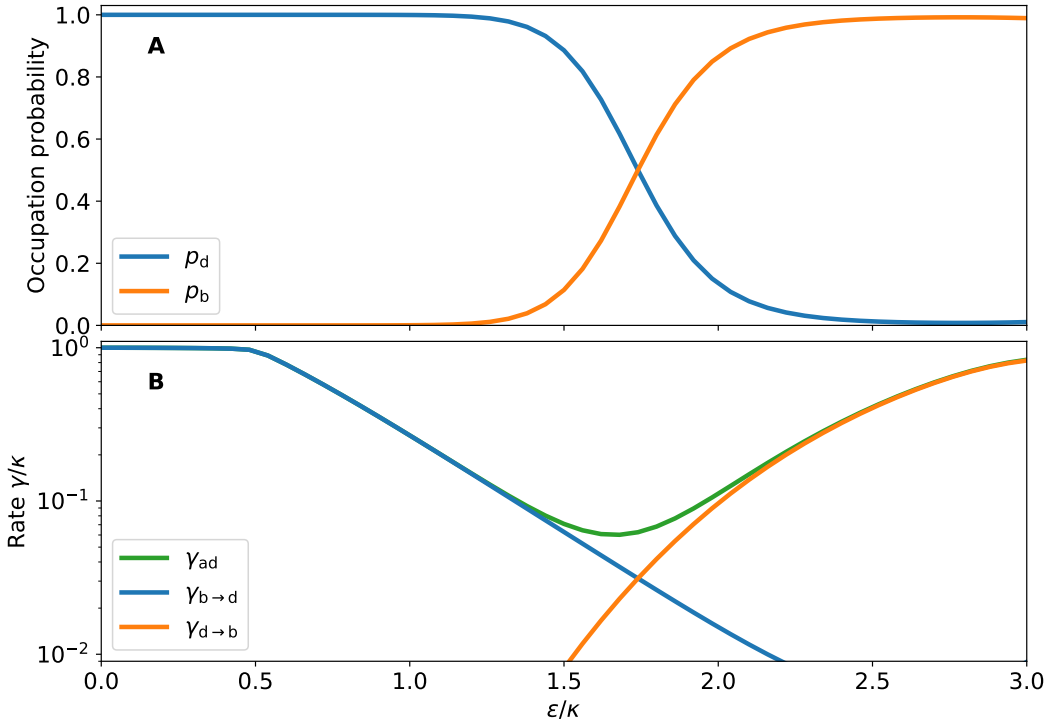

Figure 3.4.1: Calculating the switching rates from the occupation probabilities. In panel **A** we plot the occupation probabilities as a function of ε for $(\delta/\kappa, \chi/\kappa) = (3, -0.5)$ while in panel B we plot the asymptotic decay rate γ_{ad} in green. At low drives the system occupies the dim state and the asymptotic decay rate is equal to the oscillator decay rate κ. However, at sufficiently large drives the system switches from the dim state to the bright state. This transition occurs simultaneously with a dramatic reduction in the asymptotic decay rate, which falls by an order of magnitude. This effect is known as critical slowing down and it is characteristic of phase transitions. Using $\gamma_{d(b)\to b(d)} = p_{d(b)}\gamma_{ad}$ we are able to produce switching rates displayed in panel **B**.

we will compare the methods in panels B and C. In panel A the mean-field boundaries of the bistable regime are marked in red. Within this regime we see expected sudden transition between low and high amplitude states of the oscillator. The black lines highlight the parameter ranges over which panels B and C were produced. Using the attempt frequencies ω_b and ω_d as fitting parameters we are able to obtain excellent agreement between the switching rates produced by the Keldysh and Liouvillian methods over several orders of magnitude. This indicates that variations in the switching action are dominant in determining the dependence of the switching rates on the system parameters. Since the attempt frequencies are used as fitting parameters we are unable to fully quantify the accuracy of the Keldysh approach. Future work should examine how these attempt frequencies can be calculated in

order to complete this work.

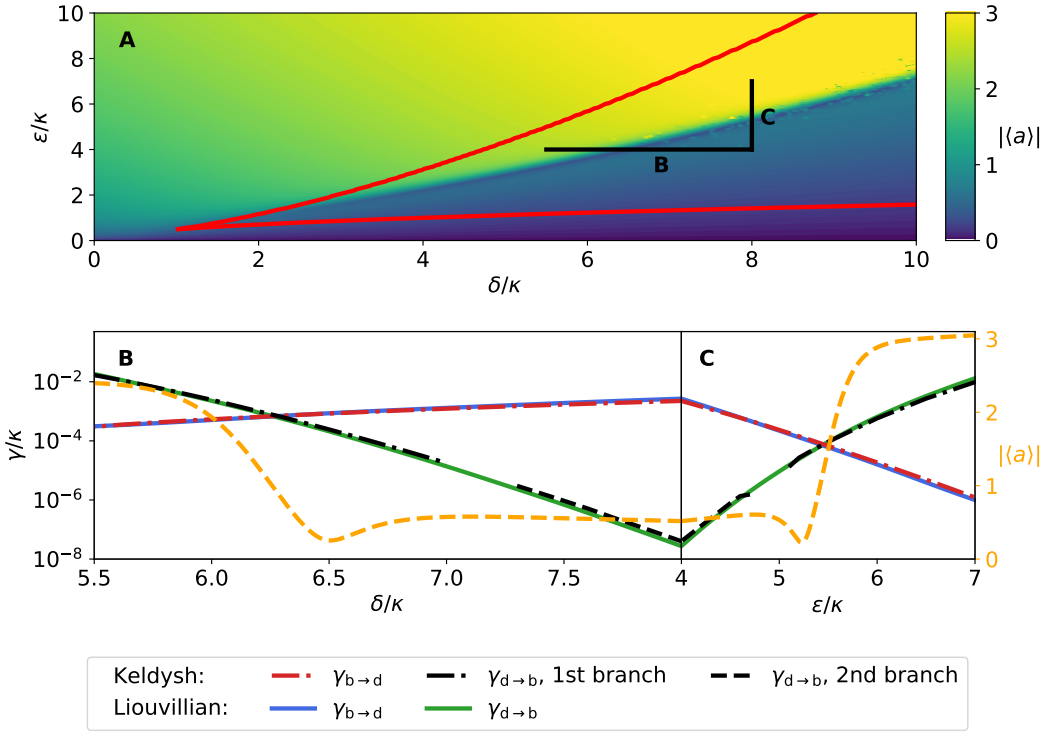

Figure 3.4.2: Comparing Keldysh and Liouvillian switching rates. Here we plot and compare the switching rates produced using the Keldysh and Liouvillian methods at $\chi/\kappa = -0.5$ and we place them in the context of the oscillator response. In panel **A** we plot the oscillator amplitude as a function of δ and ε. The boundaries of the bistable regime are calculated using the classical equations of motion and are marked in red. Within this bistable regime we can see the sudden transition from low to high amplitude states which occurs as the drive is increased. In panels **B** and **C** we will plot the switching rates and oscillator amplitude along the black lines marked in panel **A**. Panel **B** was produced at $\varepsilon/\kappa = 4$ while panel **C** was produced at $\delta/\kappa = 8$. If the attempt rates vary sufficiently slowly with δ and ε then we can assume they are constant and use them as fitting parameters. In this case we have used $\omega_{\mathrm{b}\to\mathrm{d}}/\kappa = 1.3\times10^{-2}$, $\omega_{\mathrm{d}\to\mathrm{b,1st\ branch}}/\kappa = 1.4\times10^{-1}$ and $\omega_{\mathrm{d}\to\mathrm{b,2nd\ branch}}/\kappa = 9.9\times10^{9}$. We justify using two separate attempt for the dim to bright switching due to the discontinuity in the switching path. Using these fitting parameters we see excellent agreement between the Keldysh and Liouvillian switching rates over several orders of magnitude. This indicates that our assumption that the attempt rates vary slowly with the drive parameters was remarkably accurate and the dominant variations in the switching rates are well described by the action of the optimal switching path. Finally, we overlay the cavity amplitude on these switching rate plots to show that the crossing of the rates coincides with transition between high and low amplitude states of the oscillator.

Contributions

This project was conceived by Eran Ginossar and Marzena Szymanska. Changwoo Lee placed the equations of motion in Hamiltonian form and found a way to calculate switching paths by initializing the system close to the unstable point and integrating backwards in time. Changwoo Lee also prepared Mathematica notebooks to implement this method, which Paul Brookes used in order to compare the various methods studied in this chapter. Paul Brookes found an alternative method of finding switching paths by using boundary value methods and contributed the method of finding metastable state occupation probabilities by studying the eigenvectors of the Liouvillian matrix. The comparisons between these methods and with the quantum trajectory approach were performed by Paul Brookes.

Appendix

3.A Deriving equations of motion in Hamiltonian form

In order to place the equations of motion in Hamiltonian form we first take the Lagrangian in eq. 3.4 and then decompose the field variables into real and imaginary components according to:

$$a_c = (x_c + ip_c)/\sqrt{2}, \quad a_q = (\tilde{x}_q + i\tilde{p}_q)/\sqrt{2}. \tag{3.28}$$

In these terms the Lagrangian becomes:

$$\begin{aligned} L = \dot{x}_c\tilde{p}_q - \dot{p}_c\tilde{x}_q - \left[\delta + \frac{\chi}{2}\left(x_x^2 + p_c^2 + \tilde{x}_q^2 + \tilde{p}_q^2\right)\right](x_c\tilde{x}_q + p_c\tilde{p}_q) \\ + \kappa(x_1\tilde{p}_q - p_c\tilde{x}_q) + i\kappa(\tilde{x}_q^2 + \tilde{p}_q^2) + 2\varepsilon\tilde{p}_q \end{aligned} \tag{3.29}$$

up to total derivatives. Allowing the variables to run on imaginary axes (near $\tilde{x}_q \approx 0,\ \tilde{p}_q \approx 0$), let:

$$\tilde{x}_q \to -ip_q,\ \tilde{p}_q \to ix_q \quad (\textit{instanton} \text{ transformation}), \tag{3.30}$$

then the above expression changes to a Hamiltonian structure:

$$iL = -\left[\dot{x}_c p_c + \dot{p}_c p_q - H\left(x_c, p_c, x_q, p_q\right)\right] \tag{3.31}$$

with an auxiliary Hamiltonian given by eq. (3.11) which produces the equations of motion in eq. (3.12). The action, consequently, becomes:

$$S = i\int L\,dt \tag{3.32}$$

$$= -\int d\boldsymbol{z}_c \cdot \boldsymbol{z}_q. \tag{3.33}$$

Chapter 4

Driving-induced resonance narrowing in a strongly coupled cavity-qubit system

4.1 Introduction

The spectral response of a variety of both classical and quantum systems near an isolated resonance is often well-described by the Breit-Wigner model [86]. In this description the lifetime of an isolated resonance can be determined from its linewidth. A variety of intriguing effects may occur in regions where resonances overlap [87]. For example, both linewidth narrowing and broadening have been observed with systems having overlapping resonances [88]. These effects are attributed to interference between different processes contributing to damping [89, 90]. Destructive interference gives rise to linewidth narrowing, whereas the opposite effect of broadening occurs due to constructive interference.

These effects have been demonstrated in a wide variety of both classical and quantum systems. In the classical domain narrowing has been observed with resonators having two overlapping resonances for which the frequency separation is smaller than the resonances' bandwidth [92, 93, 94]. Closely related processes occur in the quantum domain with systems having overlapping resonances. In some cases this overlap is obtained by static tuning of the system under study. One well-

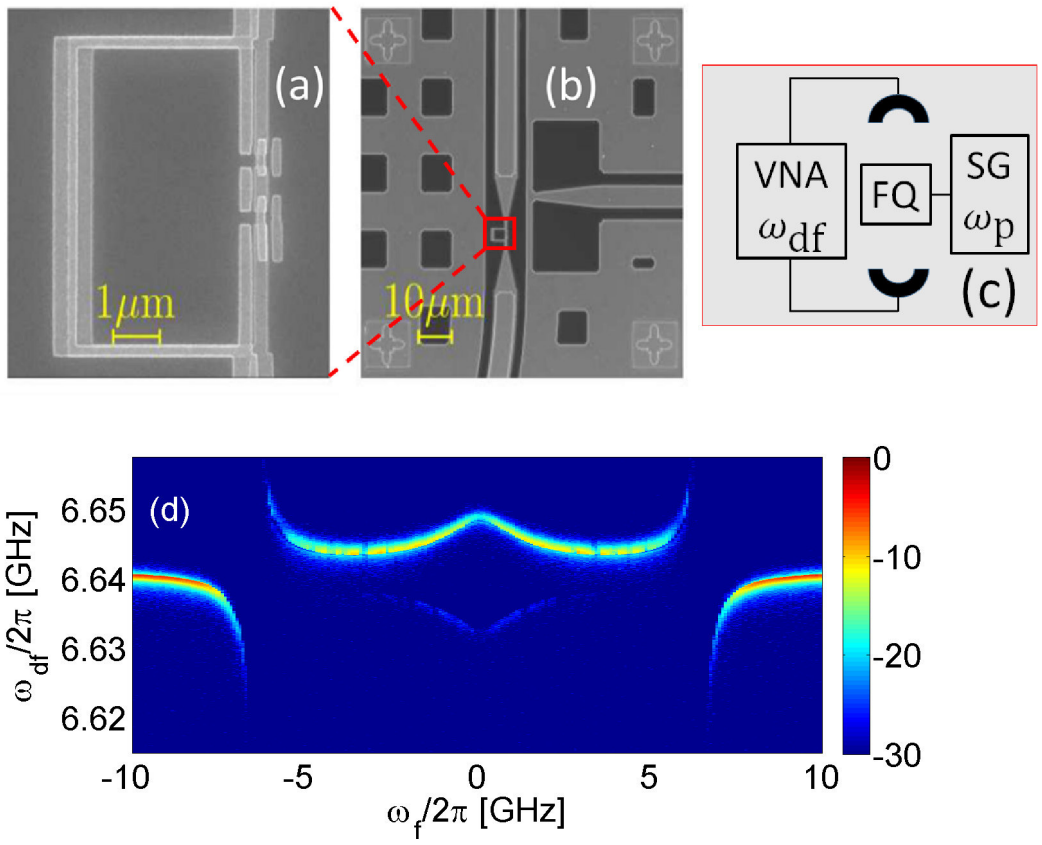

Figure 4.1.1: The device. (a) Electron micrograph of the flux qubit. (b) Zoom out electron micrograph showing the qubit embedded in the CPW resonator and its local flux control line. (c) Sketch of the experimental setup. The cavity transmission is measured using a vector network analyzer (VNA). Monochromatic flux qubit (FQ) driving is applied using a signal generator (SG). (d) The measured cavity transmission (in dB units) 60 vs. $\omega_f/2\pi$ (magnetic field detuning from the symmetry point) and $\omega_{df}/2\pi$ (cavity driving frequency). The power injected into the cavity is -112 dBm. For the device under study $\omega_c/2\pi = 6.6408\,\text{GHz}$, $\omega_\Delta/2\pi = 1.12\,\text{GHz}$, $g/2\pi = 0.274\,\text{GHz}$ and $\gamma_c/\omega_c = 1.1\times10^{-5}$. The relaxation time $T_1 = 1.2\,\mu\text{s}\,(1+0.45\,\text{ns}\times|\omega_f|)$ is obtained from energy relaxation measurements, and the rate $T_2^{-1} = 4.5\,\text{MHz}\,(1+44\,|\omega_f|/\omega_a)$ is obtained from Ramsey rate measurements [91]. The empirical expressions for both T_1 and T_2 are obtained using approximate interpolation.

known example is the Purcell effect [95], which is observed when atoms interact with light confined inside a cavity. In such cavity quantum electrodynamics (CQED) systems, both linewidth narrowing and broadening occur when the atomic and cavity mode resonances overlap. Other examples of static tuning giving rise to linewidth narrowing and broadening due to overlapping resonances have been reported in [96, 97].

Closely related processes occur in atomic systems exhibiting electromagnetically induced transparency (EIT) [98, 99]. However, tuning into the region of EIT is commonly based on external driving (rather than static tuning), which can be used for manipulating the spectrum of the dressed states. Both linewidth narrowing and broadening have been observed in such systems in the region where the dressed spectrum contains overlapping resonances. Commonly, a broadened resonance is referred to as a bright state, whereas the term dark state refers to a narrowed resonance. The slow propagation speed associated with dark states [100] can be exploited for long term storage of quantum information [101].

In this chapter we analyse recently collected data [102] displaying linewidth narrowing in a superconducting circuit composed of a microwave resonator couple to a Josephson flux qubit [103, 104] and we carry out a numerical study of the dynamics governing this phenomenon. The qubit under study, which is strongly coupled [105, 106, 107, 108] to a coplanar waveguide (CPW) microwave resonator [106, 109, 110, 111, 112, 113, 114, 115], is shown in Fig. 4.1.1(a) and (b). The strong coupling gives rise to a dispersive splitting of the cavity mode resonance and the experimenters found that this frequency splitting could be controlled by applying a monochromatic driving to the flux qubit [see Fig. 4.1.1(b)]. The effect of linewidth narrowing, which is discussed below in section 4.4, is observed when the frequency and power of qubit driving are tuned into the region where the frequency splitting vanishes. In this region the measured linewidth becomes significantly smaller than the linewidth of the decoupled cavity resonance by a factor of up to 20.

While the linewidth narrowing effect is induced by qubit driving, a variety of other nonlinear effects can be observed with strong cavity mode driving [116, 117, 118, 119, 120, 121, 71, 122, 123, 124, 125, 126, 127, 128, 129, 130, 131, 132]. In section 4.5 we focus on the lineshape of the cavity transmission in the nonlinear region. The experimental results are compared with predictions of a semiclassical theory. We find that good agreement can be obtained with theoretical predictions derived by numerical integration of the master equation for the coupled system.

4.2 Experimental setup

The device under investigation [see Fig. 4.1.1(a) and (b)] contains a CPW cavity resonator weakly coupled to two ports which are used for performing microwave transmission measurements [see Fig. 4.1.1(c)]. A persistent current flux qubit [103], consisting of a superconducting loop interrupted by four Josephson junctions, is inductively coupled to the fundamental half-wavelength mode of the CPW resonator. A CPW line terminated by a low inductance shunt is used for qubit driving [see Fig. 4.1.1(b) and (c)]. The device was fabricated on a high resistivity silicon substrate in a two-step process. In the first step, the resonator and the control lines were defined using optical lithography, evaporation of a 190 nm thick aluminum layer and liftoff. In the second step, a bilayer resist was patterned by electron-beam lithography. Subsequently, shadow evaporation of two aluminum layers, 40 nm and 65 nm thick respectively, followed by liftoff defined the qubit junctions.

The chip was enclosed inside a copper package, which was cooled using a dilution refrigerator to a temperature of $T = 23$ mK. Both passive and active shielding methods were employed to suppress magnetic field noise. While passive shielding was performed using a three-layer high permeability metal, an active magnetic field compensation system placed outside the cryostat was used to actively reduce low-frequency magnetic field noise. A set of superconducting coils was used to apply DC magnetic flux. Qubit state control, which was employed in order to measure the qubit longitudinal T_1 and transverse T_2 relaxation times, was performed using shaped microwave pulses. Attenuators and filters were installed at different cooling stages along the transmission lines for qubit control and readout. A detailed description of sample fabrication and experimental setup can be found in [111, 110].

4.3 The dispersive region

The Hamiltonan describing this system can be written as [133]

$$H = \hbar\omega_c a^\dagger a - \hbar g(a + a^\dagger)\sigma_0^z + \frac{1}{2}\hbar\omega_f\sigma_0^z + \frac{1}{2}\hbar\omega_\Delta\sigma_0^x \tag{4.1}$$

where a is a cavity annihilation operator and σ_0^x and σ_0^z are Pauli operators acting on the Hilbert space of the qubit. These operators can be written in the form $\sigma_0^x = |\circlearrowleft\rangle\langle\circlearrowleft| + |\circlearrowright\rangle\langle\circlearrowright|$ and $\sigma_0^z = |\circlearrowleft\rangle\langle\circlearrowleft| - |\circlearrowright\rangle\langle\circlearrowright|$ where $|\circlearrowright\rangle$ and $|\circlearrowleft\rangle$ correspond to a clockwise or anticlockwise circulating current of I_p.

The above Hamiltonian describes an inductive coupling of strength g between the flux qubit and the transmission line resonator, which has a resonance frequency of ω_c. Meanwhile the transition frequency of the qubit is given by $\omega_a = \sqrt{\omega_f^2 + \omega_\Delta^2}$. In the presence of an externally applied magnetic flux Φ_e, this frequency can be tuned by controlling $\omega_f = (2I_{cc}\Phi_0/\hbar)(\Phi_e/\Phi_0 - 1/2)$ where $\Phi_0 = h/2e$ is the flux quantum.

At this point it is convenient to change our basis to the energy eigenstates $|\pm\rangle$ of the qubit, which are given by:

$$\begin{pmatrix} |+\rangle \\ |-\rangle \end{pmatrix} = \begin{pmatrix} \cos(\theta/2) & \sin(\theta/2) \\ -\sin(\theta/2) & \cos(\theta/2) \end{pmatrix} \begin{pmatrix} |\circlearrowleft\rangle \\ |\circlearrowright\rangle \end{pmatrix} \tag{4.2}$$

where $\tan(\theta) = \omega_\Delta/\omega_f$. We use these states to define a new set of Pauli operators: $\sigma^z = |+\rangle\langle+| - |-\rangle\langle-|$, $\sigma^+ = |+\rangle\langle-|$ and $\sigma^- = |-\rangle\langle+|$, in terms of which the Hamiltonian is given by:

$$H = \hbar\omega_c a^\dagger a + \frac{1}{2}\hbar\omega_a\sigma^z - \hbar g(a + a^\dagger)\Big(\cos(\theta)\sigma^z - \sin(\theta)(\sigma^+ + \sigma^-)\Big) \tag{4.3}$$

$$\approx \hbar\omega_c a^\dagger a + \frac{1}{2}\omega_a\sigma^z + g\sin(\theta)(a\sigma^+ + a^\dagger\sigma^-) \tag{4.4}$$

where the last line is obtained by applying the rotating wave approximation. This leaves us with a Jaynes-Cummings Hamiltonian, which describes the exchange of quanta of energy between the qubit and resonator but conserves their total number. This Hamiltonian can be diagonalized by the application of a unitary transformation [134, 65, 135]:

$$U = \exp\Big(-\Lambda(a^\dagger\sigma^- - a\sigma^+)\Big) \tag{4.5}$$

for which we define:

$$\Lambda = \frac{1}{2\sqrt{N}} \arctan\left(2\lambda\sqrt{N}\right) \tag{4.6}$$

$$N = a^\dagger a + \sigma^+\sigma^- \tag{4.7}$$

$$\lambda = \frac{g}{\Delta} \tag{4.8}$$

$$\Delta = \omega_\mathrm{a} - \omega_\mathrm{c}. \tag{4.9}$$

The application of this transformation gives:

$$U^\dagger H U = \hbar\omega_c a^\dagger a + \frac{1}{2}\hbar\omega_\mathrm{a}\sigma^z - \frac{1}{2}\hbar\Delta\left(1 - \sqrt{1+4\lambda^2 N}\right)\sigma^z. \tag{4.10}$$

The form above is exact but in the dispersive regime, defined by $g/|\Delta| \ll 1$, it can be approximated by [30, 1]:

$$U^\dagger H U \approx \hbar\left(\omega_\mathrm{c} + \frac{g^2}{\Delta}\sigma^z\right)a^\dagger a + \frac{1}{2}\hbar\left(\omega_\mathrm{a} + \frac{g^2}{\Delta}\right)\sigma^z + \mathcal{O}(\lambda^3). \tag{4.11}$$

In this form we can see a shift in the cavity resonance frequency of $\pm\frac{g^2}{\Delta}$ depending on the state of the qubit. This effect can be seen in network analyzer measurements of the cavity transmission, which are shown in Fig. 4.1.1(d). The middle region where $\omega_\mathrm{f} < \sqrt{\omega_\mathrm{c}^2 - \omega_\Delta^2}$ corresponds to $\Delta > 0$ and in this region two peaks are seen in the cavity transmission. The upper one corresponds to the case where the qubit occupies the ground state, whereas the lower one, which is weaker, corresponds to the case where the qubit occupies the first excited state.

4.4 Qubit driving

We now move on to study the transmission of the resonator when a drive is applied to the qubit. The experimenters tuned the frequency of the qubit to $\omega_\mathrm{a}/2\pi = 5\,\mathrm{GHz}$ by adjusting the external magnetic flux. Meanwhile a signal with angular frequency ω_p and amplitude Ω_q was injected into the control line to drive the qubit. Network analyzer measurements of the cavity transmission as a function of ω_p for two fixed

values of qubit driving amplitude Ω_q are shown in Fig. 4.4.1(a) and (b). In panel (a) we observe two resonances the cavity drive frequency is swept ω_{df}, however one of these resonances is only visible when the qubit drive is tuned close to $\omega_a/2\pi =$ 5 GHz. This is consistent with the expected dispersive shift of the cavity resonance frequency, whose sign is dependent on the state of the qubit. When the qubit drive is detuned only the ground state is occupied, therefore only one resonance is observed. However, when it is brought into resonance, the occupation of the excited state increases and the second resonance becomes visible.

The transmission data in panel (b) was collected after increasing the qubit drive amplitude by a factor of 100 and is is more challenging to interpret. As in panel (a) we see two dispersively shifted resonances, however now both are visible when the qubit drive is detuned. Meanwhile at $\omega_p/2\pi = 5$ GHz both resonances have merged into a single peak. This effect cannot be explained through the dispersive approximation. In order to model it we first introduce the qubit drive to the Hamiltonian according to:

$$H_{\text{driven}}(t) = H + \hbar\Omega_q \cos(\omega_p t)\sigma^x. \tag{4.12}$$

We can remove the time dependence of the Hamiltonian by moving to a frame rotating with the drive and applying the rotating wave approximation. In a rotating frame the Hamiltonian is given by:

$$H_R(t) = V^\dagger(t)HV(t) + i\big(\partial_t V^\dagger(t)\big)V. \tag{4.13}$$

In the current case we choose $V(t) = \exp\Big(-i\omega_p t(a^\dagger a + \sigma^+\sigma^-)\Big)$ which produces:

$$\begin{aligned} H_R(t) =& \hbar(\omega_c - \omega_p)a^\dagger a + \frac{1}{2}\hbar(\omega_a - \omega_p)\sigma^z + \hbar g\sin(\theta)(a\sigma^+ + a^\dagger\sigma^-) \\ &+ \hbar\Omega_q\cos(\omega_p t)\Big(\sigma^+ e^{i\omega_p t} + \sigma^- e^{-i\omega_p t}\Big). \end{aligned} \tag{4.14}$$

After the rotating wave approximation this gives:

$$H_{\mathrm{R}} \approx \hbar(\omega_{\mathrm{c}} - \omega_{\mathrm{p}})a^{\dagger}a + \frac{1}{2}\hbar(\omega_{\mathrm{a}} - \omega_{\mathrm{p}})\sigma^{z} + \hbar g\sin(\theta)(a\sigma^{+} + a^{\dagger}\sigma^{-}) + \frac{1}{2}\hbar\Omega_{\mathrm{q}}\sigma^{x}. \tag{4.15}$$

When a drive is applied to the cavity it probes the transitions between the eigenstates of this Hamiltonian. Significant transmission only occurs when the cavity drive is resonant with a transition and the lower energy level is occupied. By diagonalizing the above Hamiltonian and studying the low lying transitions we produce the black dashed lines in Fig. 4.4.1(b), which align closely with the observed resonances.

In Fig. 4.4.2 we study the dependence of cavity transmission on qubit driving amplitude Ω_{q}. In panel (a) we plot the cavity transmission which was experimentally observed when the driving frequency was fixed at $\omega_{\mathrm{p}}/2\pi = 5.16\,\mathrm{GHz}$. At low drive powers we see the expected pair of dispersively shifted resonances corresponding to the ground and excited states of the qubit. When the drive power is increased to -6 dB these resonances merge before separating again at the even higher powers. In panel (b) we plot cross sections of the transmission at -6 dB and -45 dB. The asymmetry in the line shapes at low driving power indicates nonlinearity in the cavity response, similar to the behaviour observed in [133]. In the high power cross section the two resonances merge into a single peak of width ≈ 200 kHz, which is narrower than the low power resonances which are of width ≈ 1MHz.

This effect is even more pronounced in panels (c) and (d), in which the qubit drive frequency is set to $\omega_{\mathrm{p}}/2\pi = 5.52\,\mathrm{GHz}$. This is sufficiently far detuned from the transition frequency of the qubit that at low drive powers only one resonance is visible. However, as the drive power is increased the second resonance is visible due to the excitation of the qubit. When they merge at -1 dB they produce a sharp peak of width ≈ 70kHz, an order of magnitude sharper than the low power resonance.

It is a challenge to provide an explanation for this linewidth narrowing. It is also a challenge to provide an intuitive explanation for the line merging which accompanies it, despite our diagonalization of the system Hamiltonian providing

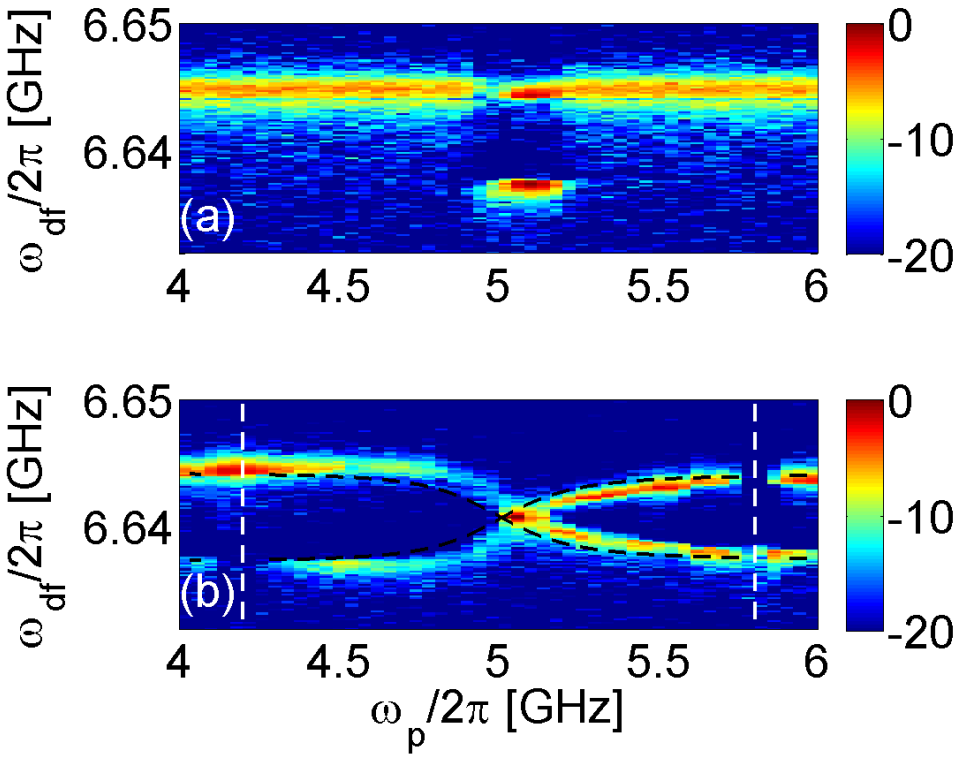

Figure 4.4.1: The effect of qubit driving. Cavity transmission in dB units as a function of qubit driving frequency $\omega_p/2\pi$ and cavity driving frequency $\omega_{df}/2\pi$. The qubit driving amplitude Ω_q in (b) is 100 times larger compared with the values used in (a). For both plots the qubit frequency is given by $\omega_a/2\pi = 5\,\text{GHz}$. The overlaid black dotted line in (b) is obtained by numerically calculating the transition frequencies between the lowest-lying eigenvalues of the Hamiltonian in eq. 4.15 using the following parameters $\Omega_q/2\pi = 0.5\,\text{GHz}$, $\omega_c/2\pi = 6.6408\,\text{GHz}$, $\omega_\Delta/2\pi = 1.12\,\text{GHz}$, $\omega_f/2\pi = 4.9\,\text{GHz}$, $\omega_a/2\pi = 5.0\,\text{GHz}$ and $g\sin(\theta)/2\pi = 0.075\,\text{GHz}$.

a quantitative model. One possibility is that the merging occurs due to motional averaging [136, 137, 138, 139] in which a system whose resonant frequency varies rapidly will respond at the average frequency. In this case the frequency of the cavity is dispersively shifted according to the state of the qubit so we might expect that apply a drive to the qubit will cause Rabi oscillations and induce the resonator to respond at its average frequency. However this fails to explain why increasing the drive power causes the lines to split again. We would not expect motional averaging to disappear when we make the qubit oscillate faster.

Nevertheless, in the following we will propose that this effect may be the result of combination of multistability and motional narrowing occurring when both

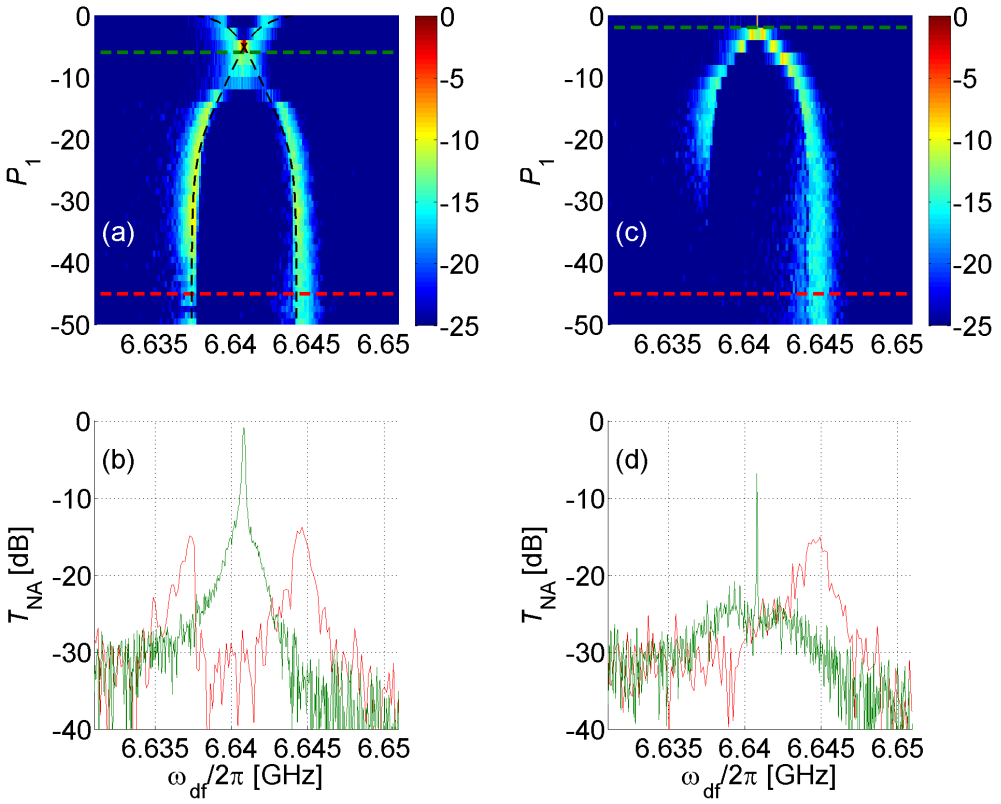

Figure 4.4.2: Dependence on qubit driving amplitude. The driving frequency is $\omega_p/2\pi = 5.16\,\mathrm{GHz}$ in (a) and (b) and $\omega_p/2\pi = 5.52\,\mathrm{GHz}$ in (c) and (d). Cavity transmission in dB units as a function of cavity driving frequency $\omega_{df}/2\pi$ and amplitude (in logarithmic scale) $P_1 = 20\log_{10}\left(\Omega_q/\Omega_{q,0}\right)$ are shown in (a) and (c). Cross sections taken at values of P_1 indicated by colored horizontal dotted lines in (a) and (c) are shown using the corresponding colors in (b) and (d). The overlaid black dotted line in (a) is obtained by numerically calculating the transition frequencies between the eigenvalues of the Hamiltonian (**??**) using the following parameters $\omega_p/2\pi = 5.16\,\mathrm{GHz}$, $\Omega_{q,0}/2\pi = 2.4\,\mathrm{GHz}$, $\omega_\Delta/2\pi = 1.12\,\mathrm{GHz}$, $\omega_f/2\pi = 4.873\,\mathrm{GHz}$, $\omega_a/2\pi = 5.000\,\mathrm{GHz}$ and $g\sin(\theta)/2\pi = 0.075\,\mathrm{GHz}$.

the qubit and cavity are strongly driven. Our analysis is based on applying quantum trajectory methods to the system Hamiltonian including both qubit and cavity drives. However, our study is challenging for several reasons. First, multistability is a nonlinear effect which only appears when the cavity drive is sufficiently strong. This requires that we retain a large Hilbert space size in our calculations. In the following we will include 60 cavity levels. Furthermore, in the presence of both qubit and cavity driving it is not possible to find a frame in which the Hamiltonian is time independent, which adds additional complexity to our calculations. Finally, long integration times are required in order to produce accurate long time averages

in this regime due to critical slowing down in the multistable regime. This prevents us from carrying out simulations for the same parameters as used in the experiment. Therefore we are unable to to make quantitative comparisons with the data collected by the experimenters.

When we include the cavity drive the Hamiltonian is given by:

$$H'_{\mathrm{R}}(t) = H_{\mathrm{R}} + \Omega_{\mathrm{c}}\left(a\exp(i\Delta_{\mathrm{dp}}t) + a^{\dagger}\exp(-i\Delta_{\mathrm{dp}}t)\right) \tag{4.16}$$

where $\Delta_{\mathrm{dp}} = \omega_{\mathrm{df}} - \omega_{\mathrm{p}}$. In order to describe dissipation due to loss of photons from the cavity we use the Lindblad operator $\sqrt{\gamma_{\mathrm{c}}}a$, while to describe dissipation in the qubit we use $\sqrt{\gamma}\sigma^{-}$. After combining these elements, the evolution of the state of the system is described by the Linblad master equation:

$$\partial_t\rho = -\frac{i}{\hbar}[H'_{\mathrm{R}}(t),\rho] + \gamma_c D[a]\rho + \gamma_1 D[\sigma^{-}]\rho. \tag{4.17}$$

The time-dependence of the cavity amplitude $\langle A\rangle = \mathrm{Tr}(\rho(t)A)$ contains two main frequencies $\Delta_{\mathrm{dp}} = \omega_{\mathrm{df}} - \omega_{\mathrm{p}}$ and $\Delta_{\mathrm{cp}} = \omega_{\mathrm{c}} - \omega_{\mathrm{p}}$ due to the drive and cavity frequency respectively. The experimental data presented in Fig. 4.4.2 were measured by mixing the signal transmitted through the cavity with a reference at the cavity drive frequency, as is standard in heterodyne detection. Therefore in order to model the transmitted power T_{NA} we must examine the cavity amplitude $\langle A\rangle$ in a frame rotating with the drive. This is given by

$$\alpha(\Delta_{\mathrm{dp}},t) = \mathrm{Tr}\left(\rho(t)A\right)\exp\left(-i\Delta_{\mathrm{dp}}t\right). \tag{4.18}$$

According to input-output theory T_{NA} will be proportional to the square of this amplitude.

In order to observe narrowing we must drive the cavity in the nonlinear regime. We take a cavity drive amplitude of $\Omega_{\mathrm{c}}/2\pi = 1.00$ MHz. The remaining parameters are set to $\Omega_{\mathrm{q}}/2\pi = 1.726$ MHz, $\omega_{\mathrm{p}}/2\pi = 5.50$ GHz, $g\sin(\theta)/2\pi = 0.075$ GHz, $\omega_{\mathrm{a}}/2\pi = 5$ GHz, $\gamma_c/2\pi = 377$ kHz and $\gamma_1/2\pi = 40.7$ kHz. Using these parameters

we produce the spectrum in Fig. 4.4.3 by evolving the state of our system over 9.6 ms for a range of cavity drive frequencies [74]. The long time average $\overline{\alpha}(\Delta_{\mathrm{dp}})$ displays a full width at half maximum of 125 kHz, significantly less than the natural linewidth of 377 kHz.

This narrowing can be explained when we realise that in the presence of a strong cavity drive the system displays multistability and the line narrowing is due to a bright cavity state (b) which is most stable over a narrow range of frequencies close to the bare cavity resonance. Close to the cavity resonance the system occupies the bright state and the transmitted power is high. However away from this point the system may also occupy two other dim states ($d_{\downarrow}$ and $d_{\uparrow}$), which causes a sharp drop in the transmitted power and a narrow linewidth.

In Fig. 4.4.4 we examine these metastable states more closely. We plot the cavity amplitude and qubit polarization over 170 μs of evolution at $\omega_d/2\pi =$ 6.6409 GHz. The two dim states, labelled $d_{\uparrow}$ and $d_{\downarrow}$, occur when the qubit is polarized in the up and down directions respectively. Meanwhile the bright state occurs when the qubit is depolarised and varies widely over the range $-1 < \langle\sigma^z\rangle < 1$. This behaviour is reminiscent of motional averaging. Since the state of the qubit rapidly varies between the ground and excited states the cavity appears to respond at its bare frequency and form a motionally averaged bright state.

4.5 Cavity driving

In this section we study the response of the cavity in the absence of qubit driving. The nonlinear response of a microwave cavity coupled to a transmon superconducting qubit has recently been studied in Ref. [140] and in chapter 2. The experimental results, together with theoretical analysis [132, 141], indicate that the response to strong cavity driving is affected by the significant coherent driving of the qubit as well as by the stochastic transitions between qubit states. The effect of cavity driving can be characterized by a dephasing rate and by a measurement rate. Both rates have been numerically calculated and analytically estimated in Ref. [142].

Measurements of the cavity transmission T_{NA} of the device under study as a

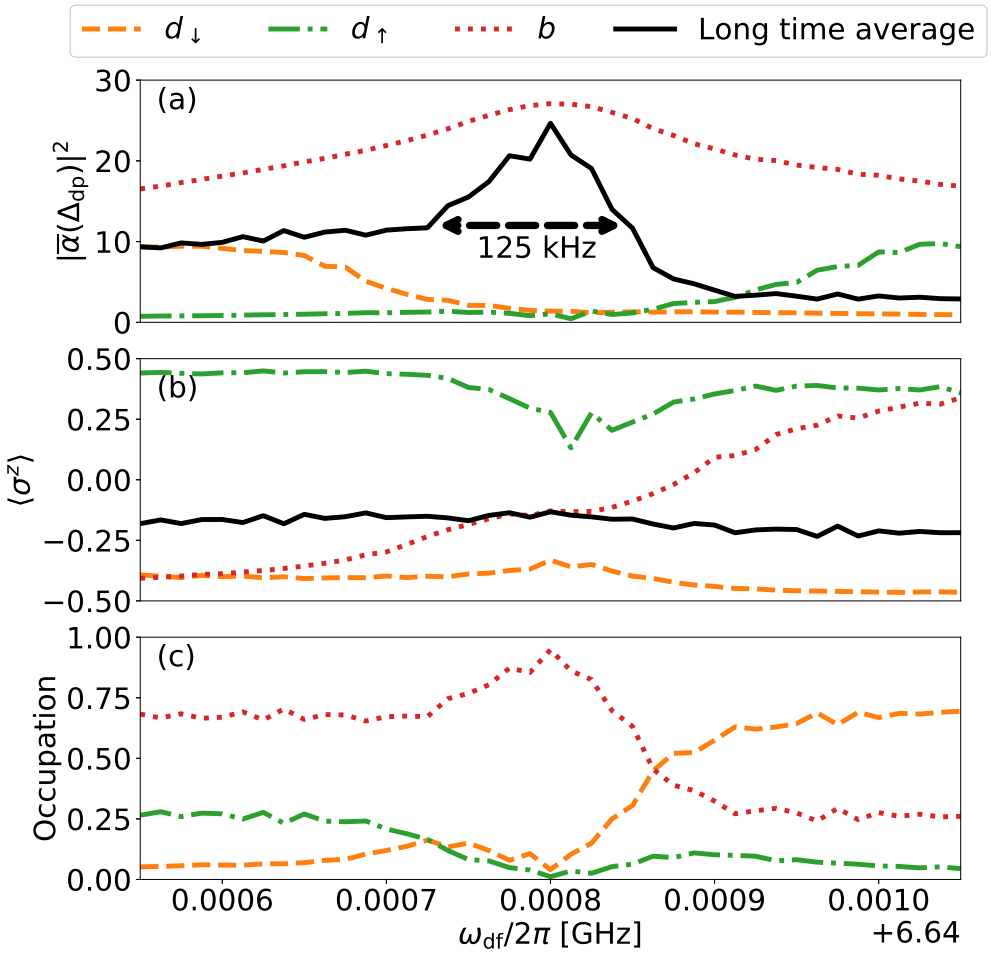

Figure 4.4.3: Simulation of the cavity spectrum in the nonlinear regime. We use a cavity drive amplitude of $\Omega_c/2\pi = 1$ MHz, a qubit drive frequency of $\omega_p = 5.5$ GHz and a qubit drive amplitude of $\Omega_q = 0.863$ GHz. The system displays multistability and three distinct metastable states can be identified, which are labelled by $d_\downarrow$, $d_\uparrow$ and b and assigned the colours orange, green and red respectively. We plot the square cavity amplitude (a), qubit polarization (b) and occupation probability (d) of each of these three states against the cavity drive frequency $\omega_{df}/2\pi$. In panel (a) we see that the cavity amplitude of state b is significantly larger than the amplitudes of states $d_\downarrow$ and $d_\uparrow$. Hence we refer to b as bright and $d_\downarrow$ and $d_\uparrow$ as dim. The black line is produced by averaging the cavity amplitude over 9.6 ms of evolution before taking the square of the absolute value. It displays a narrow resonance at the bare cavity frequency. The full width at half maximum is only 125 kHz, which is 33% of the natural linewidth of 377 kHz. In panel (b) we see that states $d_\downarrow$ and $d_\uparrow$ occur when the qubit is polarized up and down respectively whereas the qubit polarization associated with state b varies with the drive frequency. Finally in panel (c) we see the occupation probabilities of the three states. Away from the cavity resonance the stability of state b falls. This causes the narrowing observed in panel (a).

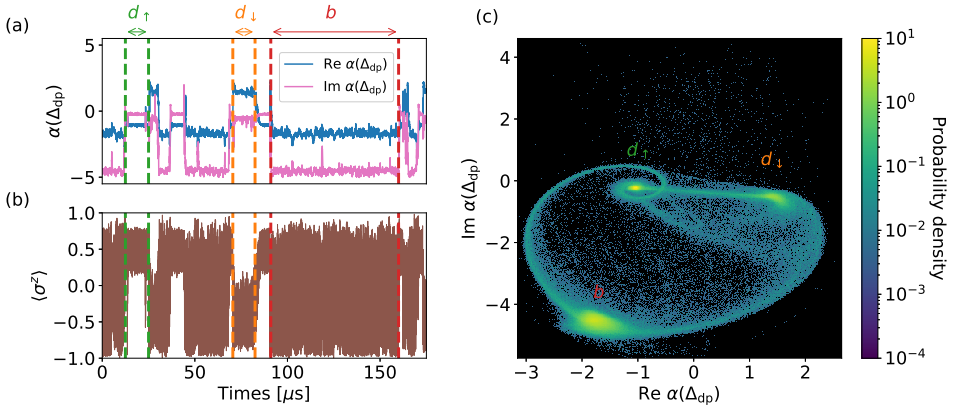

Figure 4.4.4: Here we examine a quantum state trajectory produced at $\omega_{df}/2\pi = 6.6409$ GHz. In panel (a) we plot the real and imaginary parts of the cavity amplitude. The cavity is observed to jump between three metastable states. Examples of states $d_\uparrow$, $d_\downarrow$ and b are highlighted between the vertical dashed lines in green, orange and red respectively. By referring to panel (b) we see that state $d_\uparrow$ occurs when the qubit has positive polarization, state $d_\downarrow$ occurs when it has negative polarization and state b occurs when the qubit freely varies over the range $-1 < \langle\sigma^z\rangle < 1$. In panel (c) we plot a histogram of the cavity amplitude throughout 9.6 ms of evolution. The three metastable states are clearly identified as three clusters in the plane. Switching pathways leading between these clusters can also be observed.

function of cavity driving frequency $\omega_{df}/2\pi$ and power P_{da} are shown in Fig. 4.5.1. No qubit driving is applied during these measurements. We demonstrate nonlinearity of the softening type in Fig. 4.5.1(a-c), whereas hardening is demonstrated in Fig. 4.5.1(d-f). We obtained the data shown in Fig. 4.5.1 by sweeping the cavity driving frequency $\omega_{df}/2\pi$ upwards. Almost no hysteresis is observed when the sweeping direction is flipped.

The measured cavity transmission T_{NA} can be compared with theoretical predictions based on the semiclassical approximation. Such a comparison has previously been performed in Ref. [133] based on data that has been obtained from the same device. Good quantitative agreement was found in the region of relatively small cavity driving amplitudes [133].

However, when the cavity is strongly driven, the nonlinearity introduced to the system by the qubit causes the onset of bistability and the semiclassical approximation alone is unable to reproduce the cavity transmission. This is because, despite accurately modeling the fixed points, which henceforth are referred to as the bright

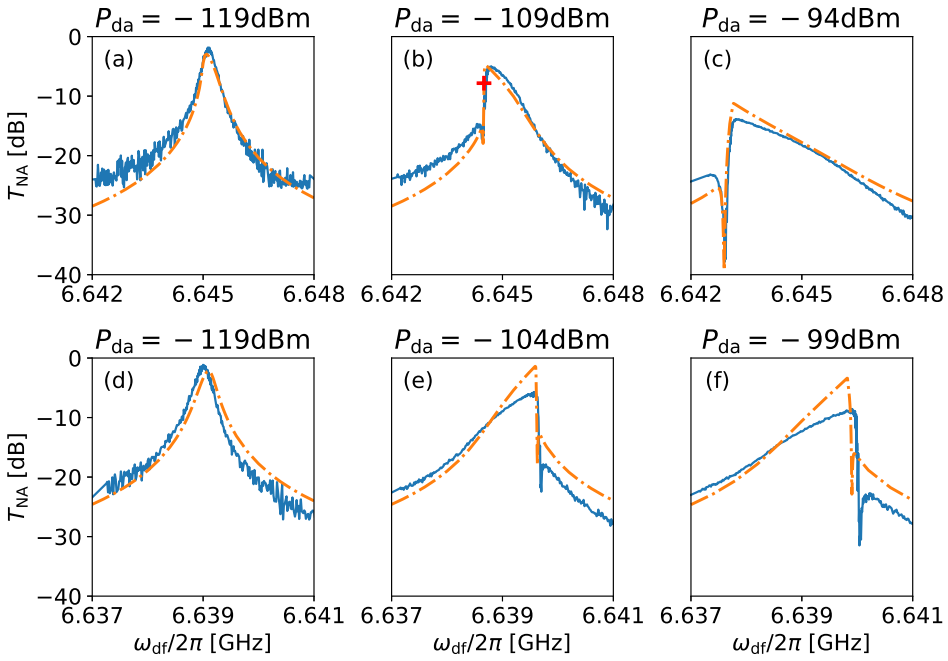

Figure 4.5.1: Nonlinear response to cavity driving. The cavity transmission T_{NA} is measured as a function of cavity driving frequency $\omega_{df}/2\pi$ for different values of the cavity driving power P_{da}. These data are compared with a numerical calculation of the steady state of the Lindblad master equation (dashed red line). In (a-c) the frequency $\omega_f/2\pi$ is flux-tuned to 5.5 GHz, and in (d-f) to 7.8 GHz. Different values of γ_c are used at each drive power to account for the increase in the quality factor of the cavity with occupation. We use $\gamma_c =$ (a) 0.314, (b) 0.251, (c) 0.126, (d) 0.314, (e) 0.251 and (f) 0.126 MHz.

and dim metastable states (see Fig. 4.5.2), the semiclassical equations of motion give no information regarding the occupation probabilities of the two metastable states in the overall state of the system, which can be written as:

$$\rho = p_b \rho_b + p_d \rho_d \tag{4.19}$$

where $\rho_b(\rho_d)$ and $p_b(p_d)$ represent the bright (dim) state and its probability respectively.

The experimental results shown in Fig. 4.5.1 exhibit a sharp dip in cavity transmission T_{NA} at drive powers above -109dBm. A very similar feature has been experimentally observed before in [140] and theoretically discussed in Refs. [132, 141], for which the full quantum theory of the single nonlinear oscillator

has been developed in [143]. The origin of this dip is the destructive interference between the two metastable states. Since the system is coupled to an external reservoir, fluctuations in the quantum state ensue and occasionally cause major switching events between the bright and dim states. When the complex amplitude of the cavity state is averaged over an ensemble of many such switching events, there is typically a narrow region in the frequency-power space where the two complex amplitudes partially cancel each other. By using the Lindblad master equation to model the system, we are able to take account of these fluctuations which cause these switching events and we produce the numerical fits seen in Fig. 4.5.1.

In order to calculate the response of our system to cavity driving (without qubit driving) we use the following master equation:

$$\partial_t \rho = -\frac{i}{\hbar}[H,\rho] + \gamma_c D[A]\rho + \gamma_1 D[\sigma_-]\rho, \tag{4.20}$$

where the Hamiltonian a frame rotating with the cavity drive is given by:

$$H \approx \hbar(\omega_c - \omega_{df})a^\dagger a + \frac{1}{2}\hbar(\omega_a - \omega_{df})\sigma^z + \hbar g\sin(\theta)(a\sigma^+ + a^\dagger\sigma^-) + \frac{1}{2}\hbar\Omega_c(a + a^\dagger). \tag{4.21}$$

In the above the detuning between the cavity drive and the cavity resonance is given by $\Delta_{dc} = \omega_{df} - \omega_c$, while the detuning between the cavity drive and the qubit frequency is given by $\Delta_{da} = \omega_{df} - \omega_a$. Since the relaxation rate of the qubit depends on the magnetic field detuning from the symmetry point we must take account of this in our calculations. For Figs. 4.5.1(a-c) we have $\omega_f/2\pi = 5.5$GHz and $\gamma_1/2\pi = 6.29$kHz, whereas for Figs. 4.5.1(d-f) we have $\omega_f/2\pi = 7.8$GHz and $\gamma_1/2\pi = 4.02$kHz.

The master equation above does not include a Lindblad operator to describe pure dephasing of the flux qubit. Since we are operating the qubit far from its symmetry point, pure dephasing will be dominated by flux noise, and in [111] the power spectral density (PSD) of this noise was found to have a $1/f^{0.9}$ form. Unfortunately we cannot account for this noise in the master equation, because the Markovian

approximation requires that the PSD is well-behaved at zero frequency. However, even without the inclusion of pure dephasing, the master equation is still able to explain the major features of the spectra measured in Fig. 4.5.1.

Comparison between the predictions derived from the numerical integration of the master equation and the ones analytically derived from the semiclassical equations of motion is shown in Fig. 4.5.2.

4.6 Summary

Our main finding is the linewidth narrowing that is obtained by applying intense qubit driving. The experimenters showed that this effect is robust, however, its theoretical modeling is quite challenging. We have made a qualitative comparison with the results of a simulation which display linewidth narrowing due to a bright metastable state with a narrow range of stability. We also speculated that this bright state could be an example of motional averaging. Further work should explore this possibility more deeply and aim to understand if the motionally averaged bright state is stable over only a narrow range of qubit drive powers.

We also find that bistability, which is predicted by the semiclassical model for monochromatic cavity driving, is experimentally inaccessible. This effect and related observations can be satisfactorily explained using numerical integration of the master equation for the coupled system.

Contributions

This chapter is based on published work [102]. The experimental data presented in this chapter were collected by Eyal Buks in collaboration with Chunqing Deng, Jean-Luc Orgiazzi and Martin Otto in the group of Adrian Lupascu at the Institute for Quantum Computing, University of Waterloo. Paul Brookes and Eyal Buks interpreted the data. Paul Brookes performed the numerical calculations presented in this chapter under the supervision of Eran Ginossar.

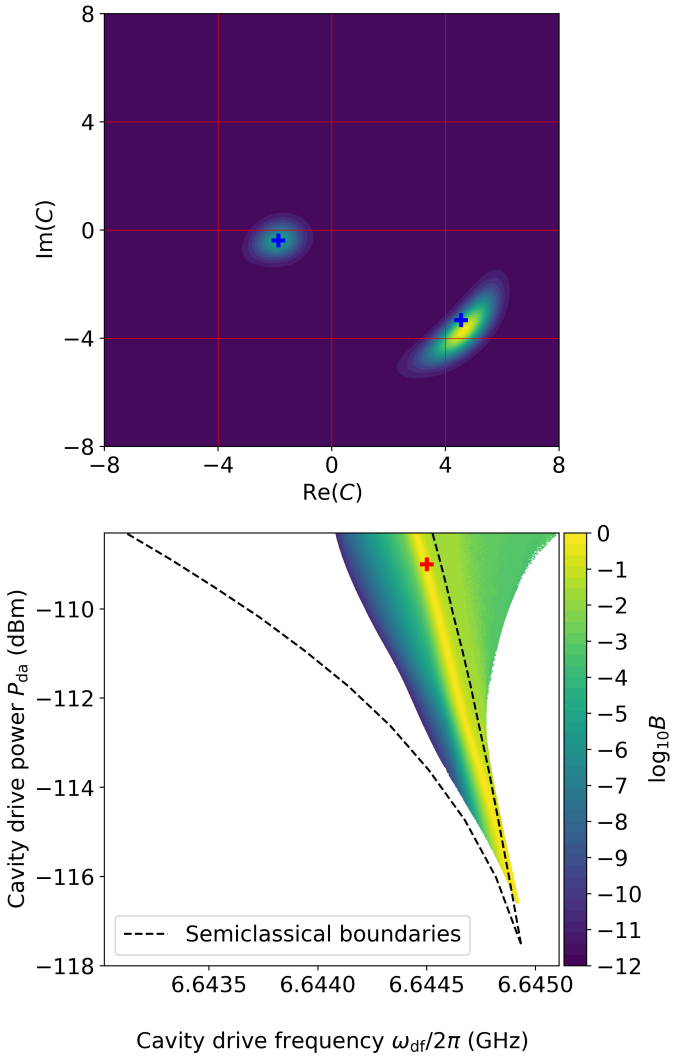

Figure 4.5.2: The bistable regime. The cavity drive power is given by $P_{\mathrm{da}} = 20\log_{10}(\Omega_{\mathrm{c}}/\omega_{2,0})$ where $\omega_{2,0}/2\pi = 340\,\mathrm{GHz}$. In (a) we plot the Wigner function of the cavity state in the bistable regime, which is obtained by solving for the steady state of the master equation at a drive power of $P_{\mathrm{da}} = -109\mathrm{dBm}$ and a drive frequency of $\omega_{\mathrm{da}}/2\pi = 6.6445\mathrm{GHz}$. These parameters are marked by the red crosses in panel (b) and in Fig. 4.5.1(b). Two metastable states can be seen: a bright state at $C_{\mathrm{b}} = 4.64 - 3.73i$ and a dim state at $C_{\mathrm{d}} = -1.88 - 0.39i$. These two states correspond to the fixed points produced using the semiclassical equations of motion, marked by blue crosses. Next in (b) we examine the boundaries of the bistable regime. By examining the cavity Wigner function over a range of drive powers and frequencies we map the region in which we find two peaks corresponding to the bright and dim states. When two peaks can be identified we calculate the metric $B = 1 - |p_b - p_d|$ as a measure of bistability. This is plotted in the colormap above. Meanwhile the dashed black lines mark the boundaries of the region in which the semiclassical equations of motion have two fixed points. These methods produce significant overlap and both predict the onset of bistability around $P_{\mathrm{da}} = -117\mathrm{dB}$. We also see that the region of maximum bistability predicted by the master equation (yellow strip) lies either close to or within the semiclassical bistable region at all powers. However there are significant differences in the limits of the bistable region, particularly at the upper freuqency limit. The master equation predicts this limit should increase with drive power, whereas the semiclassical equations predict the opposite.

Chapter 5

Long range couplings in a spin chain and the protection of quantum information

In this chapter we shall change theme. Whereas the previous chapters dealt with nonlinear effects in coupled resonator-qubit systems, in this chapter we shall present a new qubit design based on a spin chain model obeying certain common symmetries, such as invariance under translation or inversion, and demonstrate that these symmetries can produce eigenstates which have some degree of protection against decoherence. These states can be found among the excited states of many well studied models, but we will demonstrate that using long range interactions these states can be brought down to the low lying part of the spectrum where they can be used to encode information. Models containing long range interactions generally receive less attention because they are assumed to be less physically realistic, but we will highlight such a model which not only produces some interesting coherence properties but can also be engineered in a laboratory.

5.1 Symmetries and a toy model

Let us begin by discussing the relevant symmetries. We consider a periodic chain containing an even number of spins M and we introduce the operators σ_m, $\mathcal{N}$, $\mathcal{T}$ and $\mathcal{I}$. The operator σ_m is a local Pauli operator acting on site m while the hermitian

operator $\mathcal{N}$ is corresponds to the total number of excitations in the chain $\mathcal{N} = \sum_{m=1}^{M}(\sigma_m^+\sigma_m^- - \frac{1}{2})$. The operators $\mathcal{T}$ and $\mathcal{I}$ are unitary and they act to either displace the chain by a single site $\mathcal{T}\sigma_m\mathcal{T}^{-1} = \sigma_{m+1}$ or to invert the chain around the central bond $\mathcal{I}\sigma_m\mathcal{I} = \sigma_{M+1-m}$. Using these transformations it is straightforward to show that σ_m can be written as

$$\sigma_m = \mathcal{T}^{2m-M-1}\underbrace{\mathcal{I}\sigma_m\mathcal{I}}_{\sigma_{M+1-m}}\mathcal{T}^{-(2m-M-1)}. \tag{5.1}$$

Essentially we have inverted the site on which the Pauli operator acts before translating it back to its original location. Now let's imagine that we can find two states of the chain, denoted by $|\uparrow\rangle$ and $|\downarrow\rangle$, which are simultaneously eigenstates of the translation, inversion and number operators with the following eigenvalues

$$\mathcal{N}|\uparrow\rangle = N|\uparrow\rangle, \quad \mathcal{N}|\downarrow\rangle = N|\downarrow\rangle \tag{5.2a}$$

$$\mathcal{T}|\uparrow\rangle = |\uparrow\rangle, \qquad \mathcal{T}|\downarrow\rangle = |\downarrow\rangle \tag{5.2b}$$

$$\mathcal{I}|\uparrow\rangle = |\uparrow\rangle, \qquad \mathcal{I}|\downarrow\rangle = -|\downarrow\rangle \tag{5.2c}$$

Using these properties we will now demonstrate that at first order our chosen states are immune to relaxation and dephasing due to noise channels acting on single sites. We start by looking at relaxation, which should be proportional to matrix elements of the form $\langle\uparrow|\sigma_m|\downarrow\rangle$. But using the eigenvalues above in combination with eq. 5.1 we can show that these matrix elements vanish:

$$\langle\uparrow|\sigma_m|\downarrow\rangle = \underbrace{\langle\uparrow|\mathcal{T}^{2m-M-1}\mathcal{I}}_{\langle\uparrow|}\sigma_m\underbrace{\mathcal{I}\mathcal{T}^{-(2m-M-1)}|\downarrow\rangle}_{-|\downarrow\rangle} = -\langle\uparrow|\sigma_m|\downarrow\rangle = 0. \tag{5.3}$$

In other words the symmetry properties of our states have allowed us to prove that the transition matrix element of a Pauli operator $\langle\uparrow|\sigma_m|\downarrow\rangle$ is equal to minus itself, and is therefore zero.

Next we consider dephasing, which should occur at a rate proportional to $|\langle\uparrow|\sigma_m|\uparrow\rangle - \langle\downarrow|\sigma_m|\downarrow\rangle|$ i.e. the first order shift in the energy splitting of our states

induced by noise acting on a Pauli operator σ_m. We first consider σ_m^z Pauli operators. Using the translation operator we show that the expectation value of $\mathcal{N}$ for the $|\uparrow\rangle$ state is given by:

$$\langle\uparrow|\mathcal{N}|\uparrow\rangle = \sum_{m=0}^{M-1} \langle\uparrow|\mathcal{T}^m\sigma_1^z\mathcal{T}^{-m}|\uparrow\rangle = M\langle\uparrow|\sigma_m^z|\uparrow\rangle \tag{5.4}$$

and in the same way we can also demonstrate $\langle\downarrow|\mathcal{N}|\downarrow\rangle = M\langle\downarrow|\sigma_m^z|\downarrow\rangle$. But since the eigenvalues in eq. 5.2a tell us $\langle\uparrow|\mathcal{N}|\uparrow\rangle = \langle\downarrow|\mathcal{N}|\downarrow\rangle = N$ we find $\langle\uparrow|\sigma_m^z|\uparrow\rangle = \langle\downarrow|\sigma_m^z|\downarrow\rangle = N/M$. Therefore the states are immune to σ_m^z noise to first order. In addition, since $[\mathcal{N},\sigma_m^\pm] = \pm\sigma_m^\pm$ we know that the action of the $\sigma_m^\pm$ operator is to map the states to orthogonal eigenstates of $\mathcal{N}$ with eigenvalues $N\pm 1$. Therefore $\langle\uparrow|\sigma_m^\pm|\uparrow\rangle = \langle\downarrow|\sigma_m^\pm|\downarrow\rangle = 0$. This means that our states are also immune to dephasing acting on $\sigma_m^\pm$ or any superposition thereof, such as σ_m^x or σ_m^y.

Unfortunately it is not easy to find a model which produces such states in usable form. There are many examples of models which obey the necessary symmetries and produce the desired eigenstates, but in order to use these states conveniently as a basis for a qubit they must be well separated from the rest of the spectrum. For example, we might expect to find such states in the XX model, wherein the spins of the chain are coupled only by nearest neighbour flip-flop interactions. This model conserves $\mathcal{N}$ and is symmetric under both translation and inversion. Indeed, the spectrum of the XX model contains a degenerate manifold, within which lie two states satisfying the required symmetries. But, since they are both intermediate in the spectrum and degenerate with multiple other states, they cannot be used.

For our purposes we will investigate a modified XX model consisting of a periodic chain of 6 spins which are coupled by three different kinds of interactions. Flip-flop interactions exchange excitations between neighbouring sites in the ring at a rate t and between diametrically opposite sites in the ring at a rate λ. In addition there is an all-to-all $\sigma^z\otimes\sigma^z$ coupling with strength ζ. This model is described by

the following Hamiltonian:

$$H = \sum_{m=0}^{N-1} \left(\frac{t}{2}(\sigma_m^+ \sigma_{m+1}^- + \sigma_m^- \sigma_{m+1}^+) - \frac{\lambda}{2}(\sigma_m^+ \sigma_{m+3}^- + \sigma_m^- \sigma_{m+3}^+) \right) + \frac{\zeta}{4} \sum_{m,n=0}^{N-1} \sigma_m^z \sigma_n^z \tag{5.5}$$

which is illustrated in Fig. 5.1.1(a). Using this model we show in Fig. 5.1.1(b) and (c) that it is possible to produce a qubit manifold which satisfies the above symmetries and is therefore protected against relaxation and dephasing. We quantify the sensitivity to relaxation by

$$R^2 = \sum_{w \in \{x,y,z\}} |\langle\uparrow| \sigma_m^w |\downarrow\rangle|^2 \tag{5.6}$$

and the sensitivity to dephasing by

$$D^2 = \sum_{w \in \{x,y,z\}} |\langle\uparrow| \sigma_m^w |\uparrow\rangle - \langle\downarrow| \sigma_m^w |\downarrow\rangle|^2. \tag{5.7}$$

By plotting these quantities as a function of ζ and λ we observe regions in which the sensitivities to relaxation and dephasing are suppressed. The hatched regions which are overlain indicate the areas of parameter space in which the symmetries listed in eqs. 5.2 are obeyed by the lowest two eigenstates of the Hamiltonian. As expected, these co-indicate with the protected regions.

Here we note that the suppression of D can also be connected to time reversal symmetry. The time reversal operator is given by:

$$U = i\sigma^y K \tag{5.8}$$

where K is the antiunitary complex conjugation operator. The action of U on a Pauli operator is given by:

$$U^\dagger \sigma^w U = -\sigma^w. \tag{5.9}$$

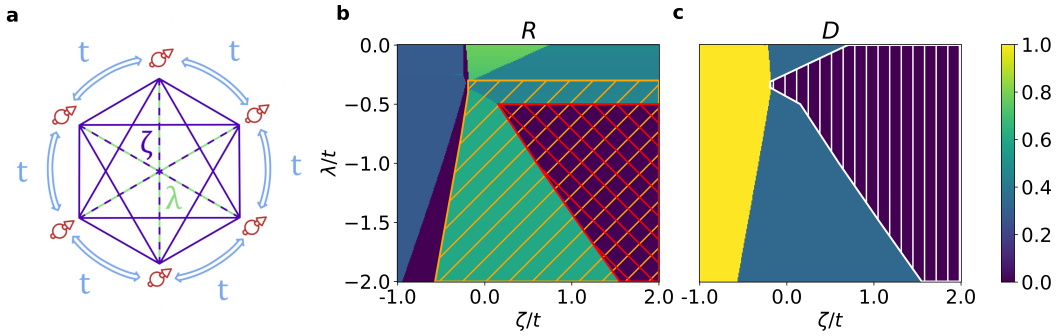

Figure 5.1.1: Decoherence properties of a periodic chain containing six spins with long range couplings. (b) Schematic representation of the Hamiltonian of the chain. Each spin (represented in red) is coupled by flip-flop interactions to both its nearest neighbours (t, blue arrows) and to its diametrically opposite counterpart (λ, green lines). In addition there are $\sigma^z \otimes \sigma^z$ interactions between all spins in the chain (ζ, purple lines). Sensitivity to relaxation R (b) and dephasing D (c) of a superposition of the two lowest energy states vs the strengths of the long range interactions ζ and λ. The black coloured regions indicate parameters where the ground and first excited state of the chain are protected against local perturbations. Three regions are highlighted to indicate different kinds of symmetries obeyed by the ground and first excited states. The red hatched region indicates that both states are invariant under the action of the translation operator $\hat{\mathcal{T}}$ while the orange hatched region indicates that the ground (resp. first excited) state is an eigenvector of the inversion operator $\hat{\mathcal{I}}$ with eigenvalue +1 (resp. -1). Finally the white hatched region indicates that the ground and first excited states are eigenvectors of the total number of excitations $\hat{N}_{\text{tot}}$ with eigenvalue 3.

Since our model in eq. 5.5 only contains pairs Pauli operators, we can see that the time-reversal operator will leave the Hamiltonian unchanged. Therefore, assuming our states are not degenerate with any others, the action of the time reversal operator will be to map them back to themselves, possible acquiring a phase:

$$U|s\rangle = \exp(i\phi_s)|s\rangle \tag{5.10}$$

where $s \in \{\uparrow,\downarrow\}$. We can combine this information to demonstrate vanishing expectation values as follows. From the above we see that the expectation value of operator σ^w in state $U|s\rangle$ is given by:

$$\langle s|U^\dagger \sigma^w U|s\rangle = \langle s|\sigma^w|s\rangle\,. \tag{5.11}$$

Simultaneously from eq. 5.9 we see:

$$\langle s| U^{\dagger}\sigma^{w}U |s\rangle = -\langle s| \sigma^{w} |s\rangle . \tag{5.12}$$

Therefore $\langle s| \sigma^{w} |s\rangle = -\langle s| \sigma^{w} |s\rangle = 0$.

If the system contains an odd number of sites then the total spin will be a half integer and according to Kramers theorem all eigenstates of the Hamiltonian will form degenerate multiplets and the action of the time reversal operator will be non-trivial. Therefore for the above argument to hold the chain must contain an even number of sites.

5.2 Circuit design

This development is promising, however it is a challenging task to find a physical system where long range interactions are not only of similar strength to the nearest neighbour interactions but also of opposite sign. Fortunately for us, the toolset of superconducting electronics offers methods to engineer such interactions via directly connecting distant sites in a chain. In the following we propose an implementation of our Hamiltonian using an array of Josephson junctions. In our design the spins are formed by the radial Josephson junctions shown in blue in Fig. 5.2.1(a), which have Josephson energy E_{Jr} and charging energy E_{Cr}. Each junction, whose gate charge is tuned to $N_g = 0.5$, forms a Cooper pair box superconducting qubit.

These qubits are coupled to their nearest neighbours via Josephson junctions with Josephson energy E_{Ja} and to their diametrically opposite counterparts via Josephson junctions of Josephson energy E_{Jl}. These two types of junctions will henceforth be referred to as azimuthal and diametric junctions. Tunneling across these junctions can be used to recreate the flip-flop coupling above. Meanwhile the charging energies of the azimuthal junctions E_{Ca} are chosen such that $E_{Ca}/E_{Cr} \ll 1$. In this case a long range charge coupling of strength $\sim E_{Cr}$ arises between the qubits which recreates the all-to-all $\sigma^{z} \otimes \sigma^{z}$ coupling.

The relative sign of the flip-flop interactions is controlled by the choice of the flux threading through the circuit. At the optimal point the flux threading through

each internal sector is tuned to half a flux quantum $\Phi_0/2$, while the flux threading the outer loops is $3\Phi_0/2$. This can be easily arranged by applying a homogeneous external magnetic field and choosing the appropriate circuit dimensions. For ease of fabrication we choose all three junction types to have the same plasma frequency $\sqrt{8E_JE_C}/h = 10$ GHz. In Fig. 5.2.1(b) we plot the transition frequency between the ground ($|0\rangle$) and first excited ($|1\rangle$) states of the circuit $\omega_{01}/2\pi$ as a function of E_{Cr}/E_{Ja} and E_{Jl}/E_{Ja} assuming $E_{Ja}/h = 6$ GHz. These axes are analogous to those used in Fig. 5.1.1(b) since the strengths of the nearest neighbour flip-flop, range 3 flip-flop and all-to-all $\sigma^z \otimes \sigma^z$ couplings are proportional to E_{Ja}, E_{Jl} and E_{Cr} respectively.

We shall now outline the process of quantizing this circuit and obtaining the Hamiltonian, which is explained in more detail in [14, 15, 144]. The circuit is treated as a graph consisting of a grounded node in the centre connected to 6 outer nodes via radial Josephson junctions. The voltage of node n at time t is written as $v_n(t)$, from which we define the node fluxes by $\phi_n(t) = \int_{-\infty}^{t'} v_n(t')dt'$. The Lagrangian is then divided into a kinetic part T which consists of the capacitive charging energies, and a potential part V which is the sum of the inductive energies of the Josephson junctions. If we denote the capacitances of the radial, azimuthal (nearest-neighbour) and diametric (next-next-nearest-neighbour) junctions by C_r, C_a and C_l respectively then we can write the kinetic term as

$$T = \frac{1}{2}\sum_{m=1}^{6}\left(C_a(\dot{\phi}_{m+1}-\dot{\phi}_m)^2 + C_r\dot{\phi}_m^2\right) + \frac{1}{2}\sum_{m=1}^{3} C_l(\dot{\phi}_{2m}-\dot{\phi}_{2m+3})^2 \tag{5.13}$$

$$= \frac{1}{2}\sum_{m,n=1}^{6} \mathbf{C}_{mn}\dot{\phi}_m\dot{\phi}_n \tag{5.14}$$

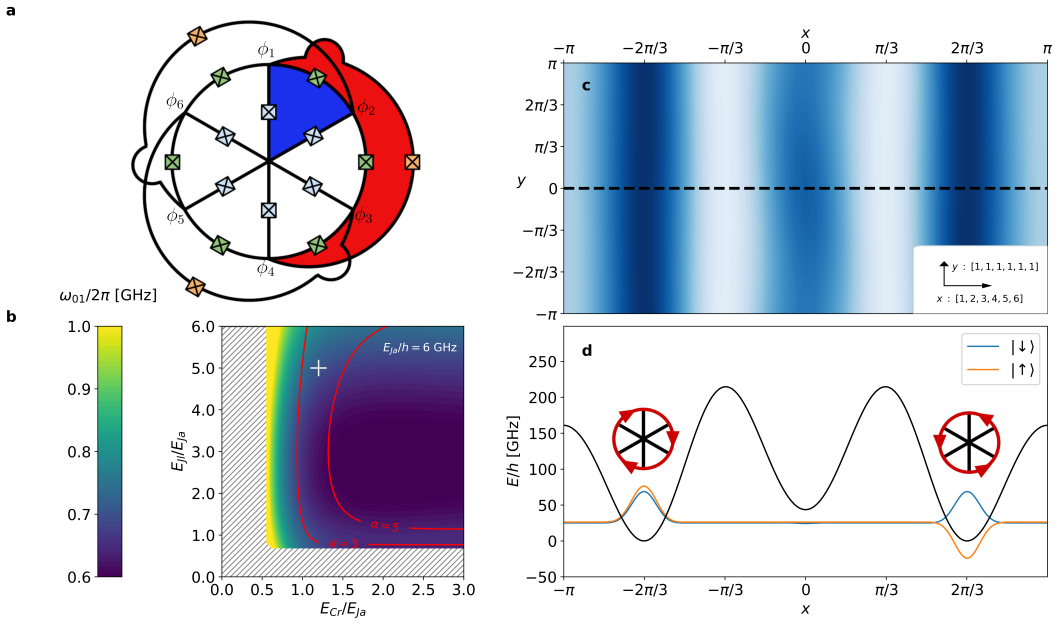

Figure 5.2.1: Realizing the protected states in a superconducting circuit. (a) Circuit diagram of the qubit showing a superconducting loop intersected by six identical azimuthal Josephson junctions of Josephson energy E_{Ja} (green). Each of the islands - whose phases are labelled ϕ_1 to ϕ_6 - is connected both radially to ground via a Josephson junction of charging energy E_{Cr} (blue) and to its diametrically opposite counterpart by a junction with Josephson energy E_{Jl} (orange). (b) Transition frequency to the first excited state of the qubit $\omega_{01}/2\pi$ as a function of E_{Cr}/E_{Ja} and E_{Jl}/E_{Ja} assuming *all the junctions of the circuit have the same plasma frequency* $\sqrt{8E_JE_C}/h = 10$ GHz. The hatched region corresponds to parameters where the ground and first excited states do not exhibit the required symmetries for protection of the qubit against decoherence. The red lines indicate contours of constant anharmonicity $\alpha = \omega_{12}/\omega_{01}$. The white cross corresponds to the qubit parameters we chose for the remainder of the article. (c) Potential landscape in the (x, y) plane. In this plane two valleys of global minima can be seen. The wavefunctions of the ground and first excited state are localised in the potential minima. (d) Potential energy along the horizontal direction shown in (c) as a dashed black line. Two global potential minima are observed for $x = \pm 2\pi/3$ and correspond to states with clockwise or anti-clockwise current flowing in the circuit. The ground (resp. first excited) state wavefunction consists of a symmetric (resp. anti-symmetric) superposition of these states.

where in the second line we have introduced the capacitance matrix:

$$\mathbf{C} = \begin{pmatrix} C_r+2C_a+C_l & -C_a & 0 & -C_l & 0 & -C_a \\ -C_a & C_r+2C_a+C_l & -C_a & 0 & -C_l & 0 \\ 0 & -C_a & C_r+2C_a+C_l & -C_a & 0 & -C_l \\ -C_l & 0 & -C_a & C_r+2C_a+C_l & -C_a & 0 \\ 0 & -C_l & 0 & -C_a & C_r+2C_a+C_l & -C_a \\ -C_a & 0 & -C_l & 0 & -C_a & C_r+2C_a+C_l \end{pmatrix}. \tag{5.15}$$

In order to write down the potential term we must be careful to take account of any fluxes which may be threading through the loops of the circuit. We first define a spanning tree which reaches all nodes of the circuit without forming any loops. In our case this spanning tree consists of all the radial Josephson junctions. Each Josephson junction in the circuit makes a contribution to the inductive energy of the form $-E_J\cos(\phi/\varphi_0)$ where ϕ is the difference in node fluxes across that junction. For junctions lying within the spanning tree, i.e. the radial junctions, this phase difference is simply given by the node fluxes $\phi_n(t)$. However if the junction lies outside the spanning tree then the flux difference must account for the external flux threaded through the loop it forms. According to Maxwell's equations the change in potential energy when traversing a loop is proportional to the rate of change of magnetic flux through that loop:

$$\oint \mathbf{E}\cdot d\mathbf{x} = -\partial_t \Phi_{\text{ext}}. \tag{5.16}$$

If we integrate this relation over time then we find that the sum of flux differences across circuit elements within a loop will be equal to the external flux threading the loop. This allows us to write the flux differences across the mth azimuthal $\Delta\phi_{a,m}$

and diametric $\Delta\phi_{l,m}$ junctions as

$$\Delta\phi_{a,m} = \phi_{m+1} - \phi_m - \Phi_{a,m} \tag{5.17}$$

$$\Delta\phi_{l,m} = \phi_{2m+3} - \phi_{2m} - \Phi_{l,m} \tag{5.18}$$

where $\Phi_{a,m}$ and $\Phi_{l,m}$ are the external fluxes threading through the loops formed by these junctions. Finally, these flux differences can be used to write the potential part of the Lagrangian as

$$\begin{aligned} V = &- E_{Jr} \sum_{m=1}^{6} \cos\left(\frac{\phi_m}{\varphi_0}\right) - E_{Ja} \sum_{m=1}^{6} \cos\left(\frac{\phi_{m+1} - \phi_m - \Phi_{am}}{\varphi_0}\right) \\ &- E_{Jl} \sum_{m=1}^{3} \cos\left(\frac{\phi_{2m+3} - \phi_{2m} - \Phi_{lm}}{\varphi_0}\right). \end{aligned} \tag{5.19}$$

where φ_0 is the reduced flux quantum. To convert this Lagrangian to the form of a Hamiltonian we must first obtain the node charges. These are given by

$$q_m = \frac{\partial L}{\partial \dot{\phi}_m} \tag{5.20a}$$

$$= \sum_{n=1}^{6} C_{mn}\dot{\phi}_n \tag{5.20b}$$

After performing a Legendre transformation the Hamiltonian is given by

$$H = \sum_{m=1}^{6} \dot{\phi}_m q_m - L \tag{5.21a}$$

$$= T + V \tag{5.21b}$$

where we now express the kinetic term as

$$T = \frac{1}{2} \sum_{m,n=1}^{6} \mathbf{C}^{-1}_{mn} q_m q_n \tag{5.22}$$

This Hamiltonian can be quantized by replacing $q_n \to 2e(\hat{N}_n - N_{g,n})$ and $2\pi\phi_n/\Phi_0 \to \hat{\theta}_n$ where $N_{g,n}$ is the gate charge on site n and the commutation re-

lation $[\hat{\theta}_n, \hat{N}_n] = i$ holds. This gives the complete Hamiltonian in the form

$$\begin{aligned} H =& 2e^2 \sum_{m,n=1}^{6} \mathbf{C}^{-1}_{mn}(\hat{N}_m - N_{g,m})(\hat{N}_n - N_{g,n}) - E_{Jr} \sum_{m=1}^{6} \cos\left(\hat{\theta}_m\right) \\ & - E_{Ja} \sum_{m=1}^{6} \cos\left(\hat{\theta}_{m+1} - \hat{\theta}_m - \frac{\Phi_{am}}{\varphi_0}\right) \\ & - E_{Jl} \sum_{m=1}^{3} \cos\left(\hat{\theta}_{2m+3} - \hat{\theta}_{2m} - \frac{\Phi_{lm}}{\varphi_0}\right). \end{aligned} \tag{5.23}$$

If denoted the fluxes through the six inner and three outer loops of the circuit by $\Phi_{I,m}$ and $\Phi_{O,m}$ then we can rewrite the external fluxes as:

$$\Phi_{am} = \Phi_{I,m}, \qquad \Phi_{lm} = \Phi_{I,m} + \Phi_{I,m+1} + \Phi_{I,m+2} + \Phi_{O,m}. \tag{5.24}$$

We can now demonstrate the relationship between this Hamiltonian and our original spin model more clearly. We start with the potential term which recreates the flip-flop couplings of the spin-1/2 model. We can see this by rewriting the potential in terms of the tunneling operators

$$\Sigma^+ = \sum_n |n+1\rangle\langle n|, \tag{5.25a}$$

$$\Sigma^- = \sum_n |n\rangle\langle n+1| \tag{5.25b}$$

which cause Cooper pairs to tunnel back and forth across the radial junctions, and are written in terms of the Cooper pair number states $\hat{N}|n\rangle = n|n\rangle$. These operators are useful for representing the cosine and sine functions as

$$\cos(\hat{\theta}_m) = \frac{1}{2}\left(\Sigma^-_m + \Sigma^+_m\right), \tag{5.26a}$$

$$\sin(\hat{\theta}_m) = \frac{i}{2}\left(\Sigma^-_m - \Sigma^+_m\right). \tag{5.26b}$$

Using compound angle formulae the nearest neighbour coupling is then rewritten

as

$$\cos\left(\hat{\theta}_{m+1}-\hat{\theta}_m-\frac{\Phi_{am}}{\varphi_0}\right)=\frac{1}{2}\left(\Sigma^+_m\Sigma^-_{m+1}e^{i\Phi_{am}/\varphi_0}+\Sigma^-_m\Sigma^+_{m+1}e^{-i\Phi_{am}/\varphi_0}\right). \quad (5.27)$$

Similarly the diametric coupling is rewritten as

$$\cos\left(\hat{\theta}_{m+3}-\hat{\theta}_m-\frac{\Phi_{lm}}{\varphi_0}\right)=\frac{1}{2}\left(\Sigma^+_m\Sigma^-_{m+3}e^{i\Phi_{lm}/\varphi_0}+\Sigma^-_m\Sigma^+_{m+3}e^{-i\Phi_{lm}/\varphi_0}\right). \quad (5.28)$$

In order to arrange the current signs for these couplings we simply choose $\Phi_{am}/\varphi_0=\pi$ and $\Phi_{lm}/\varphi_0=4\pi$.

Next we look at the charge coupling. In the limit $C_r/C_a\to 0$ the inverse of the capacitance matrix gives an all to all charge coupling according to

$$\mathbf{C}^{-1}_{mn}\to\frac{1}{6C_r},\qquad T\to\frac{2}{3}E_{Cr}\sum_{m,n=1}^{6}(\hat{N}_m-N_{g,m})(\hat{N}_n-N_{g,n}). \quad (5.29)$$

If the gate charges are tuned to a half integer then we can make the identification $\hat{N}-N_g\sim\frac{1}{2}\boldsymbol{\sigma}^z$ and this coupling will be of the same form as the all-to-all $\sigma^z_m\sigma^z_n$ we examined earlier. In this manner we can use our circuit to engineer a Hamiltonian which is analogous to the simple spin-1/2 model with Cooper pairs now taking the role of the excitations which can now tunnel between sites via Josephson junctions. Our circuit respects the key translation and inversion symmetries we identified earlier however whereas this previous model consisted of two level sites, each site in our circuit has many levels. But there is another set of terms in our circuit Hamiltonian which we have not yet mentioned: the radial Josephson junctions allow Cooper pairs to tunnel back and forth between the nodes of our circuit and ground. This breaks the conservation of excitations which was a key component of our symmetry arguments. Fortunately in the next section we shall see that this does not pose a significant problem.

Our next task is to find some realistic circuit parameters which produce ground and first excited states with the desired symmetries and which have usable energies i.e. they have a gap which can be driven by microwave pulses and they can be

separated from higher states in the spectrum. We start by assuming that all of the junctions in our circuit have a plasma frequency of $\sqrt{8E_JE_C}/h = 10$ GHz. In practise this means that all of the junctions have the same thickness. During fabrication this allows them to all be created simultaneously in a single oxidation step, which will make the task considerably easier. Next we choose $E_{Ja} = 6$ GHz and make a sweep of E_{Cr} and E_{Jl}.

Again we search for a region of parameter space in which the symmetries listed in eqs. 5.2 are met. Since E_{Cr} controls the strength of the charge coupling in the small C_r limit and E_{Jl} controls the strength of the diametric flip-flop coupling, sweeping these parameters is comparable to sweeping ξ and λ in Fig. 5.1.1. We diagonalize the Hamiltonian in eq. 5.23 using the PRIMME eigensolver available in Python [145]. We include 8 charge states on each site in the chain, which is found to be sufficient for calculations to converge. We find a regime in which the desired inversion and translation eigenvalues are obtained. The gap in energy between the ground and first excited states within this regime is portrayed using a colourplot in Fig. 5.2.1(b). The gap is not displayed in the hatched area outside this regime, since the corresponding states are of no interest to us.

We identify a particular set of parameters ($E_{Jr}/h = 1.7$ GHz, $E_{Ja}/h = 6.0$ GHz and $E_{Jl}/h = 30.0$ GHz), marked by the white cross, which will be used in the following to demonstrate our design. At this location the transition frequency of the qubit is $\omega_{01}/2\pi = 704$ MHz and the anharmonicity of transitions to the next excited state is $\omega_{12}/\omega_{01} = 4$, where ω_{12} is the transition frequency between the first and second excited states of the circuit. Given this large anharmonicity we will be able to address our qubit states without the participation of higher levels.

Lastly we mention the total number operator $\mathcal{N}$. We remarked earlier that our Hamiltonian does not conserve excitations, but it is crucial part of our symmetry arguments. Despite this problem we find that our qubit states are approximately eigenstates of $\mathcal{N}$. We find

$$\frac{\langle 0|\mathcal{N}|0\rangle}{\sqrt{\langle 0|\mathcal{N}^2|0\rangle}}, \frac{\langle 1|\mathcal{N}|1\rangle}{\sqrt{\langle 1|\mathcal{N}^2|1\rangle}} > 1 - 10^{-4} \tag{5.30}$$

which indicates that our symmetry arguments should still hold to some level of approximation.

5.3 Wavefunctions

So far we have very limited information about what these states look like. We only know that they obey a few symmetries, i.e. translation and inversion, but have no other clues as to their form. We will understand them better by examining their wavefunctions in the basis of phase eigenstates $\hat{\theta}_m|\theta_m\rangle = \theta_m|\theta_m\rangle$. For our purposes it will also be useful to define the transformed phase states $|\vec{\theta},\vec{N}_g\rangle = e^{i\vec{N}_g\cdot\vec{\theta}}|\vec{\theta}\rangle$, which will allow us to remove background oscillations due to the gate charges. We write the wavefunctions as

$$\Psi_0(\vec{\theta},\vec{N}_g) = \langle\vec{\theta},\vec{N}_g|0\rangle, \tag{5.31a}$$

$$\Psi_1(\vec{\theta},\vec{N}_g) = \langle\vec{\theta},\vec{N}_g|1\rangle. \tag{5.31b}$$

where $\vec{\theta} = (\theta_1,\theta_2,\theta_3,\theta_4,\theta_5,\theta_6)$ and $\vec{N}_g = (N_{g,1},N_{g,2},N_{g,3},N_{g,4},N_{g,5},N_{g,6})$. To see exactly why it is necessary to use the transformed phase states we must understand that the charge states present in the wavefunctions are centered around the gate charges. This can be proven by recognising that the Hamiltonian is invariant under the exchange of all charge states above the gate charge with the charge states below the gate charge i.e. $|\lfloor N_g\rfloor - m\rangle \leftrightarrow |\lfloor N_g\rfloor + m\rangle$. This action can be implemented via the unitary operator

$$\hat{F}(N_g) = \sum_{m=-\infty}^{\infty} |\lfloor N_g\rfloor - m\rangle\langle\lfloor N_g\rfloor + m| \tag{5.32}$$

which acts on the number and tunneling operators according to

$$\hat{F}(N_g)\hat{N}\hat{F}(N_g) = 2\lfloor N_g\rfloor + 1 - \hat{N} \tag{5.33a}$$

$$\hat{F}(N_g)\Sigma^{\pm}\hat{F}(N_g) = \Sigma^{\mp}. \tag{5.33b}$$

Provided that the gate charges are tuned to half integers, this transformation will leave the charge couplings terms of the Hamiltonian unchanged. In addition, if the fluxes controlling the signs of the tunnel couplings are tuned to half or full integers of flux quanta, these terms will also be left unchanged. Hence the overall Hamiltonian and its eigenstates must respect this symmetry.

Next we examine a charge state expressed in the phase basis as

$$|n\rangle = \frac{1}{\sqrt{2\pi}} \int d\theta e^{-in\theta} |\theta\rangle . \tag{5.34}$$

This charge state takes the form of a plane wave oscillating with angular frequency n. Since the charge states contributing to our qubit states are centered on the gate charges, we should expect the the frequencies contributing to the wavefunctions to also be centered on the gate charges. This background frequency is removed in the $|\vec{\theta},\vec{N}_g\rangle$ basis, which produces the potential and wavefunctions plotted in Fig. 5.2.1(c). We represent the potential along a two-dimensional $(x-y)$ cut of the six-dimensional Hilbert space, within which the node phases are given by $\theta_n = nx + y$. To sets of global minima are observed forming two valleys along the lines $y = x \pm \frac{2\pi}{3}$. In Fig. 5.2.1(b) we plot the potential along $y = 0$ along with the wavefunctions of the qubit states. We observe that the wavefunctions are localised in the potential minima. The co-ordinates of the left minimum $\vec{\phi} = (-2\pi/3, -4\pi/3, -6\pi/3, -8\pi/3, -10\pi/3, -12\pi/3)$ correspond to a clockwise current flowing in each azimuthal junction of $I_p = I_{ca}\sin(\pi/3)$ where I_{ca} is the critical current of these junctions, while the current in the junctions of the outer loops are all zero. Similarly, the co-ordinates of the right minimum $\overline{\phi} = (2\pi/3, 4\pi/3, 6\pi/3, 8\pi/3, 10\pi/3, 12\pi/3)$ correspond to an anti-clockwise current of $I_p = I_{ca}\sin(\pi/3)$. We denote the states localised in these minima by $|\circlearrowright\rangle$ and $|\circlearrowleft\rangle$ so that the qubit states are given by $|0\rangle = \frac{1}{\sqrt{2}}(|\circlearrowright\rangle + |\circlearrowleft\rangle)$ and $|1\rangle = \frac{1}{\sqrt{2}}(|\circlearrowright\rangle - |\circlearrowleft\rangle)$.

By looking at the potential and our states in the phase basis it is also possible to see why our states are approximately eigenstates of the the total excitation operator, despite the Hamiltonian not conserving total excitations. To see why, we must

express the Cooper pair number operators in the phase basis as follows:

$$\begin{aligned}\langle\theta, N_g|\hat{N} &= \int d\theta' \langle\theta, N_g|\,\theta'\rangle\langle\theta'|\hat{N} \\ &= e^{-iN_g\theta}\langle\theta|\hat{N} \\ &= -ie^{-iN_g\theta}\partial_\theta\langle\theta| \\ &= N_g - i\partial_\theta\langle\theta, N_g|\,. \end{aligned} \tag{5.35}$$

We can then obtain express the total Cooper pair number operator $\mathcal{N} = \sum_{m=1}^{6}\hat{N}_m$ as

$$\begin{aligned}\langle\vec{\theta}, \vec{N}_g|\mathcal{N} &= \sum_{m=1}^{6}(N_{g,m} - i\partial_{\theta_m}\langle\vec{\theta}, \vec{N}_g|) \\ &= \sum_{m=1}^{6} N_{g,m} - i\partial_y\langle\vec{\theta}(x,y), \vec{N}_g|\,. \end{aligned} \tag{5.36}$$

In other words the total Cooper pair number operator acts like a derivative with respect the y coordinate, with an added offset from the gate charges. Within the valleys formed by the global minima we see that neither the potential nor the wavefunctions vary with respect to y. Hence, within these minima Cooper pairs are approximately conserved, despite the fact that in general the radial junctions allow Cooper pairs to tunnel back and forth from the ground node.

5.4 Coherence properties

We now turn our attention to the coherence properties of our proposed qubit, both at the optimal point and away from it. Sources of decoherence can be divided into two basic types: relaxation due to exchange of energy between the qubit and its environment, and dephasing whereby the energy gap of the qubit may vary stochastically in time causing the experimentalist to lose track of the accumulated phase. In our design we will consider dephasing due to charge and flux noise, and we will consider relaxation via quasiparticle tunneling and dielectric losses.

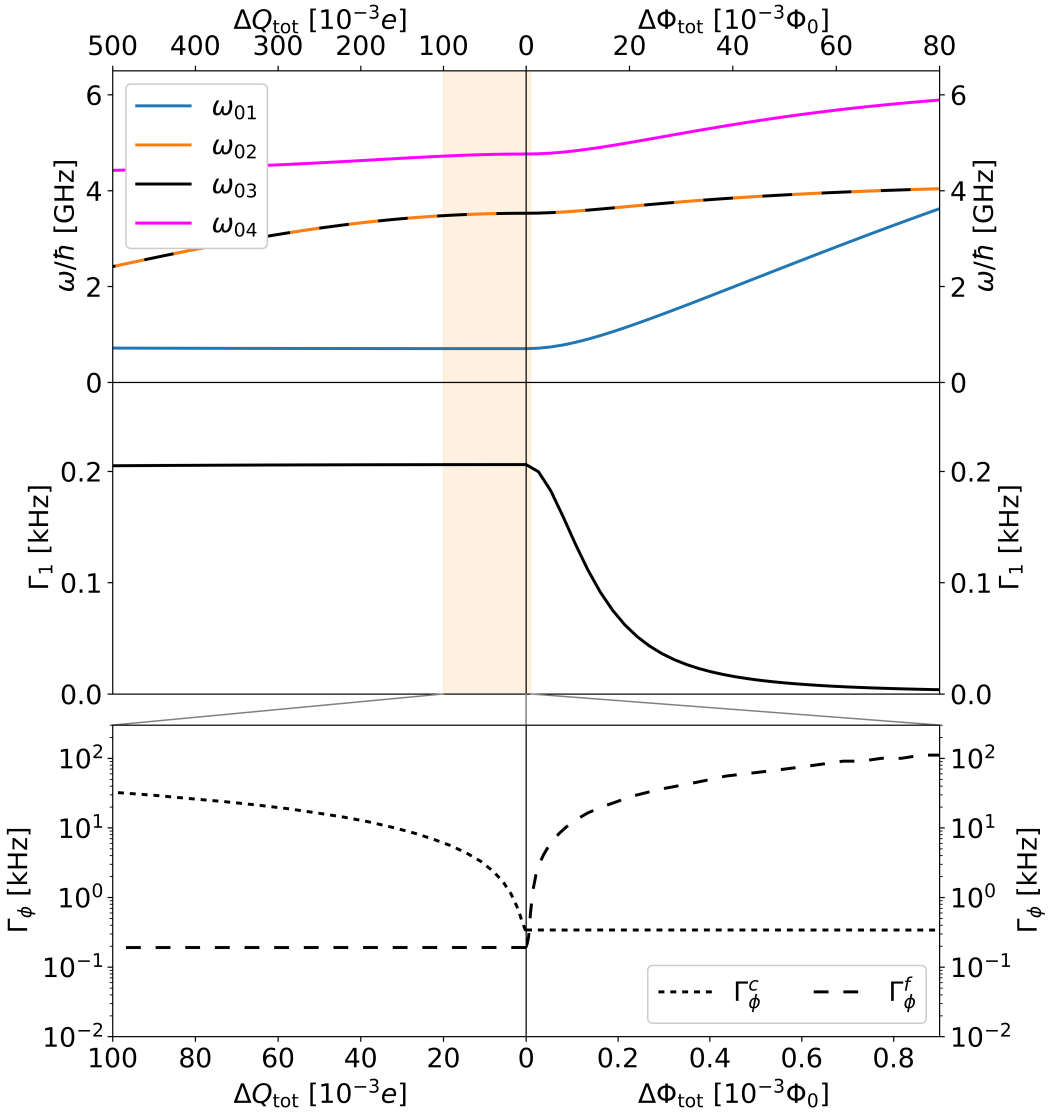

Figure 5.3.1: Decoherence properties of the qubit. Upper: Spectroscopy of the qubit showing the first four transition frequencies vs. the total charge ΔQ_{tot} and flux $\Delta\Phi_{\text{tot}}$ offsets from the optimal point. Middle: Relaxation rate of the qubit due to quasiparticle tunneling. Lower: Pure dephasing rate away from the optimal point due to charge noise (Γ_ϕ^c) or flux noise (Γ_ϕ^f). The spectral density of the both charge and flux noise is assumed to behave as $1/f$ with an IR cutoff of 1 Hz and a UV cutoff of 1 MHz. The amplitudes of the power spectra at 1 Hz are assumed to be $\sqrt{A^c} = 2\times10^{-4}\ e$ for charge noise and $\sqrt{A^f} = 2\times10^{-6}\ \Phi_0$ for flux noise. This charge and flux noise is divided evenly among the nodes and loops of the circuit.

5.4.1 Dephasing

We begin with dephasing. In any realistic design we expect our circuit to undergo both charge noise and flux noise. The microscopic sources of charge noise may include fluctuating charges in the substrate of the circuit or in the oxide layers formed within both the Josephson junctions and on top of the lines of the circuit [146, 147, 148, 149, 150]. Meanwhile flux noise is thought to originate from spin defects [151, 152]. Only spins near the edges of the loops of circuit would contribute to flux noise since the net flux of a dipole far from the edge would tend to zero. Temperature-activated motion of these charge fluctuators and spins is expected to produce noise in the gate charges and external fluxes with a $1/f$ power spectral density (PSD).

We will now introduce the theory which allows us to calculate the dephasing time of the qubit in the presence of such noise [153, 154]. We consider a Hamiltonian H which depends on some time varying set of noisy parameters $\vec{x}(t)$ whose long-time average is zero $\bar{\vec{x}} = 0$. If the PSD of the noise is limited to frequencies below the gaps between the eigenstates of the Hamiltonian then it will be unable to cause transitions. Therefore we can treat the noise adiabatically and consider the occupation probabilities of all eigenstates to be constant. Our qubit is formed by the lowest two eigenstates of $H\big(\vec{x}(t)\big)$, whose splitting frequency is written as

$$\omega_{01}(\vec{x}(t)) = \omega_{01}(0) + \delta\omega_{01}(\vec{x}(t)) \tag{5.37}$$

where $\delta\omega_{01}(\vec{x}(t))$ denotes any fluctuations in the splitting frequency due to the noise. The state of our qubit consists of a superposition of these states and is written as

$$|\psi(t)\rangle = \alpha(t)\,|0\rangle + \beta(t)\,|1\rangle\,. \tag{5.38}$$

In order to study the coherence of the qubit during its evolution we must calculate

the ensemble average state over many experiments. This will be given by

$$\rho(t) = \mathbb{E}[|\psi(t)\rangle \langle\psi(t)|] \tag{5.39}$$

$$= \begin{pmatrix} p_0 & C(t) \\ C^*(t) & p_1 \end{pmatrix} \tag{5.40}$$

where p_0 and p_1 represent the occupation probabilities of states $|0\rangle$ and $|1\rangle$ and $C(t)$ represents the coherence of their superposition. The evolution of this coherence can be written as

$$\begin{aligned} C(t) &= \mathbb{E}[\alpha(t)\beta^*(t)], \\ &= \sqrt{p_0 p_1}\exp(-i\overline{\omega_{01}}t) f_\phi(t). \end{aligned} \tag{5.41}$$

where $f_\phi(t) = \mathbb{E}[\exp(-i\phi(t))]$ and $\phi(t) = \int_0^t \delta\omega_{01}(\vec{x}(\tau))d\tau$. This evolution consists of two principal parts: an oscillation at the average frequency of the qubit multiplied by a term which accounts for the variations in the accumulated phase in each experimental run. The latter term decays over time due to destructive interference between these variations, causing the qubit to decohere. Our task is to calculate $f_\phi(t)$ numerically by taking many samples of the noise from an appropriate PSD, calculating $\phi(t)$ for each sample, and finally taking the ensemble average of the phase. We define the PSD of a component of the noise as

$$S_x(\omega) = \int_{-\infty}^{+\infty} R_x(\tau)\exp(-i\omega\tau)d\tau, \tag{5.42a}$$

$$R_x(\tau) = \mathbb{E}[x(\tau)x(t+\tau)]. \tag{5.42b}$$

We find it useful to write $S(\omega)$ is terms of a normalized PSD as

$$S_x(\omega) = A_x S_0(\omega). \tag{5.43}$$

A sample from the normalized PSD is denoted by $\tilde{x}(t)$ and the corresponding sample from the unnormalized PSD is $x(t) = \sqrt{A}\tilde{x}(t)$. If we have noise on a single

parameter then we can write the frequency variation of the qubit using a Taylor expansion as

$$\begin{aligned}\delta\omega_{01}(t) &= x(t)\partial_x\omega_{01} + \frac{1}{2}x^2(t)\partial_x^2\omega_{01} + \mathcal{O}(x^3(t)) \\ &= \tilde{x}(t)\sqrt{A}\partial_x\omega_{01} + \frac{1}{2}\tilde{x}^2(t)A\partial_x^2\omega_{01} + \mathcal{O}(\tilde{x}^3(t)) \\ &= \tilde{D}_x\tilde{x}(t) + \frac{1}{2}\tilde{D}_{x,x}\tilde{x}^2(t) + \mathcal{O}(\tilde{x}^3(t))\end{aligned} \tag{5.44}$$

in which we use

$$\tilde{D}_x = \sqrt{A}\partial_x\omega_{01} \quad \text{and} \quad \tilde{D}_{x,x} = A\partial_x^2\omega_{01}. \tag{5.45}$$

If we expand to multi-parameter noise then the frequency variation is given by

$$\delta\omega_{01}(t) = \sum_m \tilde{x}_m(t)\tilde{D}_{x_m} + \frac{1}{2}\sum_{m,n}\tilde{D}_{x_m,x_n}\tilde{x}_m(t)\tilde{x}_n(t) + \mathcal{O}(\tilde{x}^3(t)) \tag{5.46}$$

for which we define

$$\tilde{D}_{x_m} = \sqrt{A}\partial_{x_m}\omega_{01} \quad \text{and} \quad \tilde{D}_{x_m,x_n} = A\partial_{x_m}\partial_{x_n}\omega_{01}. \tag{5.47}$$

These derivatives can be calculated by numerically by diagonalizing $H(\vec{x})$ for many samples of $\vec{x}$ and fitting a Taylor expansion to the resulting values of $\omega_{01}(\vec{x})$. We will present the results of these dephasing calculations in section 5.4.3 alongside calculations of the relaxation time.

5.4.2 Relaxation

There are two principal sources of relaxation to examine: dielectric losses due to currents flowing in the oxide layer of the Josephson junctions, and the tunneling of quasiparticles across these junctions. We start by demonstrating that dielectric losses should be negligible, before moving on to quasiparticle tunneling.

The theory describing dielectric losses is based on the quantum fluctuation-dissipation relation and Fermi's golden rule [155]. We expect the voltage across each junction in the circuit to fluctuate with a PSD proportional to $E_C\tan(\delta)$ where E_C is the charging energy of that junction and $\tan(\delta)$ is the loss tangent of the dielec-

tric within the junction. Using Fermi's golden rule we can calculate the transition rate due to these fluctuations [27]. We obtain an order of magnitude estimate for the relaxation rate due to dielectric losses in junction i according to

$$\Gamma_{1,i} \sim E_{C,i} \tan(\delta_i) \max_{j,k}(N_{j,k}) \tag{5.48}$$

where $N_{j,k} = \langle 1|\hat{N}_j|0\rangle \langle 0|\hat{N}_k|1\rangle$. However, due to our symmetry arguments we expect such transition matrix elements to vanish. For our design parameters we calculate $|\langle 0|\hat{N}_j|1\rangle| < 10^{-11}$. Given a typical loss tangent of $\tan(\delta) \sim 10^{-5}$ [27, 156] we therefore expect $\Gamma_{1,i} \lesssim 10^{-17}$ Hz so dielectric losses will not be a significant source of relaxation.

We can now move on to quasiparticle tunneling [157, 158, 159, 155]. Quasiparticles within the circuit act as a bath with which the superconducting states may exchange energy. The energy required for a quasiparticle to tunnel across a junction may be provided by a relaxation of the state of the qubit. The contribution to the relaxation rate of quasiparticle tunneling over a single junction is given by

$$\Gamma_{1,\mathrm{qp}} \approx \frac{4E_J x_{\mathrm{qp}}}{\pi} \sqrt{\frac{2\Delta}{\hbar\omega_{01}}} \left| \langle 1| \sin\left(\frac{\delta\hat{\theta}}{2}\right) |0\rangle \right|^2 \tag{5.49}$$

where E_J is the Josephson energy of the junction, Δ is the superconducting gap, $\delta\hat{\theta}$ is the phase difference over the junction and x_{qp} is the quasiparticle density. The full relaxation rate is obtained by summing the relaxation rates for all of the junctions in the circuit.

5.4.3 Coherence results

Now that we have the tools to calculate both the dephasing and relaxation rates of our qubit we can plot how these quantities change as the fluxes and gate charges of the circuit are varied. In Fig. 5.3.1 we display how the energies of the four lowest excited states of the Hamiltonian change as we vary the total gate charge and flux offsets: $\Delta Q_{\mathrm{tot}} = 2e\sum_{m=1}^{6} N_{g,n}$ and $\Delta\Phi_{\mathrm{tot}} = \sum_{m=1}^{6} \Phi_{I,m} + \sum_{m=1}^{3} \Phi_{O,m}$. Varying the gate charges does not have a significant effect on the transition frequency of

our qubit, but varying the flux away from the optimal point generates a magnetic dipole where one current state ($|\circlearrowleft\rangle$ or $|\circlearrowright\rangle$) becomes more favourable and therefore increases the transition frequency by $\sim I_p \Delta\Phi_{\text{tot}}$. This behaviour is similar to what is usually observed with flux qubits but the sensitivity of the transition frequency to changes in the flux is significantly reduced since the persistent current flowing in our circuit $I_p = 10$ nA is two orders of magnitude smaller than the typical current flowing in a flux qubit. Eventually the transition frequency will increase until the first and second excited states cross at $\omega_{01}/2\pi \approx 4$ GHz.

The rate of relaxation due to quasiparticle tunneling is plotted in the middle panel of Fig. 5.3.1. These result were calculated using a quasiparticle density of $x_{\text{qp}} = 5 \times 10^{-9}$ and a superconducting gap of $\Delta = 200$ μeV for aluminium [160]. At the optimal point we find a relaxation rate of $\Gamma_1 = 0.2$ kHz which corresponds to a relaxation time of $T_1 = 5$ ms. The relaxation rate is insensitive to charge detuning, but it decreases when the flux is detuned from the optimal point.

Finally we examine dephasing. Flux and charge noise are generated with a $1/f$ spectrum i.e. with a PSD of the form

$$S_0(\omega) = \frac{1}{|\omega|}. \tag{5.50}$$

For the charge noise we choose an overall power of $A_c = (2 \times 10^{-4} e)^2$ which we divide among the six gate charges so that each gate charge has a PSD of

$$S_{2eN_{g,m}}(\omega) = \frac{A_c}{6} S_0(\omega). \tag{5.51}$$

For this spectrum we choose an infrared cutoff of $\omega_{\text{IR}}/2\pi = 1$ Hz and an ultraviolet cutoff of $\omega_{\text{UV}}/2\pi = 1$ MHz. Similarly for flux noise we choose an overall power of $\sqrt{A_f} = 2 \times 10^{-6} \Phi_0$ which is divided among the 9 loops of the circuit such that we have

$$S_{\Phi_{I/O,m}}(\omega) = \frac{A_f}{9} S_0(\omega). \tag{5.52}$$

We use these power spectra to produce the dephasing rates plotted in the lower panel of Fig. 5.3.1. We plot the rate of dephasing up to second order in both charge and flux noise. At the optimal point these values give pure dephasing times of $T_\phi^c = 2.9$ ms and $T_\phi^f = 5.2$ ms. When the flux is detuned from the optimal point the qubit becomes vulnerable to flux noise, while when the gate charges are detuned from the optimal point the qubit becomes vulnerable to charge noise.

5.5 Operating the qubit

These coherence times are promising, but conversely they also make it challenging to communicate with the qubit. Typically, the better protected a qubit is from its environment, the harder it is to control, initialize and read its state. We would like to perform these tasks using a circuit-QED architecture and thus coupling our qubit to a microwave resonator is key a requirement. In the next section we will outline a design to implement this coupling by galvanically connecting a resonator to one of the loops of the circuit, which allow some ability to control and read the state of the qubit.

But we must also consider initialization. Initialization is particularly challenging given the small transition frequency of the qubit, which is only $\omega_{01}/2\pi = 704$ MHz. At the base temperature of a dilution refrigerator, i.e. around 20 mK, we expect the thermal state of the qubit to be highly mixed. In order to create a pure ground state we intend to use the flux line to detune the qubit from its optimal point and increase the transition frequency. However, as we can see from Fig. 5.3.1 this will also lead to a suppression of the relaxation rate to such a low level as to be impractical for experimental purposes.

But there is a solution. We could use the resonator to enhance the speed of intialization via the Purcell effect [161]. If we tune the qubit to the frequency of the resonator then the two systems hybridize and the excited state of the qubit decays via the resonator at a highly accelerated rate. Once this operation has been completed we can adiabatically tune the flux back to the optimal point for operation. The details of this procedure and the resonator coupling will be explained below.

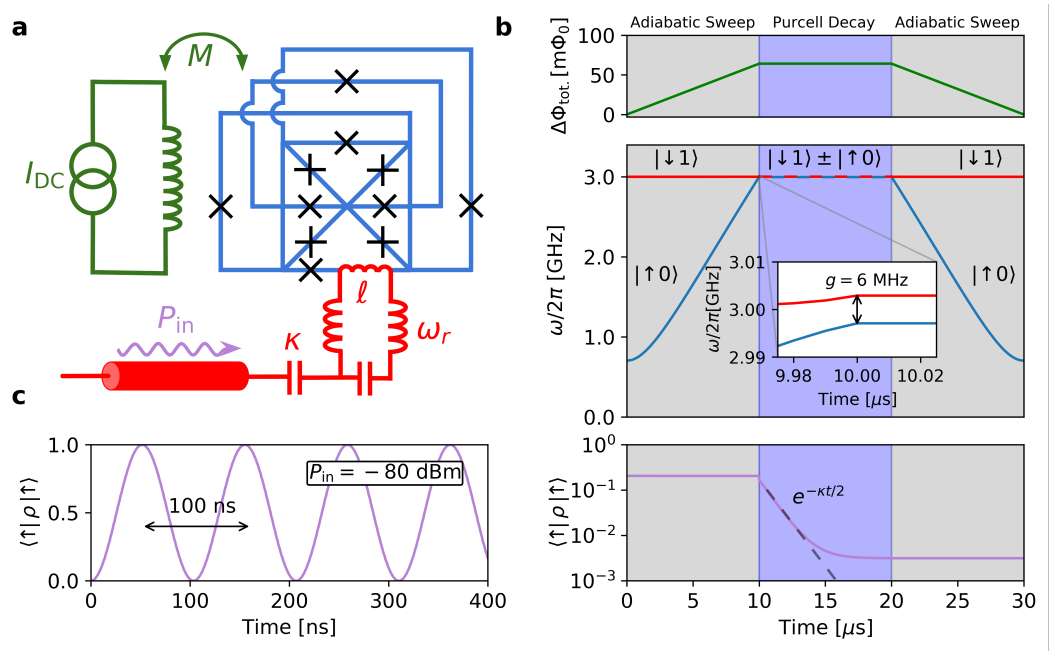

Figure 5.5.1: Operating the qubit. (a) Circuit diagram showing a mode of operation of the qubit. A resonator of frequency $\omega_r/2\pi = 3$ GHz and quality factor $Q = \omega_r/\kappa = 10000$ is galvanically connected to the qubit via a small inductance $l = 40$ pH. The resulting strength of the coupling between the resonator and the qubit is $g \approx 11$MHz. In addition the qubit can be biased by a DC flux line, which is used to detune the flux threading the qubit from the optimal point for the purposes of initialization and readout. (b) Control sequence used to initialize the qubit. Due to its relatively small transition frequency the excited state of the qubit in thermal equilibrium (25 mK) is significantly occupied. In this sequence we use the flux line to adiabatically increase the qubit transition frequency over a period of 10 μs and bring it into resonance with the microwave resonator. At this point the qubit hybridizes with the resonator and relaxes by Purcell decay to the new thermal state at a rate $\kappa/2$. This thermal state is much closer to a pure ground state due to the larger frequency of the resonator. The flux can then be adiabatically tuned back to the optimal point. (c) Simulation of Rabi oscillations with a period of 100 ns which can be produced at the optimal point by driving the resonator at the qubit transition frequency with a power of $P_{in} = -80$ dBm.

5.5.1 Engineering a coupling

In order to obtain a ground state with sufficient purity we need to engineer a resonator with a frequency far above the base fridge temperature. We aim for a frequency of 3 GHz. In the lumped element approximation this frequency is given by $\omega = 1/\sqrt{LC}$, where L and C are the inductance and capacitance of the resonator respectively. We take a typical characteristic impedance of $Z = \sqrt{L/C} \approx 30\ \Omega$ from

which the capacitance and inductance are then given by:

$$C = \frac{1}{\omega Z} = 1.8 \text{ pF} \tag{5.53a}$$

$$L = \frac{Z}{\omega} = 1.6 \text{ nH}. \tag{5.53b}$$

We couple to the qubit by a galvanic connection. A length of wire leading between azimuthal Josephson jundctions is shared by both the resonator and the qubit as illustrated in Fig. 5.5.1(a). We can boost the strength of the coupling by increasing the inductance of this wire. This can be achieved either by lengthening it or by constricting its width, which increases its kinetic inductance. The kinetic inductance of the wire is given by

$$l = \frac{\hbar R}{\pi \Delta} \tag{5.54}$$

where R is its resistance and Δ is the superconducting gap, which is measured to be around 200 μeV in aluminium [160]. The resistance can be calculated according to

$$R = \frac{\rho l}{S} = \frac{\rho l}{aw} \tag{5.55}$$

where ρ is the normal resistivity, l is it's length, S is it's cross-sectional area, w is it's width and a is it's thickness. We choose the radius of our qubit to be 2 μm and the shared wire to also be of length 2 μm. The width of the wire is 50 nm and it's thickness is 24 nm. The resistivity of aluminium is 240 nΩm, which gives a resistance of 40 Ω and we therefore find our constricted wire should have a kinetic inductance of $l = 40$ pH.

The potential energy of the circuit is altered by the addition of this constriction. We now have a new node in the circuit, whose phase we denote by $\hat{\theta}_l$. The phase difference over the constriction can then be written as $\hat{\delta} = \hat{\theta}_l - \hat{\theta}_1$. This phase difference will alter the potential energy of the 1st Josephson junction. Combined with the potential energy of this constriction the new terms in the Hamiltonian take

the form

$$V_{l-1} = \frac{\varphi_0^2 \hat{\delta}^2}{2l} - E_{Ja} \cos\left(\hat{\theta}_2 - \hat{\theta}_1 - \hat{\delta} - \frac{\Phi_{a1}}{\varphi_0}\right). \tag{5.56}$$

By expanding the cosine we find

$$\begin{aligned} V_{l-1} &= \frac{\varphi_0^2 \hat{\delta}^2}{2l} - E_{Ja} \cos\left(\hat{\theta}_2 - \hat{\theta}_1 - \frac{\Phi_{\mathrm{a1}}}{\varphi_0}\right) \cos\left(\hat{\delta}\right) \\ &\quad + E_{Ja} \sin\left(\hat{\theta}_2 - \hat{\theta}_1 - \frac{\Phi_{\mathrm{a1}}}{\varphi_0}\right) \sin\left(\hat{\delta}\right) \\ &= \frac{\varphi_0^2 \hat{\delta}^2}{2l} - E_{Ja} \cos\left(\hat{\theta}_2 - \hat{\theta}_1 - \frac{\Phi_{\mathrm{a1}}}{\varphi_0}\right) \cos\left(\hat{\delta}\right) + \varphi_0 \hat{I}_a \sin\left(\hat{\delta}\right) \end{aligned} \tag{5.57}$$

in which $\hat{I}_a$ is the current flowing in the junction, given by

$$\hat{I}_a = \frac{E_{Ja}}{\varphi_0} \sin\left(\hat{\theta}_2 - \hat{\theta}_1 - \frac{\Phi_{\mathrm{a1}}}{\varphi_0}\right). \tag{5.58}$$

Next we can relate $\hat{\delta}$ to the current flowing in the constriction according to

$$\varphi_0 \hat{\delta} = l \hat{I}_l \tag{5.59}$$

where the constriction current $\hat{I}_l = \hat{I}_a + \hat{I}_r$ is equal to the sum of the junction current and the the current in the resonator. Provided l is sufficiently small we may say that $\hat{\delta}$ is also small. Then we can make the approximation $\sin(\hat{\delta}) = \hat{\delta}$ and rewrite the constriction current to give

$$V_{l-1} = \frac{\varphi_0^2 \hat{\delta}^2}{2l} - E_{Ja} \cos\left(\hat{\theta}_2 - \hat{\theta}_1 - \frac{\Phi_{\mathrm{a1}}}{\varphi_0}\right) \cos\left(\hat{\delta}\right) + l \hat{I}_a (\hat{I}_a + \hat{I}_r). \tag{5.60}$$

Thus we see that there is a coupling between our qubit and the resonator of the form

$$H_{\mathrm{coupling}} = l \hat{I}_a \hat{I}_r. \tag{5.61}$$

The current in the resonator can be expressed as

$$\hat{I}_r = I_{\mathrm{ZPF}}(a + a^\dagger) \tag{5.62}$$

where the zero point fluctuation is given by $I_{\mathrm{ZPF}} = \omega_0 \sqrt{\frac{\hbar}{2Z_0}}$. For a resonator of frequency $\omega_0/2\pi = 3$ GHz and impedance $Z_0 = 30\ \Omega$ we find $I_{\mathrm{ZPF}} = 25$ nA. We write the junction current operator in a truncated basis consisting of our qubit states as

$$\hat{I}_a = \frac{1}{2}(\langle 0|\hat{I}_a|0\rangle - \langle 1|\hat{I}_a|1\rangle)\sigma_z + \langle 0|\hat{I}_a|1\rangle\,\sigma_x + \ldots \tag{5.63}$$

where we have chosen the phases of our states such that $\langle 0|\hat{I}_a|1\rangle$ is real. If it is valid to apply the rotating wave approximation then we will at last arrive a Jaynes-Cummings coupling of the form

$$H_{\mathrm{coupling}} = lI_{\mathrm{ZPF}}\langle 0|\hat{I}_a|1\rangle\,(\sigma^+ a + \sigma^- a^\dagger) \tag{5.64}$$

with a coupling strength of $g = lI_{\mathrm{ZPF}}\langle 0|\hat{I}_a|1\rangle$. At the optimal point we find $\langle 0|\hat{I}_a|1\rangle \approx 7.5$ nA. This gives us a coupling of $g/2\pi = 11$ MHz.

5.5.2 Initialization

Now that we have established how to couple our qubit to a microwave resonator we can consider initialization. As stated above, this procedure can be carried out via the Purcell effect, i.e. tuning our qubit to the frequency of the microwave resonator and using the cavity decay to accelerate the process of thermalization, before tuning the qubit back to the optimal point.

The variations in the flux must be carried out adiabatically in both directions. During the initial sweep we must avoid transitions to higher states which will not relax via the resonator, whereas on the return sweep we must preserve as occupation probability in the ground state as possible. However, if the flux sweeps are carried out too slowly then we will lose the advantage of using the Purcell effect to accelerate initialization. We must balance these two conflicting considerations in order to

obtain the optimum initialization protocol.

In order to demonstrate the feasibility of this initialization procedure we wish to carry out simulations using the framework of the Lindblad master equation. However this is challenging because of the large size of the Hilbert space used to describe the circuit. If each node in the circuit is represented by Hilbert space consisting of 10 charge states then the overall Hilbert space of the circuit will contain 10^{10} states. The task of evolving such a large state over the entire initialization procedure is beyond our means. Fortunately there is an alternative. Only the lowest eigenstates of the Hamiltonian should contribute to this state and we can greatly accelerate our simulation by truncating the basis. But this introduces a new complication: these eigenstates will vary with the flux. How can we perform a simulation in a time-dependent basis? We will now describe the formalism for such a situation.

Consider a Hamiltonian $H(x)$ which depends on a time dependent parameter $x(t)$. Each eigenstate $\psi_n(x)$ corresponds to an eigenvalue $\omega_n(x)$, both of which are also dependent on x. The eigenvalue equation is written as

$$H(x)\psi_n(x) = \omega_n(x)\psi_n(x). \tag{5.65}$$

Now consider a state $\Psi(t)$ which evolves in time according to the Schrödinger equation

$$i\partial_t\Psi(t) = H\big(x(t)\big)\Psi(t). \tag{5.66}$$

We define the unitary operator which will transform our frame to the x-dependent eigenbasis of the Hamiltonian:

$$U(x) = \Big(\psi_0(x), \psi_1(x), ...\Big). \tag{5.67}$$

In this basis the state vector is described by

$$\chi(t) = U^\dagger\big(x(t)\big)\Psi(t) \tag{5.68}$$

$$= \begin{pmatrix} \psi_0^\dagger\big(x(t)\big)\Psi(t) \\ \psi_1^\dagger\big(x(t)\big)\Psi(t) \\ \vdots \end{pmatrix} \tag{5.69}$$

The time evolution of $\chi(t)$ is described in turn by

$$i\partial_t\chi(t) = H_{\text{mov}}(x,\partial_t x)\chi(t) \tag{5.70a}$$

where $H_{\text{mov}}(x,\partial_t x)$ is an appropriate Hamiltonian. This Hamiltonian is not simply the original Hamiltonian H transformed to a new static frame, but also accounts for the change in the state vector χ due to the continually changing eigenbasis. This is why H_{mov} depends on $\partial_t x$ as well as x. The new Hamiltonian is given by

$$H_{\text{mov}}(x,\partial_t x) = U^\dagger(x)H(x)U(x) + i\partial_t x\,\partial_x U^\dagger(x)\,U(x). \tag{5.71}$$

The first term is simply a matrix of instantaneous eigenfrequencies

$$U^\dagger(x)H(x)U(x) = \begin{pmatrix} \omega_0(x) & 0 & \dots \\ 0 & \omega_1(x) & \dots \\ \vdots & \vdots & \ddots \end{pmatrix} \tag{5.72}$$

and the second term describes changes due to the time-dependent basis. This second term can be calculated using first order perturbation theory. Consider a small change in the Hamiltonian due to a change in the parameter δx

$$H(x+\delta x) = H(x) + \delta x H'. \tag{5.73}$$

In non-degenerate first order perturbation theory the changes in the eigenstates are

given by

$$\psi_m(x+\delta x) = \psi_m(x) + \delta x \sum_{k\neq m} \frac{\psi_k^\dagger(x) H' \psi_m(x)}{\omega_m(x) - \omega_k(x)} \psi_k(x) + \mathcal{O}(\delta x^2). \tag{5.74}$$

From the above we see that the first derivatives of the states are given by

$$\partial_x \psi_m(x) = \sum_{k\neq m} \frac{\psi_k^\dagger(x) H' \psi_m(x)}{\omega_m(x) - \omega_k(x)} \psi_k(x). \tag{5.75}$$

By writing the above we have implicitly fixed our gauge according to $\partial_x \psi_m^\dagger \psi_m = 0$. Now we can rewrite the second term using

$$\begin{aligned} \left(\partial_x U^\dagger(x) U(x)\right)_{mn} &= \partial_x \psi_m^\dagger(x)\, \psi_n(x) \\ &= \partial_x \psi_m^\dagger(x)\, \psi_n(x) \\ &= \frac{\psi_m^\dagger(x) H' \psi_n(x)}{\omega_m(x) - \omega_n(x)} (1 - \delta_{mn}). \end{aligned} \tag{5.76}$$

We now have most of the components necessary to write down the Hamiltonian describing the evolution of our state in the time-dependent basis, but there is a final problem. What are the eigenfrequencies $\omega_m(x)$ and matrix elements $\psi_m^\dagger(x) H' \psi_n(x)$? We certainly don't want to recalculate these quantities at every new value of x throughout evolution, since this would require the very time consuming process of calculating eigenvalues and eigenvectors of the $\sim 10^{10} \times 10^{10}$ Hamiltonian which describes the circuit. The alternative is to sample these quantities over a range of values of x and interpolate between them during evolution.

We can now write down the Hamiltonian which describes the evolution of the state during the initialization protocol:

$$\begin{aligned} H_{\mathrm{JC,mov}}(\Delta\Phi_{\mathrm{tot}}) =& U^\dagger(\Delta\Phi_{\mathrm{tot}}) H(\Delta\Phi_{\mathrm{tot}}) U(\Delta\Phi_{\mathrm{tot}}) + \omega_r a^\dagger a \\ &+ i\partial_t \Delta\Phi_{\mathrm{tot}}\, \partial_{\Delta\Phi_{\mathrm{tot}}} U^\dagger(\Delta\Phi_{\mathrm{tot}})\, U(\Delta\Phi_{\mathrm{tot}}) \\ &+ g(\Delta\Phi_{\mathrm{tot}})(a\,|1\rangle\langle 0| + a^\dagger\,|0\rangle\langle 1|). \end{aligned} \tag{5.77}$$

In the above $H(\Delta\Phi_{\text{tot}})$ is equivalent to the original circuit Hamiltonian (eq. 5.23) with $\Delta\Phi_{\text{tot}}$ describing the detuning of the flux from the optimal point. The loop fluxes are given by

$$\Phi_{O/I,m} = \pi\varphi_0 + \frac{\Delta\Phi_{\text{tot}}}{9}. \tag{5.78}$$

The transformation $U(\Delta\Phi_{\text{tot}})$ acts solely to diagonalize the circuit Hamiltonian and leaves the resonator unaffected. As described above the second line represents the change in the state vector of the circuit due to changes in the basis and the last line is the Jaynes-Cummings coupling between the qubit states of the circuit ($|\downarrow\rangle$ and $|\uparrow\rangle$) and the resonator. The strength of the coupling $g(\Delta\Phi_{\text{tot}})$ is also dependent on the flux since it is proportional to the matrix element of an azimuthal Josephson current between two flux dependent eigenstates i.e.

$$g(\Delta\Phi_{\text{tot}}) = lI_{\text{ZPF}} \langle 0, \Delta\Phi_{\text{tot}} | \hat{I}_a | 1, \Delta\Phi_{\text{tot}} \rangle . \tag{5.79}$$

Finally we can write down the master equation which includes the relaxation of the cavity, making a simulation of Purcell initialization possible. This is given by

$$\partial_t \rho = -i[H_{\text{JC,mov}}(\Delta\Phi_{\text{tot}}), \rho] + \kappa(1+n)D[a]\rho + \kappa n D[a^\dagger]\rho \tag{5.80}$$

where dissipation is described by $D[O]\rho = O\rho O^\dagger - \frac{1}{2}(O^\dagger O\rho + \rho O^\dagger O)$. The Lindblad operators a and $a^\dagger$ cause thermal relaxation and excitation of the cavity at a rate κ, leading to a cavity steady state containing n photons.

By increasing the flux offset to $\Delta\Phi_{\text{tot}}/\varphi_0 = 0.606$ over 10 μs we can tune the qubit to the resonator frequency at $\omega_r/2\pi = 3$ GHz. Given a quality factor of $Q = 10{,}000$ we have a cavity relaxation rate of $\kappa/2\pi = 0.3$ MHz. Once the qubit and resonator have hybridized this allows the system to decay towards a thermal state with a time constant $\tau = 2/\kappa = 1.1$ μs. At temperature of 25 mK we use the Bose distribution to calculate a thermal occupation of $n = 0.003$ photons. After a resting time of 10 μs the system has essentially reached its steady state, after which

the flux can be returned to the optimal point over another 10 μs to give a final initialization fidelity of 99.7%.

5.5.3 Readout

We note that this process of adiabatically varying the flux through the circuit can also be useful during readout. One of the most widely used techniques for measuring the state of a superconducting qubit is known as dispersive readout, in which the state of the qubit is inferred from shifts in the resonator frequency [1, 162]. This technique requires the qubit to be coupled to the resonator via a Jaynes-Cummings type interaction in the dispersive regime, defined by $g/|\omega_{01}-\omega_r| \ll 1$. Such an interaction causes the resonator frequency to increase or decrease by $\chi = g^2/|\omega_{01}-\omega_r|$ depending on the state of the qubit according to the dispersive Hamiltonian

$$H = \left(\omega_r + \frac{g^2}{\omega_{01}-\omega_r}\sigma^z\right)a^\dagger a + \left(\frac{1}{2}\omega_{01} + \frac{g^2}{\omega_{01}-\omega_r}\right)\sigma^z. \tag{5.81}$$

If these shifts are larger than the linewidth of the cavity (i.e. $\chi \gtrsim \kappa$) then they can be used as a signature to detect the state of the qubit.

For our design at the optimal point we calculate $\chi(\Delta\Phi_{\text{tot}}=0)/2\pi = 8.9$ kHz, which is clearly far smaller than the linewidth of $\kappa/2\pi = 0.3$ MHz. The solution to this problem is to perform readout away from the optimal point. Instead we can tune the qubit close to the resonator, but still with sufficient detuning that we are in the dispersive regime. When the qubit is close to the resonator frequency we calculate a coupling strength of $g/2\pi \approx 2$ MHz. If we choose the resonator shift to be equal to the linewidth $\chi = \kappa$ then we calculate a detuning of $|\omega_{01}-\omega_r|/2\pi = 13.3$ MHz. From this we calculate $g/|\omega_{01}-\omega_r| = 0.15$, which demonstrates that we are in the dispersive regime and the above Hamiltonian is a good approximation.

5.5.4 Control

Finally we can mention control of the qubit. At the optimal point we expect to be able to carry out single qubit gates by driving Rabi oscillations. It is well known that in the Jaynes-Cummings model this can be achieved by applying a drive to the

resonator at the frequency of the qubit. Here we will simply demonstrate that the power required to drive such oscillations is realistic. These oscillations must occur on a timescale short enough that many gates can be performed within the coherence time of the qubit.

The Rabi frequency typically increases in proportion to the drive power applied to the resonator, but this in turn is limited by the ability of the dilution refrigerator to remove heat dissipated by the attenuators which protect the qubit against thermal noise from higher temperature stages both within and outside the fridge. Therefore there is a tradeoff between the maximum attainable Rabi frequency and the thermal noise n.

We simulate Rabi oscillations using the following Hamiltonian

$$H = \sum_n \omega_n |n\rangle\langle n| + \omega_r a^\dagger a + l\hat{I} I_{\mathrm{ZPF}}(a + a^\dagger) + \varepsilon \cos(\omega_d t)(a + a^\dagger) \tag{5.82}$$

in which the eigenfrequencies and eigenstates of the qubit Hamiltonian are represented by ω_n and $|n\rangle$. This Hamiltonian also includes the resonator and the coupling described above, as well as the resonator drive at amplitude ε and frequency ω_d. Our simulation also includes the Lindblad operators:

$$a\sqrt{\kappa(1+n)}, \qquad a^\dagger\sqrt{\kappa n} \quad \text{and} \quad \sqrt{\gamma}|0\rangle\langle 1|\,. \tag{5.83}$$

The input power applied to the resonator is given by $P_{in}(t) = \hbar\omega_d\varepsilon^2(t)/\kappa$ [29]. With a drive power of -80 dBm we are able to drive Rabi oscillations with a time period of 100 ns.

5.6 Conclusion

In this chapter we have introduced a new qubit design based on a superconducting circuit consisting of a ring of Cooper Pair Boxes arranged in a ring which couple to each other via both nearest neighbour and 3rd nearest neighbour couplings. The symmetries inherent to this design produce promising coherence times in when we consider both dephasing due to charge and flux noise and relaxation via quasipar-

ticle tunneling and dielectric losses. Furthermore we have shown that this circuit can be coupled to a microwave resonator in a cQED architecture. This opens up the possibility of the control and readout using the standard techniques of this field.

Thus far, all of this work has been purely theoretical. Future work should of course focus on the fabrication of this design and the demonstration of its properties. Yet there is still room for further theory work. So far we have not considered multi qubit gates, which are essential to the operating of any quantum computer. In many cQED based techniques for this procedure have been developed and it will become increasingly important to assess which is most promising for our design. Furthermore we have only considered uncorrelated noise in this chapter. In reality this cannot be assumed [163] and we must consider what effects any correlations will have on our predictions of the coherence time. Finally we may wish to consider modifications to our design such as exploring longer chain lengths to see if they lead to improved performance.

Contributions

This project was carried out by Paul Brookes under the supervision of Michael Stern, Eran Ginossar, Marzena Szymanska and Eytan Grosfeld.

Bibliography

[1] A Blais. A. blais, r.-s. huang, a. wallraff, sm girvin, and rj schoelkopf, phys. rev. a 69, 062320 (2004). *Phys. Rev. A*, 69:062320, 2004.

[2] Frank Arute, Kunal Arya, Ryan Babbush, Dave Bacon, Joseph C Bardin, Rami Barends, Rupak Biswas, Sergio Boixo, Fernando GSL Brandao, David A Buell, et al. Quantum supremacy using a programmable superconducting processor. *Nature*, 574(7779):505–510, 2019.

[3] Jens Koch, Terri M Yu, Jay Gambetta, Andrew A Houck, D I Schuster, J Majer, Alexandre Blais, Michel H Devoret, Steven M Girvin, and Robert J Schoelkopf. Charge-insensitive qubit design derived from the cooper pair box. *Physical Review A*, 76(4):042319, 2007.

[4] Peter W Shor. Fault-tolerant quantum computation. In *Proceedings of 37th Conference on Foundations of Computer Science*, pages 56–65. IEEE, 1996.

[5] Emanuel Knill and Raymond Laflamme. Theory of quantum error-correcting codes. *Physical Review A*, 55(2):900, 1997.

[6] Charles H Bennett, David P DiVincenzo, John A Smolin, and William K Wootters. Mixed-state entanglement and quantum error correction. *Physical Review A*, 54(5):3824, 1996.

[7] John Preskill. Quantum computing in the nisq era and beyond. *Quantum*, 2:79, 2018.

[8] Philip Krantz, Morten Kjaergaard, Fei Yan, Terry P Orlando, Simon Gustavsson, and William D Oliver. A quantum engineer's guide to superconducting qubits. *Applied Physics Reviews*, 6(2):021318, 2019.

[9] Morten Kjaergaard, Mollie E Schwartz, Jochen Braumüller, Philip Krantz, Joel I-J Wang, Simon Gustavsson, and William D Oliver. Superconducting qubits: Current state of play. *Annual Review of Condensed Matter Physics*, 11:369–395, 2020.

[10] Louis N Hand and Janet D Finch. *Analytical mechanics*. Cambridge University Press, 1998.

[11] Paul Adrien Maurice Dirac. The fundamental equations of quantum mechanics. *Proceedings of the Royal Society of London. Series A, Containing Papers of a Mathematical and Physical Character*, 109(752):642–653, 1925.

[12] Paul Adrien Maurice Dirac. *The principles of quantum mechanics*. Number 27. Oxford university press, 1981.

[13] Bernard Yurke and John S Denker. Quantum network theory. *Physical Review A*, 29(3):1419, 1984.

[14] Michel H Devoret et al. Quantum fluctuations in electrical circuits. *Les Houches, Session LXIII*, 7(8), 1995.

[15] Guido Burkard, Roger H Koch, and David P DiVincenzo. Multilevel quantum description of decoherence in superconducting qubits. *Physical Review B*, 69(6):064503, 2004.

[16] Brian David Josephson. Possible new effects in superconductive tunnelling. *Physics letters*, 1(7):251–253, 1962.

[17] BRIAN D Josephson. The discovery of tunnelling supercurrents. *Reviews of Modern Physics*, 46(2):251, 1974.

[18] Yasunobu Nakamura, Yu A Pashkin, and Jaw Shen Tsai. Coherent control of macroscopic quantum states in a single-cooper-pair box. *nature*, 398(6730):786–788, 1999.

[19] Vincent Bouchiat, D Vion, Ph Joyez, D Esteve, and MH Devoret. Quantum coherence with a single cooper pair. *Physica Scripta*, 1998(T76):165, 1998.

[20] Yuriy Makhlin, Gerd Schön, and Alexander Shnirman. Quantum-state engineering with josephson-junction devices. *Reviews of modern physics*, 73(2):357, 2001.

[21] Felix Bloch. Generalized theory of relaxation. *Physical Review*, 105(4):1206, 1957.

[22] Alfred G Redfield. On the theory of relaxation processes. *IBM Journal of Research and Development*, 1(1):19–31, 1957.

[23] JE Mooij, TP Orlando, L Levitov, Lin Tian, Caspar H Van der Wal, and Seth Lloyd. Josephson persistent-current qubit. *Science*, 285(5430):1036–1039, 1999.

[24] TP Orlando, JE Mooij, Lin Tian, Caspar H Van Der Wal, LS Levitov, Seth Lloyd, and JJ Mazo. Superconducting persistent-current qubit. *Physical Review B*, 60(22):15398, 1999.

[25] Vladimir E Manucharyan, Jens Koch, Leonid I Glazman, and Michel H Devoret. Fluxonium: Single cooper-pair circuit free of charge offsets. *Science*, 326(5949):113–116, 2009.

[26] Long B Nguyen, Yen-Hsiang Lin, Aaron Somoroff, Raymond Mencia, Nicholas Grabon, and Vladimir E Manucharyan. High-coherence fluxonium qubit. *Physical Review X*, 9(4):041041, 2019.

[27] Ioan M Pop, Kurtis Geerlings, Gianluigi Catelani, Robert J Schoelkopf, Leonid I Glazman, and Michel H Devoret. Coherent suppression of elec-

tromagnetic dissipation due to superconducting quasiparticles. *Nature*, 508(7496):369–372, 2014.

[28] Aaron Somoroff, Quentin Ficheux, Raymond A Mencia, Haonan Xiong, Roman V Kuzmin, and Vladimir E Manucharyan. Millisecond coherence in a superconducting qubit. *arXiv preprint arXiv:2103.08578*, 2021.

[29] Agustin Palacios-Laloy. *Superconducting qubit in a resonator: test of the Legget-Garg inequality and single-shot readout*. PhD thesis, 2010.

[30] Andreas Wallraff, David I Schuster, Alexandre Blais, Luigi Frunzio, R-S Huang, Johannes Majer, Sameer Kumar, Steven M Girvin, and Robert J Schoelkopf. Strong coupling of a single photon to a superconducting qubit using circuit quantum electrodynamics. *Nature*, 431(7005):162, 2004.

[31] Edwin T Jaynes and Frederick W Cummings. Comparison of quantum and semiclassical radiation theories with application to the beam maser. *Proceedings of the IEEE*, 51(1):89–109, 1963.

[32] Bruce W Shore and Peter L Knight. The jaynes-cummings model. *Journal of Modern Optics*, 40(7):1195–1238, 1993.

[33] A. Blais, R.-S. Huang, A. Wallraff, S. M. Girvin, and R. J. Schoelkopf. Cavity quantum electrodynamics for superconducting electrical circuits: An architecture for quantum computation. *Phys. Rev. A*, 69(62320), 2004.

[34] A Wallraff, DI Schuster, A Blais, L Frunzio, J Majer, MH Devoret, SM Girvin, and RJ Schoelkopf. Approaching unit visibility for control of a superconducting qubit with dispersive readout. *Physical review letters*, 95(6):060501, 2005.

[35] V DeGiorgio and Marlan O Scully. Analogy between the laser threshold region and a second-order phase transition. *Physical Review A*, 2(4):1170, 1970.

[36] R Graham and H Haken. Laserlight—first example of a second-order phase transition far away from thermal equilibrium. *Zeitschrift für Physik*, 237(1):31–46, 1970.

[37] S Grossmann and PH Richter. Laser threshold and nonlinear landau fluctuation theory of phase transitions. *Zeitschrift für Physik A Hadrons and nuclei*, 242(5):458–475, 1971.

[38] I. Siddiqi, R. Vijay, F. Pierre, C.M.Wilson, M. Metcalfe, C. Rigetti, L. Frunzio, and M. H. Devoret. RF-driven josephson bifurcation amplifier for quantum measurement. *Phys. Rev. Lett.*, 93:207002, 2004.

[39] R. Vijay, M. H. Devoret, and I. Siddiqi. Invited review article: The josephson bifurcation amplifier. *Review of Scientific Instruments*, 80(11):111101, 2009.

[40] A. Szöke, V. Daneu, J. Goldhar, and N. A. Kurnit. BISTABLE OPTICAL ELEMENT AND ITS APPLICATIONS. *Applied Physics Letters*, 15(11):376–379, dec 1969.

[41] H. M. Gibbs, S. L. McCall, T. N. C. Venkatesan, A. C. Gossard, A. Passner, and W. Wiegmann. Optical bistability in semiconductors. *Applied Physics Letters*, 35(6):451–453, sep 1979.

[42] A. Amo, D. Sanvitto, F. P. Laussy, D. Ballarini, E. del Valle, M. D. Martin, A. Lemaître, J. Bloch, D. N. Krizhanovskii, M. S. Skolnick, C. Tejedor, and L. Viña. Collective fluid dynamics of a polariton condensate in a semiconductor microcavity. *Nature*, 457(7227):291–295, jan 2009.

[43] Howard J Carmichael. Breakdown of photon blockade: A dissipative quantum phase transition in zero dimensions. *Physical Review X*, 5(3):031028, 2015.

[44] R Bonifacio, M Gronchi, and LA Lugiato. Photon statistics of a bistable absorber. *Physical Review A*, 18(5):2266, 1978.

[45] P D Drummond and D F Walls. Quantum theory of optical bistability. I. Nonlinear polarisability model. *Journal of Physics A: Mathematical and General*, 13(2):725–741, feb 1980.

[46] Th K Mavrogordatos, G Tancredi, Matthew Elliott, M J Peterer, A Patterson, J Rahamim, P J Leek, Eran Ginossar, and M H Szymańska. Simultaneous bistability of a qubit and resonator in circuit quantum electrodynamics. *Physical review letters*, 118(4):040402, 2017.

[47] Wim Casteels, Rosario Fazio, and Christiano Ciuti. Critical dynamical properties of a first-order dissipative phase transition. *Physical Review A*, 95(1):012128, 2017.

[48] Fabrizio Minganti, Alberto Biella, Nicola Bartolo, and Cristiano Ciuti. Spectral theory of liouvillians for dissipative phase transitions. *Physical Review A*, 98(4):042118, 2018.

[49] M D Reed, L DiCarlo, B R Johnson, L Sun, D I Schuster, L Frunzio, and R J Schoelkopf. High-fidelity readout in circuit quantum electrodynamics using the jaynes-cummings nonlinearity. *Physical review letters*, 105(17):173601, 2010.

[50] Lev S Bishop, Eran Ginossar, and S M Girvin. Response of the strongly driven jaynes-cummings oscillator. *Physical review letters*, 105(10):100505, 2010.

[51] E Ginossar, Lev S Bishop, D I Schuster, and S M Girvin. Protocol for high-fidelity readout in the photon-blockade regime of circuit qed. *Physical Review A*, 82(2):022335, 2010.

[52] K W Murch, E Ginossar, S J Weber, R Vijay, S M Girvin, and I Siddiqi. Quantum state sensitivity of an autoresonant superconducting circuit. *Physical Review B*, 86(22):220503, 2012.

[53] Francois Mallet, Florian R Ong, Agustin Palacios-Laloy, Francois Nguyen, Patrice Bertet, Denis Vion, and Daniel Esteve. Single-shot qubit readout in circuit quantum electrodynamics. *Nature Physics*, 5(11):791, 2009.

[54] A. Lupascu, E. F. C. Driessen, L. Roschier, C. J. P. M. Harmans, and J. E. Mooij. High-contrast dispersive readout of a superconducting flux qubit using a nonlinear resonator. *Phys. Rev. Lett.*, 96:127003, 2006.

[55] I Siddiqi, R Vijay, M Metcalfe, E Boaknin, L Frunzio, RJ Schoelkopf, and MH Devoret. Dispersive measurements of superconducting qubit coherence with a fast latching readout. *Physical Review B*, 73(5):054510, 2006.

[56] Maxime Boissonneault, J. M. Gambetta, and Alexandre Blais. Improved Superconducting Qubit Readout by Qubit-Induced Nonlinearities. *Physical Review Letters*, 105(10):100504, sep 2010.

[57] Natalya S. Maslova, Evgeny V. Anikin, Nikolay A. Gippius, and Igor M. Sokolov. Effects of tunneling and multiphoton transitions on squeezed-state generation in bistable driven systems. *Phys. Rev. A*, 99:043802, Apr 2019.

[58] Th K Mavrogordatos, F Barratt, U Asari, P Szafulski, Eran Ginossar, and M H Szymańska. Rare quantum metastable states in the strongly dispersive jaynes-cummings oscillator. *Physical Review A*, 97(3):033828, 2018.

[59] M. I. Dykman. Critical exponents in metastable decay via quantum activation. *Phys. Rev. E*, 75:011101, Jan 2007.

[60] Mattias Fitzpatrick, Neereja M. Sundaresan, Andy C. Y. Li, Jens Koch, and Andrew A. Houck. Observation of a Dissipative Phase Transition in a One-Dimensional Circuit QED Lattice. *Physical Review X*, 7(1):011016, feb 2017.

[61] Andreas Angerer, Stefan Putz, Dmitry O Krimer, Thomas Astner, Matthias Zens, Ralph Glattauer, Kirill Streltsov, William J Munro, Kae Nemoto,

Stefan Rotter, Jörg Schmiedmayer, and Johannes Majer. Ultralong relaxation times in bistable hybrid quantum systems. *Science advances*, 3(12):e1701626, 2017.

[62] Filippo Vicentini, Fabrizio Minganti, Riccardo Rota, Giuliano Orso, and Cristiano Ciuti. Critical slowing down in driven-dissipative Bose-Hubbard lattices. *Physical Review A*, 97(1):013853, jan 2018.

[63] Maxim Goryachev, Warrick G Farr, Daniel L Creedon, Yaohui Fan, Mikhail Kostylev, and Michael E Tobar. High-cooperativity cavity qed with magnons at microwave frequencies. *Physical Review Applied*, 2(5):054002, 2014.

[64] Heinz-Peter Breuer and F. (Francesco) Petruccione. *The theory of open quantum systems*. Oxford University Press, 2002.

[65] Maxime Boissonneault, Jay M Gambetta, and Alexandre Blais. Dispersive regime of circuit qed: Photon-dependent qubit dephasing and relaxation rates. *Physical Review A*, 79(1):013819, 2009.

[66] A Vukics, A Dombi, Johannes M Fink, and P Domokos. Finite-size scaling of the photon-blockade breakdown dissipative quantum phase transition. *Quantum*, 3:150, 2019.

[67] Cristóbal Lledó, Th K Mavrogordatos, and MH Szymańska. Driven bose-hubbard dimer under nonlocal dissipation: A bistable time crystal. *Physical Review B*, 100(5):054303, 2019.

[68] Mattias Fitzpatrick, Neereja M Sundaresan, Andy CY Li, Jens Koch, and Andrew A Houck. Observation of a dissipative phase transition in a one-dimensional circuit qed lattice. *Physical Review X*, 7(1):011016, 2017.

[69] Jay Gambetta, Alexandre Blais, David I Schuster, Andreas Wallraff, L Frunzio, J Majer, Michel H Devoret, Steven M Girvin, and Robert J Schoelkopf. Qubit-photon interactions in a cavity: Measurement-induced dephasing and number splitting. *Physical Review A*, 74(4):042318, 2006.

[70] Jay Gambetta, Alexandre Blais, Maxime Boissonneault, Andrew A Houck, DI Schuster, and Steven M Girvin. Quantum trajectory approach to circuit qed: Quantum jumps and the zeno effect. *Physical Review A*, 77(1):012112, 2008.

[71] Maxime Boissonneault, JM Gambetta, and Alexandre Blais. Nonlinear dispersive regime of cavity qed: The dressed dephasing model. *Physical Review A*, 77(6):060305, 2008.

[72] Maxime Boissonneault, AC Doherty, FR Ong, P Bertet, D Vion, D Esteve, and A Blais. Back-action of a driven nonlinear resonator on a superconducting qubit. *Physical Review A*, 85(2):022305, 2012.

[73] Raphaël Lescanne, Lucas Verney, Quentin Ficheux, Michel H Devoret, Benjamin Huard, Mazyar Mirrahimi, and Zaki Leghtas. Escape of a driven quantum josephson circuit into unconfined states. *Physical Review Applied*, 11(1):014030, 2019.

[74] J Robert Johansson, Paul D Nation, and Franco Nori. Qutip: An open-source python framework for the dynamics of open quantum systems. *Computer Physics Communications*, 183(8):1760–1772, 2012.

[75] Alex Kamenev. *Field theory of non-equilibrium systems*. Cambridge University Press, 2011.

[76] Emanuele G Dalla Torre, Sebastian Diehl, Mikhail D Lukin, Subir Sachdev, and Philipp Strack. Keldysh approach for nonequilibrium phase transitions in quantum optics: Beyond the dicke model in optical cavities. *Physical Review A*, 87(2):023831, 2013.

[77] Lukas M Sieberer, Michael Buchhold, and Sebastian Diehl. Keldysh field theory for driven open quantum systems. *Reports on Progress in Physics*, 79(9):096001, 2016.

[78] V. N. Smelyanskiy, M. I. Dykman, and R. S. Maier. Topological features of large fluctuations to the interior of a limit cycle. *Phys. Rev. E*, 55:2369–2391, Mar 1997.

[79] Sidney Coleman. *Aspects of Symmetry: Selected Erice Lectures*. Cambridge University Press, 1985.

[80] Pauli Virtanen, Ralf Gommers, Travis E. Oliphant, Matt Haberland, Tyler Reddy, David Cournapeau, Evgeni Burovski, Pearu Peterson, Warren Weckesser, Jonathan Bright, Stéfan J. van der Walt, Matthew Brett, Joshua Wilson, K. Jarrod Millman, Nikolay Mayorov, Andrew R. J. Nelson, Eric Jones, Robert Kern, Eric Larson, C J Carey, İlhan Polat, Yu Feng, Eric W. Moore, Jake VanderPlas, Denis Laxalde, Josef Perktold, Robert Cimrman, Ian Henriksen, E. A. Quintero, Charles R. Harris, Anne M. Archibald, Antônio H. Ribeiro, Fabian Pedregosa, Paul van Mulbregt, and SciPy 1.0 Contributors. SciPy 1.0: Fundamental Algorithms for Scientific Computing in Python. *Nature Methods*, 17:261–272, 2020.

[81] H. Kleinert. *Path Integrals in Quantum Mechanics, Statistics, Polymer Physics, and Financial Markets*. EBL-Schweitzer. World Scientific, 2009.

[82] Andrew N. Jordan and Eugene V. Sukhorukov. Transport statistics of bistable systems. *Phys. Rev. Lett.*, 93:260604, Dec 2004.

[83] David Marin Roma, Ruadhan A. O'Flanagan, Andrei E. Ruckenstein, Anirvan M. Sengupta, and Ranjan Mukhopadhyay. Optimal path to epigenetic switching. *Phys. Rev. E*, 71:011902, Jan 2005.

[84] Howard M Wiseman and Gerard J Milburn. *Quantum measurement and control*. Cambridge university press, 2009.

[85] F. Pedregosa, G. Varoquaux, A. Gramfort, V. Michel, B. Thirion, O. Grisel, M. Blondel, P. Prettenhofer, R. Weiss, V. Dubourg, J. Vanderplas, A. Passos,

D. Cournapeau, M. Brucher, M. Perrot, and E. Duchesnay. Scikit-learn: Machine learning in Python. *Journal of Machine Learning Research*, 12:2825–2830, 2011.

[86] Gregory Breit and Eugene Wigner. Capture of slow neutrons. *Physical review*, 49(7):519, 1936.

[87] Ugo Fano. Effects of configuration interaction on intensities and phase shifts. *Physical Review*, 124(6):1866, 1961.

[88] AZ Devdariani, VN Ostrovskii, and Yu N Sebyakin. Crossing of quasistationary levels. *Sov. Phys. JETP*, 44:477, 1976.

[89] Frank-Michael Dittes. The decay of quantum systems with a small number of open channels. *Physics Reports*, 339(4):215–316, 2000.

[90] H Friedrich and D Wintgen. Interfering resonances and bound states in the continuum. *Physical Review A*, 32(6):3231, 1985.

[91] J-L Orgiazzi, C Deng, D Layden, R Marchildon, F Kitapli, F Shen, M Bal, FR Ong, and A Lupascu. Flux qubits in a planar circuit quantum electrodynamics architecture: quantum control and decoherence. *arXiv:1407.1346*, 2014.

[92] Vladimir B. Braginsky, Mikhail L. Gorodetsky, Farid Ya. Khalili, and Kip S. Thorne. Dual-resonator speed meter for a free test mass. *arXiv:gr-qc/9906108*, 1999.

[93] Qianfan Xu, Sunil Sandhu, Michelle L Povinelli, Jagat Shakya, Shanhui Fan, and Michal Lipson. Experimental realization of an on-chip all-optical analogue to electromagnetically induced transparency. *Physical review letters*, 96(12):123901, 2006.

[94] Yong-Chun Liu, Bei-Bei Li, and Yun-Feng Xiao. Electromagnetically induced transparency in optical microcavities. *Nanophotonics*, 6(5):789–811, 2017.

[95] Edward Mills Purcell. Spontaneous emission probabilities at radio frequencies. In *Confined Electrons and Photons*, pages 839–839. Springer, 1995.

[96] GE Makhmetov, AG Borisov, D Teillet-Billy, and JP Gauyacq. Interaction between overlapping quasi-stationary states: He (2 1s and 2 1p) levels in front of an aluminium surface. *EPL (Europhysics Letters)*, 27(3):247, 1994.

[97] I Seipp, KT Taylor, and W Schweizer. Atomic resonances in parallel electric and magnetic fields. *Journal of Physics B: Atomic, Molecular and Optical Physics*, 29(1):1, 1996.

[98] Jonathan P Marangos. Electromagnetically induced transparency. *Journal of Modern Optics*, 45(3):471–503, 1998.

[99] Ying Wu and Xiaoxue Yang. Electromagnetically induced transparency in v-, λ-, and cascade-type schemes beyond steady-state analysis. *Physical Review A*, 71(5):053806, 2005.

[100] D Budker, DF Kimball, SM Rochester, and VV Yashchuk. Nonlinear magneto-optics and reduced group velocity of light in atomic vapor with slow ground state relaxation. *Physical review letters*, 83(9):1767, 1999.

[101] Michael Fleischhauer and Mikhail D Lukin. Quantum memory for photons: Dark-state polaritons. *Physical Review A*, 65(2):022314, 2002.

[102] Eyal Buks, Paul Brookes, Eran Ginossar, Chunqing Deng, Jean-Luc FX Orgiazzi, Martin Otto, and Adrian Lupascu. Driving-induced resonance narrowing in a strongly coupled cavity-qubit system. *arXiv preprint arXiv:2008.00224*, 2020.

[103] J. E. Mooij, T. P. Orlando, L. Levitov, Lin Tian, Caspar H. Van der Wal, and Seth Lloyd. Josephson persistent-current qubit. *Science*, 285:1036 – 1039, 1999.

[104] T. P. Orlando, J. E. Mooij, Lin Tian, Caspar H. van der Wal, L. S. Levitov, Seth Lloyd, and J. J. Mazo. Superconducting persistent-current qubit. *Phys. Rev. B*, 60(22):15398–15413, Dec 1999.

[105] A. Wallraff, D. I. Schuster, A. Blais, L. Frunzio, R.-S. Huang, J. Majer, S. Kumar, S. M. Girvin, and R. J. Schoelkopf. Strong coupling of a single photon to a superconducting qubit using circuit quantum electrodynamics. *Nature*, 431:162–167, 2004.

[106] Thomas Niemczyk, F Deppe, H Huebl, EP Menzel, F Hocke, MJ Schwarz, JJ Garcia-Ripoll, D Zueco, T Hümmer, E Solano, et al. Circuit quantum electrodynamics in the ultrastrong-coupling regime. *Nature Physics*, 6(10):772–776, 2010.

[107] Pol Forn-Díaz, J Lisenfeld, David Marcos, Juan José García-Ripoll, Enrique Solano, CJPM Harmans, and JE Mooij. Observation of the Bloch-Siegert shift in a qubit-oscillator system in the ultrastrong coupling regime. *Physical Review Letters*, 105(23):237001, 2010.

[108] P Forn-Díaz, L Lamata, E Rico, J Kono, and E Solano. Ultrastrong coupling regimes of light-matter interaction. *arXiv:1804.09275*, 2018.

[109] Abdufarrukh A Abdumalikov Jr, Oleg Astafiev, Yasunobu Nakamura, Yuri A Pashkin, and JawShen Tsai. Vacuum rabi splitting due to strong coupling of a flux qubit and a coplanar-waveguide resonator. *Physical review b*, 78(18):180502, 2008.

[110] Mustafa Bal, Chunqing Deng, Jean-Luc Orgiazzi, FR Ong, and Adrian Lupascu. Ultrasensitive magnetic field detection using a single artificial atom. *Nature communications*, 3:1324, 2012.

[111] J-L Orgiazzi, C Deng, D Layden, R Marchildon, F Kitapli, F Shen, M Bal, FR Ong, and A Lupascu. Flux qubits in a planar circuit quantum electrodynamics architecture: quantum control and decoherence. *Physical Review B*, 93(10):104518, 2016.

[112] *Quantum Phase Transitions Second Edition-Quantum Phase Transitions: Second Edition Subir Sachdev Frontmatter More information*.

[113] G. Oelsner, S. H. W. van der Ploeg, P. Macha, U. Hübner, D. Born, S. Anders, E. Il'ichev, H.-G. Meyer, M. Grajcar, S. Wünsch, M. Siegel, A. N. Omelyanchouk, and O. Astafiev. Weak continuous monitoring of a flux qubit using coplanar waveguide resonator. *Phys. Rev. B*, 81:172505, May 2010.

[114] Kunihiro Inomata, Tsuyoshi Yamamoto, P-M Billangeon, Y Nakamura, and JS Tsai. Large dispersive shift of cavity resonance induced by a superconducting flux qubit in the straddling regime. *Physical Review B*, 86(14):140508, 2012.

[115] Markus Jerger, Stefano Poletto, Pascal Macha, Uwe Hübner, Evgeni Il'ichev, and Alexey V Ustinov. Frequency division multiplexing readout and simultaneous manipulation of an array of flux qubits. *Applied Physics Letters*, 101(4):042604, 2012.

[116] I Serban, MI Dykman, and FK Wilhelm. Relaxation of a qubit measured by a driven duffing oscillator. *Physical Review A*, 81(2):022305, 2010.

[117] Catherine Laflamme and Aashish A Clerk. Quantum-limited amplification with a nonlinear cavity detector. *Physical Review A*, 83(3):033803, 2011.

[118] I Siddiqi, R Vijay, F Pierre, CM Wilson, M Metcalfe, C Rigetti, L Frunzio, and MH Devoret. Rf-driven josephson bifurcation amplifier for quantum measurement. *Physical review letters*, 93(20):207002, 2004.

[119] A Lupaşcu, EFC Driessen, L Roschier, CJPM Harmans, and JE Mooij. High-contrast dispersive readout of a superconducting flux qubit using a nonlinear resonator. *Physical review letters*, 96(12):127003, 2006.

[120] E Boaknin, VE Manucharyan, S Fissette, M Metcalfe, L Frunzio, R Vijay, I Siddiqi, A Wallraff, RJ Schoelkopf, and M Devoret. Dispersive microwave

bifurcation of a superconducting resonator cavity incorporating a josephson junction. *arXiv:0702445*, 2007.

[121] François Mallet, Florian R Ong, Agustin Palacios-Laloy, Francois Nguyen, Patrice Bertet, Denis Vion, and Daniel Esteve. Single-shot qubit readout in circuit quantum electrodynamics. *Nature Physics*, 5(11):791–795, 2009.

[122] Maxime Boissonneault, JM Gambetta, and Alexandre Blais. Improved superconducting qubit readout by qubit-induced nonlinearities. *Physical review letters*, 105(10):100504, 2010.

[123] Maxime Boissonneault, AC Doherty, FR Ong, P Bertet, D Vion, D Esteve, and A Blais. Superconducting qubit as a probe of squeezing in a nonlinear resonator. *Physical Review A*, 89(2):022324, 2014.

[124] Maxime Boissonneault, AC Doherty, FR Ong, P Bertet, D Vion, D Esteve, and A Blais. Back-action of a driven nonlinear resonator on a superconducting qubit. *Physical Review A*, 85(2):022305, 2012.

[125] Maxime Boissonneault, Jay M Gambetta, and Alexandre Blais. Dispersive regime of circuit qed: Photon-dependent qubit dephasing and relaxation rates. *Physical Review A*, 79(1):013819, 2009.

[126] MD Reed, L DiCarlo, BR Johnson, L Sun, DI Schuster, L Frunzio, and RJ Schoelkopf. High-fidelity readout in circuit quantum electrodynamics using the jaynes-cummings nonlinearity. *Physical review letters*, 105(17):173601, 2010.

[127] FR Ong, M Boissonneault, F Mallet, AC Doherty, A Blais, D Vion, D Esteve, and P Bertet. Quantum heating of a nonlinear resonator probed by a superconducting qubit. *Physical Review Letters*, 110(4):047001, 2013.

[128] Florian R Ong, M Boissonneault, F Mallet, A Palacios-Laloy, A Dewes, AC Doherty, A Blais, P Bertet, D Vion, and D Esteve. Circuit qed with a

nonlinear resonator: ac-stark shift and dephasing. *Physical review letters*, 106(16):167002, 2011.

[129] Lev S Bishop, JM Chow, Jens Koch, AA Houck, MH Devoret, E Thuneberg, SM Girvin, and RJ Schoelkopf. Nonlinear response of the vacuum rabi resonance. *Nature Physics*, 5(2):105–109, 2009.

[130] V Peano and M Thorwart. Quasienergy description of the driven jaynes-cummings model. *Physical Review B*, 82(15):155129, 2010.

[131] Johannes Hausinger and Milena Grifoni. Qubit-oscillator system under ultrastrong coupling and extreme driving. *Physical Review A*, 83(3):030301, 2011.

[132] Lev S Bishop, Eran Ginossar, and SM Girvin. Response of the strongly driven jaynes-cummings oscillator. *Physical review letters*, 105(10):100505, 2010.

[133] Eyal Buks, Chunqing Deng, Jean-Luc F. X. Orgazzi, Martin Otto, and Adrian Lupascu. Superharmonic resonances in a strongly coupled cavity-atom system. *Phys. Rev. A*, 94:033807, Sep 2016.

[134] P Carbonaro, G Compagno, and F Persico. Canonical dressing of atoms by intense radiation fields. *Physics Letters A*, 73(2):97–99, 1979.

[135] Maxime Boissonneault, JM Gambetta, and Alexandre Blais. Improved superconducting qubit readout by qubit-induced nonlinearities. *Physical review letters*, 105(10):100504, 2010.

[136] Alice Berthelot, Ivan Favero, Guillaume Cassabois, Christophe Voisin, Claude Delalande, Ph Roussignol, Robson Ferreira, and Jean-Michel Gérard. Unconventional motional narrowing in the optical spectrum of a semiconductor quantum dot. *Nature Physics*, 2(11):759–764, 2006.

[137] Nicolaas Bloembergen, Edward Mills Purcell, and Robert V Pound. Relaxation effects in nuclear magnetic resonance absorption. *Physical review*, 73(7):679, 1948.

[138] Jian Li, MP Silveri, KS Kumar, J-M Pirkkalainen, A Vepsäläinen, WC Chien, J Tuorila, MA Sillanpää, PJ Hakonen, EV Thuneberg, et al. Motional averaging in a superconducting qubit. *Nature communications*, 4(1):1–6, 2013.

[139] P W. Anderson. A mathematical model for the narrowing of spectral lines by exchange or motion. *Journal of the Physical Society of Japan*, 9(3):316–339, 1954.

[140] Th K Mavrogordatos, G Tancredi, Matthew Elliott, MJ Peterer, A Patterson, J Rahamim, PJ Leek, Eran Ginossar, and MH Szymańska. Simultaneous bistability of a qubit and resonator in circuit quantum electrodynamics. *Physical review letters*, 118(4):040402, 2017.

[141] Th K Mavrogordatos, F Barratt, U Asari, P Szafulski, Eran Ginossar, and MH Szymańska. Rare quantum metastable states in the strongly dispersive jaynes-cummings oscillator. *Physical Review A*, 97(3):033828, 2018.

[142] Jay Gambetta, Alexandre Blais, Maxime Boissonneault, AA Houck, DI Schuster, and SM Girvin. Quantum trajectory approach to circuit qed: Quantum jumps and the zeno effect. *Physical Review A*, 77(1):012112, 2008.

[143] PD Drummond and DF Walls. Quantum theory of optical bistability. i. nonlinear polarisability model. *Journal of Physics A: Mathematical and General*, 13(2):725, 1980.

[144] Lev S Bishop. Circuit quantum electrodynamics. *arXiv preprint arXiv:1007.3520*, 2010.

[145] Andreas Stathopoulos and James R. McCombs. PRIMME: PReconditioned Iterative MultiMethod Eigensolver: Methods and software description. *ACM Transactions on Mathematical Software*, 37(2):21:1–21:30, 2010.

[146] John M Martinis, S Nam, J Aumentado, KM Lang, and C Urbina. Decoherence of a superconducting qubit due to bias noise. *Physical Review B*, 67(9):094510, 2003.

[147] G Zimmerli, Travis M Eiles, Richard L Kautz, and John M Martinis. Noise in the coulomb blockade electrometer. *Applied Physics Letters*, 61(2):237–239, 1992.

[148] LS Kuzmin, P Delsing, T Claeson, and KK Likharev. Single-electron charging effects in one-dimensional arrays of ultrasmall tunnel junctions. *Physical review letters*, 62(21):2539, 1989.

[149] LJ Geerligs, VF Anderegg, and JE Mooij. Tunneling time and offset charging in small tunnel junctions. *PhyB*, 165:973–974, 1990.

[150] Audrey Cottet. *Implementation of a quantum bit in a superconducting circuit*. PhD thesis, PhD Thesis, Université Paris 6, 2002.

[151] Roger H Koch, David P DiVincenzo, and John Clarke. Model for 1/f flux noise in squids and qubits. *Physical review letters*, 98(26):267003, 2007.

[152] Jochen Braumüller, Leon Ding, Antti P Vepsäläinen, Youngkyu Sung, Morten Kjaergaard, Tim Menke, Roni Winik, David Kim, Bethany M Niedzielski, Alexander Melville, et al. Characterizing and optimizing qubit coherence based on squid geometry. *Physical Review Applied*, 13(5):054079, 2020.

[153] Grégoire Ithier. *Manipulation, readout and analysis of the decoherence of a superconducting quantum bit*. PhD thesis, 2005.

[154] G Ithier, E Collin, P Joyez, PJ Meeson, Denis Vion, Daniel Esteve, F Chiarello, A Shnirman, Yu Makhlin, Josef Schriefl, et al. Decoherence in a superconducting quantum bit circuit. *Physical Review B*, 72(13):134519, 2005.

[155] Michael Stern, Gianluigi Catelani, Yuimaru Kubo, Cecile Grezes, Audrey Bienfait, Denis Vion, Daniel Esteve, and Patrice Bertet. Flux qubits with long coherence times for hybrid quantum circuits. *Physical review letters*, 113(12):123601, 2014.

[156] Aaron D O'Connell, M Ansmann, Radoslaw C Bialczak, Max Hofheinz, Nadav Katz, Erik Lucero, C McKenney, Matthew Neeley, Haohua Wang, Eva M Weig, et al. Microwave dielectric loss at single photon energies and millikelvin temperatures. *Applied Physics Letters*, 92(11):112903, 2008.

[157] Roman Lutchyn, Leonid Glazman, and Anatoly Larkin. Quasiparticle decay rate of josephson charge qubit oscillations. *Physical Review B*, 72(1):014517, 2005.

[158] Gianluigi Catelani, Jens Koch, Luigi Frunzio, RJ Schoelkopf, Michel H Devoret, and LI Glazman. Quasiparticle relaxation of superconducting qubits in the presence of flux. *Physical review letters*, 106(7):077002, 2011.

[159] Gianluigi Catelani, Robert J Schoelkopf, Michel H Devoret, and Leonid I Glazman. Relaxation and frequency shifts induced by quasiparticles in superconducting qubits. *Physical Review B*, 84(6):064517, 2011.

[160] J Aumentado, Mark W Keller, John M Martinis, and Michel H Devoret. Nonequilibrium quasiparticles and 2 e periodicity in single-cooper-pair transistors. *Physical review letters*, 92(6):066802, 2004.

[161] Audrey Bienfait, JJ Pla, Yuimaru Kubo, Xin Zhou, Michael Stern, CC Lo, CD Weis, Thomas Schenkel, Denis Vion, Daniel Esteve, et al. Controlling spin relaxation with a cavity. *Nature*, 531(7592):74–77, 2016.

[162] A. Wallraff, D. I. Schuster, A. Blais, L. Frunzio, R.-S. Huang, J. Majer, S. Kumar, S. M. Girvin, and R. J. Schoelkopf. Strong coupling of a single photon to a superconducting qubit using circuit quantum electrodynamics. *Nature*, 431:162–167, Sep 2004.

[163] CD Wilen, S Abdullah, NA Kurinsky, C Stanford, L Cardani, G d'Imperio, C Tomei, L Faoro, LB Ioffe, CH Liu, et al. Correlated charge noise and relaxation errors in superconducting qubits. *arXiv preprint arXiv:2012.06029*, 2020.